Fabrication and Characterization of Nonlinear Optical Ceramics for Random Quasi-Phase-Matching

2019

Xuan Chen
University of Central Florida

FABRICATION AND CHARACTERIZATION OF NONLINEAR OPTICAL CERAMICS FOR RANDOM QUASI-PHASE-MATCHING

by

XUAN CHEN

B.Sc., Northeastern University, China, 2013
M.S., University of Central Florida, USA, 2015

A dissertation submitted in partial fulfillment of the requirements
for the degree of Doctor of Philosophy
in the Department of Materials Science and Engineering
in the College of Engineering and Computer Science
at the University of Central Florida
Orlando, Florida

Fall Term
2018

Major Professor: Romain Gaume

ABSTRACT

A number of technologies rely on the conversion of short laser pulses from one spectral domain to another. Efficient frequency conversion is currently obtained in ordered nonlinear optical materials and requires a periodic spatial modulation of their nonlinear coefficient which results in a narrow bandwidth. One can trade off efficiency for more spectral bandwidth by relaxing the strict phase-matching conditions and achieve nonlinear interaction in carefully engineered disordered crystalline aggregates, in a so-called random quasi-phase-matching (rQPM) process. In this dissertation, we examine appropriate fabrication pathways for (1-x)Pb($Mg_{1/3}Nb_{2/3}$)O_3-x$PbTiO_3$ (PMN-PT) and ZnSe transparent ceramics for applications in the mid-IR. The main challenge associated with the fabrication of high transparency PMN-PT ceramics is to avoid the parasitic pyrochlore phase. The most effective method to suppress the formation of this undesired phase is to use magnesium niobate ($MgNb_2O_6$) as the starting material. We have found that, contrary to commercially available lead oxide powders, nanopowders synthesized in our lab by the combustion method help improve the densification of ceramics and their overall optical quality. The effects of dopants on the microstructure evolution and phase-purity control in PMN-PT ceramics are also investigated and show that La^{3+} helps control grain-growth and get a pure perovskite phase, thereby improving the samples transparency. With large second order susceptibility coefficients and wide transmission window from 0.45 to 21 µm, polycrystalline zinc selenide is also an ideal candidate material for accessing the MWIR spectrum through rQPM nonlinear interaction. We have investigated non-stoichiometric heat-treatment conditions necessary to develop adequate microstructure for rQPM from commercial CVD-grown ZnSe ceramics. We have been able to demonstrate the world's first optical parametric oscillation (OPO)

based on rQPM in ZnSe transparent ceramic, enabling broadband frequency combs spanning 3-7.5 μm.

Key Words: $\chi^{(2)}$ interaction, Transparent Ceramic, PMN-PT, ZnSe, Sintering Additive, Non-stoichiometry, Grain-growth.

To my husband Zhangchi and my parents

ACKNOWLEDGMENTS

First of all, I would like to take this opportunity to express my sincere gratitude to my advisor Prof. Romain Gaume, for his patience, motivation and guidance. The countless hours he spent with me discussing various problems and sharing his immense knowledge have had a great influence on my research life. Besides my advisor, I would like to thank the rest of my thesis committee: Prof. Kathleen Richardson, Prof. Yongho Sohn, Prof. Suryanarayana Challapalli and Prof. Stephen Kuebler, for their insightful comments which help me widen my research from various perspectives. I would also like to thank Prof. Konstantin Vodopyanov for showing me the nonlinear properties measurement techniques. I am very grateful to Qitian Ru, Taiki Kawamori and Zachary Loparo from his group for helping me with some of the experiments and the simulation part discussion. I would like to thank my friends and colleagues Dr. Shi Chen, Dr. William Taylor Shoulders, Dr. Sudeep Pandey and Matthew Julian for their companionship. Over the years, the group welcomed postdocs and students, who each contributed to my progress in their own way. Last but not the least, I would like to thank my husband Zhangchi for his support and undiminishing faith in me.

TABLE OF CONTENTS

LIST OF FIGURES

LIST OF TABLES

LIST OF ABBREVIATIONS

CIP	Cold-Isostatic Pressing
CN	Coordination Number
CVD	Chemical Vapor Deposition
DFG	Difference-Frequency Generation
EDS	Energy-Dispersive X-ray Spectroscopy
EDTA	Ethylenediaminetetraacetic Acid
EO	Electro-Optic
FE	Ferroelectric
FLIR	Forward Looking Infrared
GNP	Glycine Nitrate Process
GVD	Group Velocity Dispersion
HIP	High Isostatic Press
HP	Hot Press
KDP	Potassium Dihydrogen Phosphate
L_{coh}	Coherence Length
MCT	Mercury Cadmium Telluride
MPB	Morphotropic Phase Boundary
NLO	Nonlinear Optics
OPO	Optical Parametric Oscillation
OP-GaAs	Orientation-Patterned Gallium Arsenide

OP-GaP	Orientation-Patterned Gallium Phosphide
PE	Paraelectric
PIN-PMN-PT	Lead Indium Niobate - Lead Magnesium Niobate - Lead Titanate
PIN-PT	Lead Indium Niobate - Lead Titanate
PLZT	Lead Lanthanum Zirconate Titanate
PMN-PT	Lead Magnesium Niobate - Lead Titanate
PPLN	Periodically-Poled Lithium Niobate
PSN-PT	Lead Scandium Niobate - Lead Titanate
PYN-PT	Lead Yttrium Niobate - Lead Titanate
PZN-PT	Lead Zinc Niobate - Lead Titanate
PZT-PNN	Lead Zirconate Titanate - Lead Nickel Niobate
QPM	Quasi-Phase-Matching
rQPM	Random Quasi-Phase-Matching
SEM	Scanning Electron Microscope
SFG	Sum-Frequency Generation
SHG	Second-Harmonic Generation
SI	International System of Units
SPS	Spark Plasma Sintering
TMA	Thermomechanical Analysis
TOCs	Transparent Optical Ceramics
XRD	X-ray diffraction

CHAPTER ONE: INTRODUCTION

1.1 Transparent Ceramics

Transparent optical ceramics (TOCs) are used in various optical applications, including laser gain-media [1, 2], high-strength windows [3, 4], scintillators [5], electro-optical devices [6], transparent envelopes for high pressure sodium street lamps and compact optics with high refractive index [7, 8]. Their fabrication methods enable large size and complex shapes and the control of dopants and microstructure for enhanced functionalities.

However, transparent ceramics of high optical quality are still challenging to fabricate. The elimination of scattering centers (pores and secondary phases) (Figure 1) requires effective sintering techniques and highly pure phases and raw materials. Over the past 60 years, various processes have been developed to improve the optical quality of TOCs. These include the fabrication of fine and unagglomerated powders through wet chemical synthesis [9-11] and sintering techniques, such as high uniaxial pressing (HP), high isostatic pressing (HIP), vacuum sintering [12-14] and spark plasma sintering (SPS) [15-19].

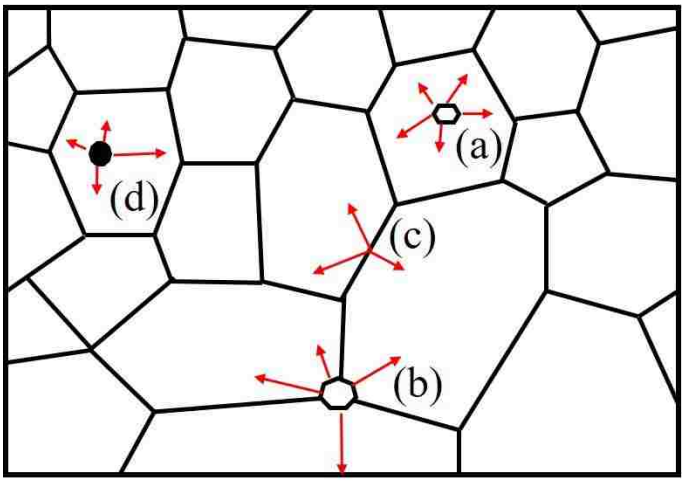

Figure 1. Scattering sources in ceramics including (a) porosities within the grains, (b) porosities at the grain boundaries, (c) grain boundaries and (d) second phases.

In recent years, these developments have enabled better control of TOC's physical attributes such as microstructure and transmission spectrum making them attractive for nonlinear optics (NLO).

1.2 Nonlinear Optics

1.2.1 Introduction to Nonlinear Optics

Nonlinear Optics is a branch of optics that studies the behavior of light in nonlinear materials. Typically, only laser light can change the optical properties of a material system because of very high intensity (atomic electric field, 10^8 V/m). Figure 2 shows an example of frequency conversion from near-infrared to mid-infrared through a nonlinear crystal. In order to explain the physics in Figure 2, Figure 3 shows the energy diagram of linear and nonlinear optics. In linear optics, the emitted light has the same energy as the input light and thus has the same waves.

However, in nonlinear optics, the excited photons can be excited to higher energy level under high intensity light. The emitted light has a higher energy than the input light and new waves are created.

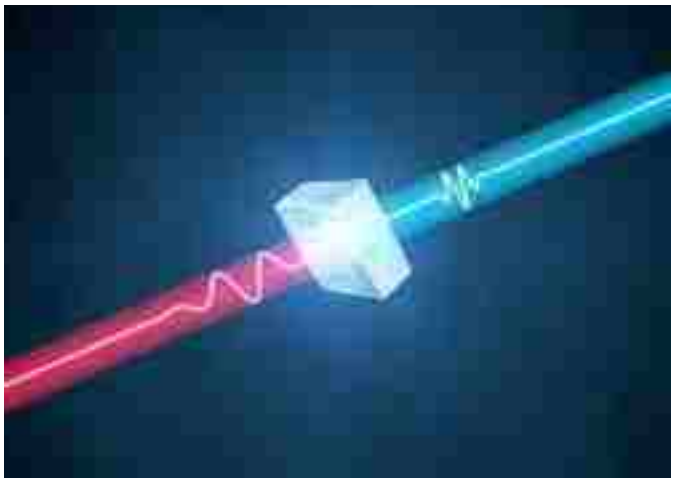

Figure 2. An illustration of frequency conversion from near-infrared to mid-infrared through a nonlinear crystal [20].

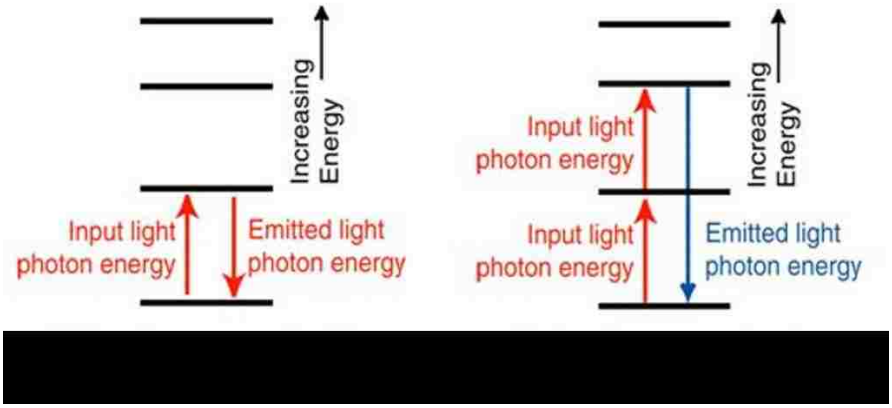

Figure 3. Energy level diagrams of linear and nonlinear optics [21].

In the case of linear optics, the polarization depends linearly on the electric field and can be described by the relationship

$$P(\omega) = \varepsilon_0 \chi^{(1)}(\omega;\omega)E(\omega) \quad (1)$$

where ε_0 is the permittivity of free space and $\chi^{(1)}$ is the linear susceptibility. In nonlinear optics, the polarization can be expressed as a power series in the field strength $E(\omega)$

$$P(\omega) = \varepsilon_0\chi^{(1)}E(\omega) + \varepsilon_0\chi^{(2)}E^2(\omega) + \varepsilon_0\chi^{(3)}E^3(\omega) + \cdots$$

$$= P^{(1)}(\omega) + P^{(2)}(\omega) + P^{(3)}(\omega) + \cdots \quad (2)$$

$\chi^{(2)}$ and $\chi^{(3)}$ are second-order and third-order nonlinear optical susceptibilities, respectively. The beams from these high order terms are named as 2nd and 3rd harmonic beams, with a frequency of twice and triple of the incident beam. In this dissertation, we are only interested in the second-order nonlinearity response, which can be written as follows:

$$P^{(2)}(\omega) = \varepsilon_0 \sum_{j,k} \sum_{\omega} K(\omega_3; \omega_1, \omega_2)\chi^{(2)}_{ijk}(\omega_3; \omega_1, \omega_2)(E_{\omega_1})_j\,(E_{\omega_2})_k \quad (3)$$

where the indices i, j, k denote the Cartesian components of the electric fields. The fundamental input beams and second-order harmonic frequency are ω_1, ω_2, ω_3 ($\omega_3 = \omega_1 + \omega_2$) respectively. The coefficient $K(\omega_3; \omega_1, \omega_2)$ takes into account the fact that frequencies of the input beams can be equal in some processes and depends on the nonlinear optical interactions [22]. Based on Neumann's principle, in order to have non-zero second-order response, crystals should lack inversion symmetry. Crystal classes where the inversion symmetry is missing are called non-centrosymmetric, which will be discussed in more details in section 1.3.

1.2.2 Nonlinear Optical Processes

In order to quantitatively analyze the polarization, we will briefly describe a number of nonlinear optical processes in this section. The rule for calculating $K(\omega_3;\omega_1,\omega_2)$ was defined by Butcher and Cotter [23] and $K(\omega_3;\omega_1,\omega_2)$ values for some second-order processes are given in Table 1. Figure 4 shows the geometry of some nonlinear optical processes. The process of second-harmonic generation (SHG) can double the frequency of the input beam. When there are two beams at different frequencies, we can get a signal at the sum or the difference of these two frequencies through sum-frequency generation (SFG) and difference-frequency generation (DFG). In this section, we only discuss second-harmonic generation and optical parametric oscillation (OPO) in details.

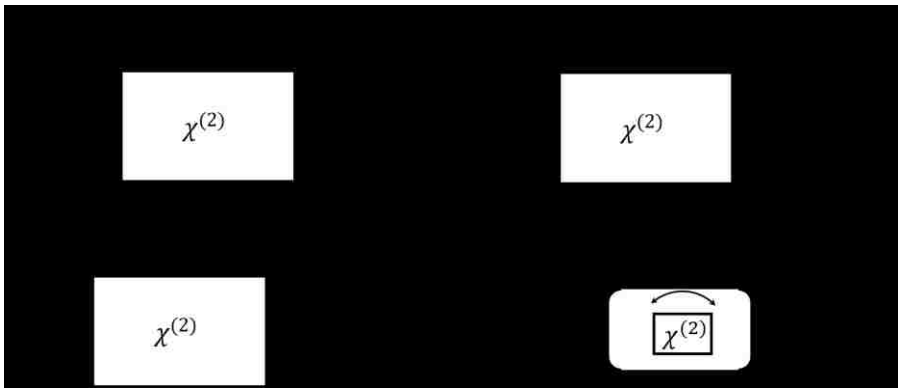

Figure 4. Geometry of (a) second-harmonic generation, (b) sum-frequency generation, (c) difference-frequency generation and (d) optical parametric oscillator.

Table 1 $K(\omega_3;\omega_1,\omega_2)$ values for second-order nonlinear processes.

Process	**Energy conservation**	**Susceptibility**	$\boldsymbol{K(\omega_3;\omega_1,\omega_2)}$
Second-Harmonic Generation (SHG)	$\omega_3 = 2\omega_1$	$\chi^{(2)}_{ijk}(\omega_3;\omega_1,\omega_1)$	1/2
Sum-Frequency Generation (SFG)	$\omega_3 = \omega_1 + \omega_2$	$\chi^{(2)}_{ijk}(\omega_3;\omega_1,\omega_2)$	1
Difference-Frequency Generation (DFG)	$\omega_3 = \omega_1 - \omega_2$	$\chi^{(2)}_{ijk}(\omega_3;\omega_1,-\omega_2)$	1

1.2.2.1 Second-Harmonic Generation

The SHG process is illustrated schematically in Figure 4 (a). The nonlinear polarization is given as

$$P^{(2)}(t) = \varepsilon_0 \chi^{(2)}(\omega_3;\omega_1,\omega_1)E^2 \tag{4}$$

Second-harmonic generation can be considered as an interaction in which photons exchange between the various frequency components of the field. Two photons of frequency ω_1 are destroyed and a photon of frequency $2\,\omega_1$ is created at the same time. Under proper experimental conditions, the conversion can be efficient so that nearly all power at frequency ω_1 can be converted to the second-harmonic frequency $2\omega_1$. In this dissertation, we will use SHG to characterize the second-order properties in samples.

1.2.2.2 Optical Parametric Oscillation

The OPO process is illustrated schematically in Figure 4 (d). When we put the nonlinear crystal into a cavity, this device is known as optical parametric oscillation. The frequency of OPO is tunable because we can generate any frequency ω_2 that is smaller than ω_1. We can control the output frequency of an OPO by changing the phase-matching condition. The frequency ω_1 is called the pump frequency. The desired output frequency is called the signal frequency (ω_2) while the other unwanted frequency is called the idler frequency (ω_3). We are going to use OPO to generate broadband spectrum based on our materials.

1.2.3 Wave Equation for Nonlinear Optical Media

After generating new frequency beams through the nonlinear process, there will be a phase mismatching problem between the interacting waves along the propagation direction. In this section, we will quantitatively analyze the wave equation for the propagation of light through a nonlinear optical medium. Let's start with Maxwell's equations:

$$\nabla \cdot D = \rho$$

$$\nabla \cdot B = 0$$

$$\nabla \times E = -\frac{\partial B}{\partial t}$$

$$\nabla \times H = \frac{\partial D}{\partial t} + J \tag{5}$$

We made the assumptions: (1) the space contains no free charges ($\rho = 0$) and no free currents ($J = 0$); (2) the material is nonmagnetic ($B = \mu_0 H$), where μ_0 is the permeability of free space and H is the magnetizing field. In order to express the nonlinearity in the material, the displacement field D can be described by $D = \varepsilon_0 E + P$, where ε_0 is the permittivity of free space. For convenience, we replace the μ_0 by $1/\varepsilon_0 c^2$. The general form of the wave equation along the propagation direction can be expressed by

$$\nabla \times \nabla \times \mathrm{E} + \frac{1}{c^2}\frac{\partial^2}{\partial t^2}E = -\frac{1}{\varepsilon_0 c^2}\frac{\partial^2 P}{\partial t^2} \tag{6}$$

We take the sum-frequency generation as an example and get the solution to the wave equation for a plane wave at frequency ω_3 along the z direction

$$E_3(z,t) = A_3 e^{i(k_3 z - \omega_3 t)} + complex\ conjugate \tag{7}$$

where $k_3 = \frac{n_3 \omega_3}{c}$, $n_3^2 = \varepsilon^{(1)}(\omega_3)$, $\varepsilon^{(1)}$ stands for the permittivity which is dimensionless and different for each material. A_3 is the amplitude of the wave, which is a constant. However, when A_3 is too large, A_3 will become a function of z and the solution still works. After several approximations, the wave equation becomes

$$\frac{dA_3}{dz} = \frac{2id_{eff}\omega_3^2}{k_3 c^2} A_1 A_2 e^{i\Delta k z} \tag{8}$$

In the case of negative uniaxial crystal of 3*m*, the effective value

$$d_{eff} = d_{31}\sin\theta - d_{22}\cos\theta \sin 3\emptyset \tag{9}$$

where θ is the angle between the propagation vector and the crystalline z axis and $\emptyset$ is the azimuthal angle between the propagation vector and the xz crystalline plane.

We have introduced the quantity

$$\Delta k = k_1 + k_2 - k_3 \tag{10}$$

This is the wavevector mismatch. k_1, k_2, k_3 are the wavenumbers of the beam at frequency ω_1, ω_2 and ω_3. After integrating from z=0 to z=L, we can get the amplitude of the sum-frequency (ω_3) field at the exit plane:

$$A_3(L) = \frac{2id_{eff}\omega_3^2 A_1 A_2}{k_3 c^2}\int_0^L e^{i\Delta kz} = \frac{2id_{eff}\omega_3^2 A_1 A_2}{k_3 c^2}\left(\frac{e^{i\Delta kL}-1}{i\Delta k}\right) \tag{11}$$

The intensity of the ω_3 can be described by

$$I_3 = \frac{8n_3\varepsilon_0 d_{eff}^2\omega_3^4|A_1|^2|A_2|^2}{k_3^2 c^3}\left|\frac{e^{i\Delta kL}-1}{\Delta k}\right|^2 = \frac{8d_{eff}^2\omega_3^2 I_1 I_2}{n_1 n_2 n_3 \varepsilon_0 c^2}L^2 sinc^2\left(\frac{\Delta kL}{2}\right) \tag{12}$$

From equation 12, we can see that intensity is proportional to the factor $sinc^2(\Delta kL/2)$, which is plotted in Figure 5. In order to get perfect phase-matching which means the highest intensity, we have to keep $\Delta k = 0$. The coherence length, which means the propagation distance over which the intensity maintains a specific value, is defined as $L_{coh} = \pi/\Delta k$ when $\Delta kL/2 = \pi/2$ in Figure 5.

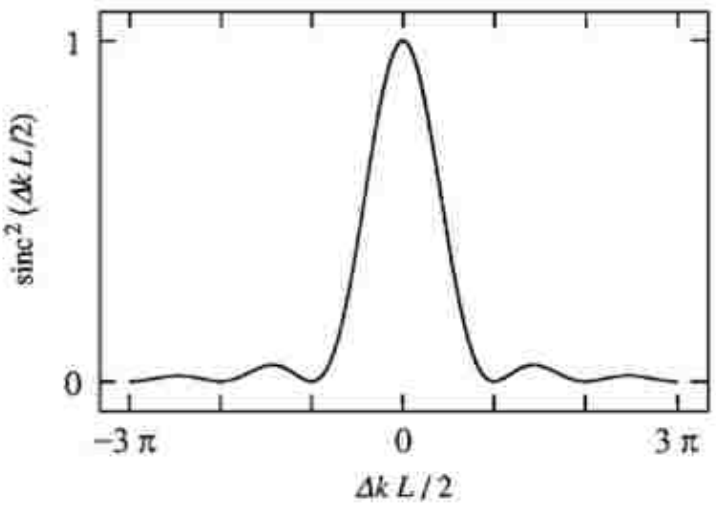

Figure 5. Phase mismatch factor function [24].

1.2.4 Phase-Matching

Phase mismatching will lead to a small conversion efficiency. As discussed in last section, in order to keep phase-matching, we have to keep $\Delta k = 0$. We take the SHG as an example and get the equation

$$2\frac{n(\omega_1)\omega_1}{c} = \frac{n(\omega_2)\omega_2}{c} \tag{13}$$

where ω_1 is the fundamental beam and ω_2 is the second-harmonic beam. This means we have to keep the refractive index at ω_1 equals to the refractive index at $2\omega_1$. This is impossible because the refractive index of materials increases as the frequency in normal dispersion. There are several ways to achieve phase-matching. We are going to talk some general methods like birefringence phase-matching, quasi-phase-matching and random quasi-phase-matching.

1.2.4.1 Phase-Matching using Birefringent Crystals

As noted in the prior section, phase-matching is very important in improving the nonlinear conversion efficiency. This can be achieved in birefringent crystals using the two (ordinary, n_o and extraordinary, n_e) refractive indices of the material (Figure 6). In the case of SHG, the ordinary refractive index at 2ω can be equal to the extraordinary refractive index at ω.

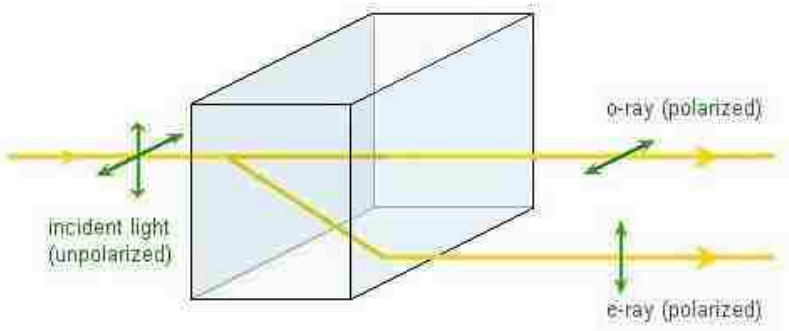

Figure 6. Schematic of birefringence [21].

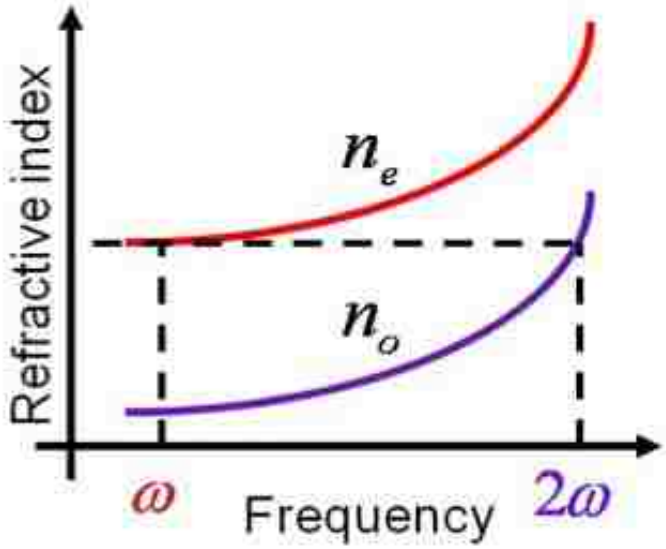

Figure 7. Phase matching of second-harmonic generation by using birefringent crystals [21].

1.2.4.2 Quasi-Phase-Matching

Another method for solving the phase-matching condition consists in the quasi-phase-matching method. The schematic of the concept is illustrated in Figure 8 in which the orientation of the crystals is flipped every coherence length by periodically stacking or poling crystalline domains.

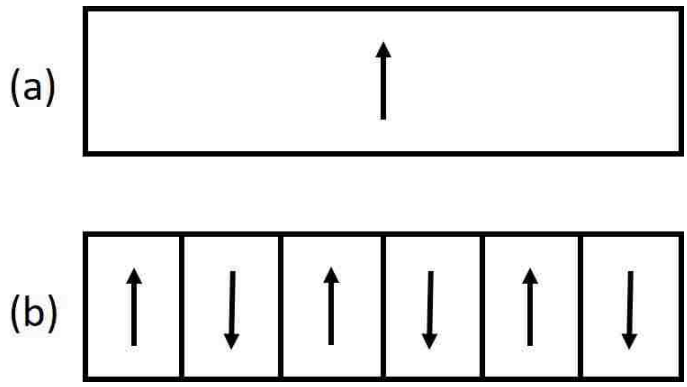

Figure 8. Schematic of (a) a homogeneous single crystal and (b) of a periodically-poled material.

From Figure 9, we can see that each time the electric field is about to decrease, the flipping of the crystalline orientation compensates for a nonzero wavevector mismatch, making the electric field grow continuously. In quasi-phase-matching, the intensity of the second order conversion signal is much higher than the wavevector mismatch and is comparable to the perfect phase-matching condition. The electric field is proportional to the number of grains and intensity is quadratically proportional with number of grains.

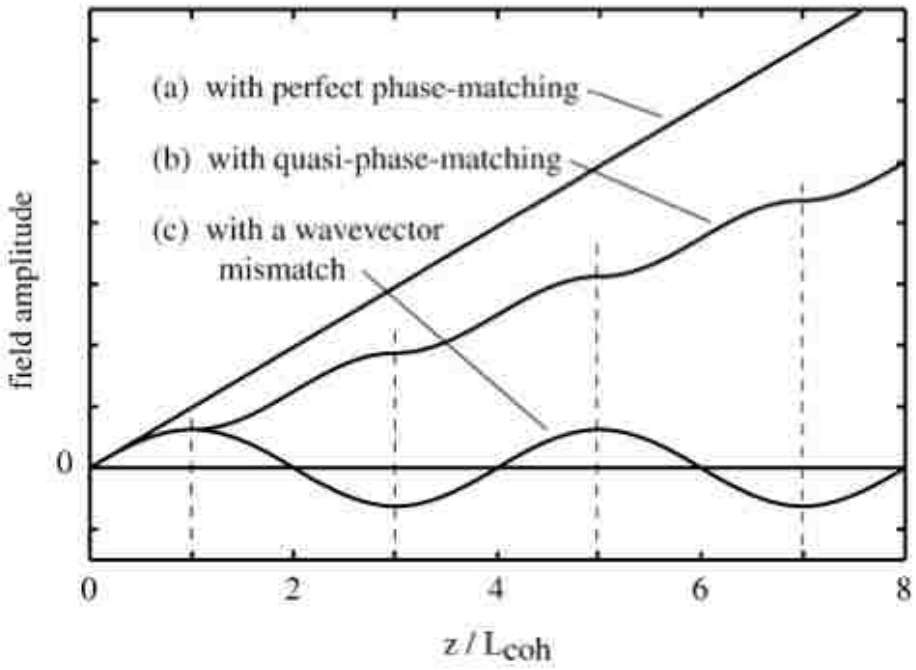

Figure 9. The electric field amplitude for wavevector mismatch, quasi-phase-matching and perfect phase-matching conditions [24].

There are many different ways to fabricate quasi-phase-matched structures. The very early one was proposed by Armstrong *et al.* in 1962 [25], who suggested slicing nonlinear optical materials into thin films and rotating the layers by 180 degrees. While feasible, this method is cumbersome and limited to the use of thick layers. An alternative approach, reported by Yamada *et al.* in 1993 [26], is to use an electric field to invert the orientation of domains in ferroelectric materials such as lithium niobate ($LiNbO_3$).

In the past three decades, the development of QPM techniques involving periodically-poled, diffusion bonded [27, 28] or epitaxially-grown materials, such as periodically-poled $LiNbO_3$ (PPLN) [29-31], orientation-patterned GaAs (OP-GaAs) [32, 33] or GaP (OP-GaP) [34-36], have been extensively studied. The inversion of the sign of the nonlinear coefficient eliminates destructive interferences and allows the generated intensity to grow quadratically with the sample

thickness. However, the techniques used to periodically flip the crystalline orientation remain fairly elaborate [37-39].

1.2.4.3 Random Quasi-Phase-Matching

A third alternative is to use transparent polycrystalline aggregates (ceramics). Despite the lack of long range order, these materials can serve as efficient nonlinear frequency converters by way of the random quasi-phase-matching (rQPM) process [40-46]. In these ceramics, the randomly-oriented crystallites all contribute to the nonlinear conversion process but with random phases and yet, the total contribution to the generated field is nonzero. Nonlinear conversion efficiency is maximized when the average grain-size of the ceramic is equal to the coherence length for the wavelengths of interest [47, 48]. The main feature of rQPM is frequency conversion depends linearly on the thickness of the sample. Although random quasi-phase-matching is less efficient than a phase-matched or quasi-phase-matched process, the difference is lessened in the femtosecond regime where short samples (<1 mm) are used. In addition, disordered polycrystalline media show a significant enhancement in spectral acceptance and tolerance to both propagation angle and temperature when compared to ordered crystals.

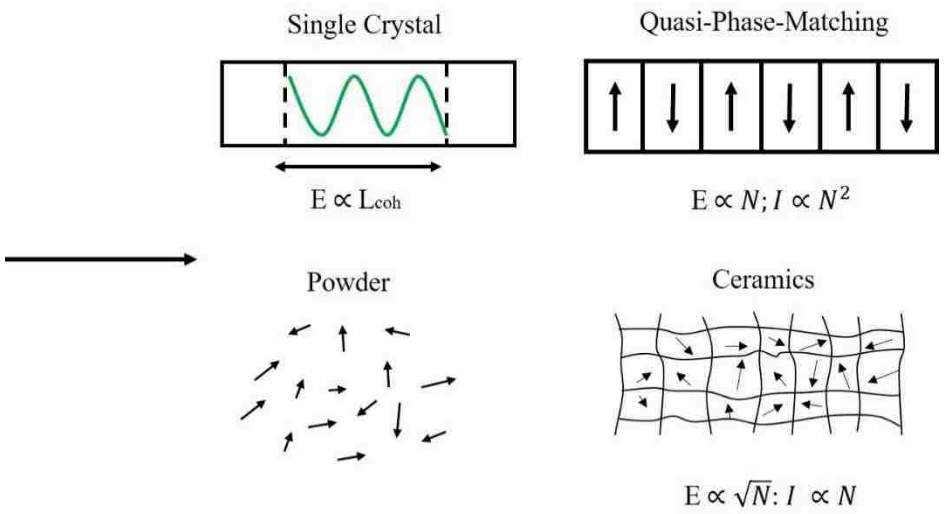

Figure 10. Three-wave mixing mechanisms in single-crystal, powder, quasi-phase-matching materials and polycrystalline materials.

In 2004, Baudrier-Raybaut *et al.* [42] found that the interaction of random phases in highly transparent polycrystalline materials can be an effective way to achieve efficient phase-matching in isotropic materials. Figure 10 shows the three-wave mixing mechanisms in single-crystal, powder, QPM materials and polycrystalline materials. In single-crystal, there is a phase-lag every coherence length which leads to a small conversion efficiency. In fully disordered materials, such as powders, each particle generates independent electric field and scatters the light in random directions. In polycrystalline materials, the randomly-oriented crystallites all contribute to the nonlinear conversion process but with random phases. The electric field is proportional to the square root of number of grains and intensity is linearly proportional to the number of grains. The concept of random quasi-phase-matching was experimentally demonstrated in a DFG experiment. As predicted, the difference frequency generation signal is linearly proportional to the sample thickness. For comparison, the DFG signal in ZnSe single crystal is also shown in Figure 11 and shows a periodically oscillation every coherence length.

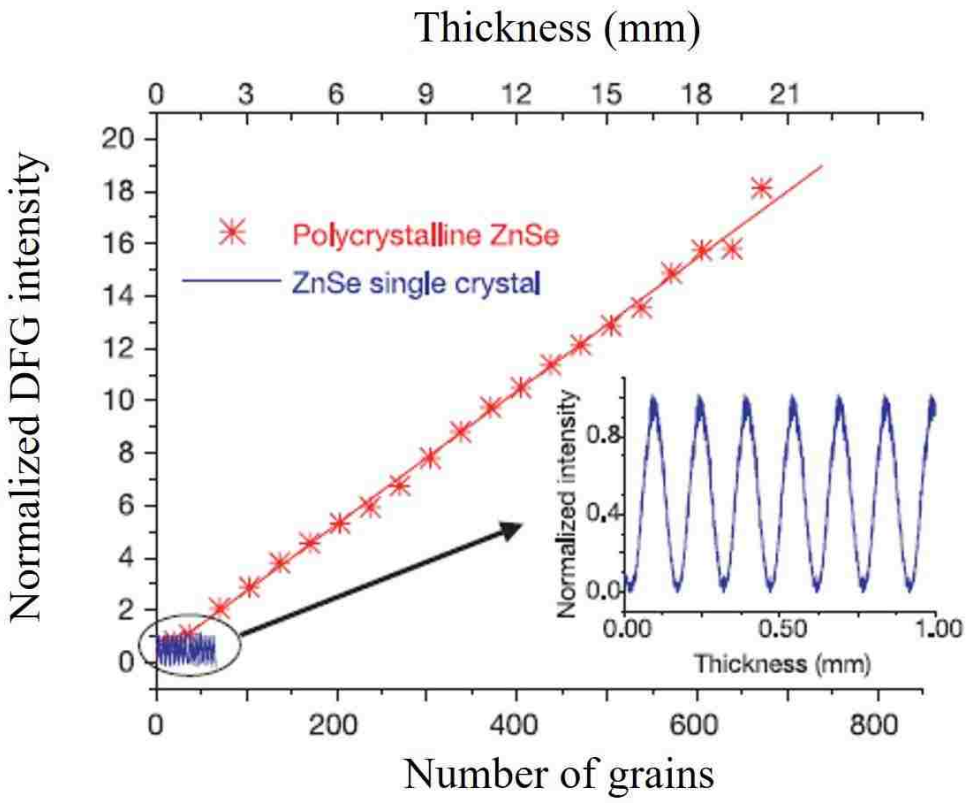

Figure 11. Normalized DFG intensity as a function of sample thickness.

In order to discuss the effect of grain size on the second-order nonlinear conversion efficiency, ZnSe ceramics with different average grain size were fabricated, from 30 microns to 100 microns. The average grain size of original ZnSe is 30 microns and the coherence length was calculated as 79 microns depends on the wavelength of input beams used in difference frequency generation experiment. Figure 12 shows the theoretical and experimental values of the normalized DFG efficiency for samples with different average grain size. From Figure 12, we can see that the nonlinear conversion efficiency is higher when the average grain size is close to coherence length, which is in good agreement with the theory.

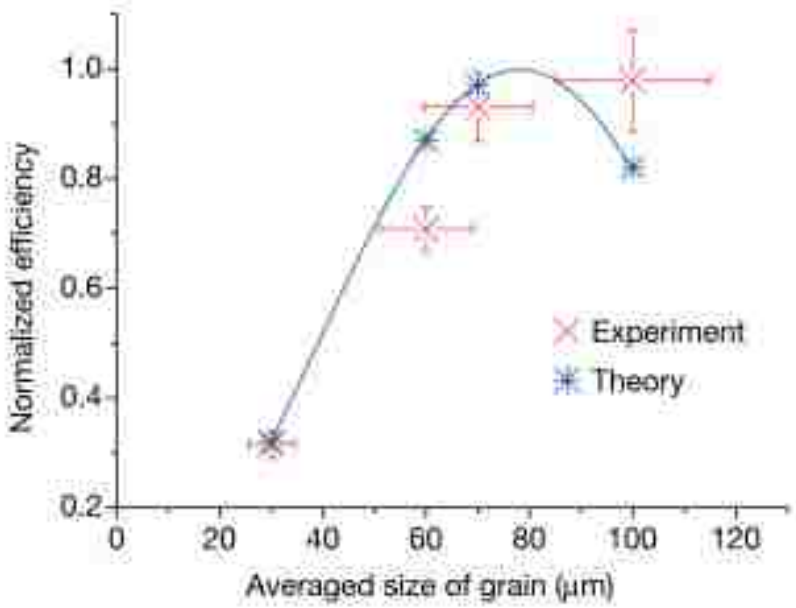

Figure 12. Normalized DFG efficiency as a function of average grain size. The coherence length is 78 μm [42].

Baudrier-Raybaut's study is the first paper talking about the rQPM in ZnSe polycrystalline transparent ceramics and experientially proves the main feature of rQPM, which is that the conversion efficiency is proportional to the sample thickness.

1.3 Nonlinear Transparent Ceramics

As discussed before, NLO materials should be non-centrosymmetric in order to have non-zero second-order susceptibilities. There are 21 non-centrosymmetric crystal symmetry classes out of 32 crystallographic point groups (Table 2). Table 3 lists some common nonlinear crystals with their crystallographic class. On the other hand, because rQPM in TOCs requires randomly oriented grains, the material must be optically isotropic to prevent Fresnel losses at the grain-boundaries. These requirements can be satisfied using either a pseudo-cubic or a cubic structure of non-

centrosymmetric point groups. Pseudo-cubic, it is defined by the approximate equality of the unit cell parameters $a \approx b \approx c$ and the interaxial angles $\alpha \approx \beta \approx \gamma \approx 90°$. For this reason, we have selected PMN-PT (point group 3*m*) and ZnSe (point group $\bar{4}3m$) as the pseudo-cubic and cubic test materials, respectively. PMN-PT is a well-known electro-optic (EO) material with nearly 100 times higher performance than $LiNbO_3$ at room temperature whereas the nonlinear properties are not characterized [49]. On the other hand, ZnSe has the broadest infrared transparency among all nonlinear optical materials and high second order nonlinearity and low group velocity dispersion.

Table 2 Crystallographic point-group symmetry (non-centrosymmetric point groups are shown in red).

Symmetry Class	Point Group
Triclinic	**1** $\bar{1}$
Monoclinic	**2** ***m*** **2/*m***
Orthorhombic	**222** ***mm*2** ***mmm***
Tetragonal	**4** $\bar{4}$ **4/*m*** **422** ***4mm*** $\bar{4}$***2m*** **4/*mmm***
Trigonal (Rhombohedral)	**3** $\bar{3}$ **32** ***3m*** $\bar{3}$***m***
Hexagonal	**6** $\bar{6}$ **6/*m*** **622** ***6mm*** $\bar{6}$***2m*** **6/*mmm***
Cubic	**23** ***m*$\bar{3}$** **432** $\bar{4}$***3m*** ***m*$\bar{3}$*m***

Table 3 Non-centrosymmetric point groups with examples of nonlinear crystals.

Symmetry Class	Point Symmetry Group	Nonlinear Crystals
Triclinic	**1**	
Monoclinic	**2**	BiBO
	m	$BaGa_4Se_7$
Orthorhombic	**222**	
	***mm*2**	KTP, KTA, RTP, RTA, $KNbO_3$, $AgGaGeSe_2$, LBO, $BaGa_4S_7$, $MgBaF_4$
Tetragonal	**4**	
	$\bar{\mathbf{4}}$	
	422	
	4mm	
	$\bar{\mathbf{4}}$***2m***	KDP, CLBO, $ZnGeP_2$, $CdSiP_2$, $AgGaS_2$, $AgGaSe_2$
Trigonal (Rhombohedral)	**3**	
	32	α-Quartz, Te, YAB
	3*m*	$LiNbO_3$, $LiTaO_3$, BBO
Hexagonal	**6**	
	$\bar{\mathbf{6}}$	
	622	
	6*mm*	CdSe, CdS, GaN
	$\bar{\mathbf{6}}$***2m***	GaSe
Cubic	**23**	
	432	
	$\bar{\mathbf{4}}$***3m***	GaAs, GaP, GaSb, InAs, InP, InSb, CdTe

1.4 Summary and Dissertation Outline

Non-centrosymmetric pseudo-cubic or cubic TOCs can be used as nonlinear media using the rQPM scheme. These materials would allow a significant enhancement in spectral and angular acceptances and a better tolerance in both propagation angle and temperature, which are essential in converting femtosecond laser pulses. In addition, nonlinear transparent ceramics would enable the generation of broader spectral bandwidth. This is in contrast to the QPM scheme whereby the periodic inversion of the nonlinear coefficient leads to a narrower bandwidth of efficiently converted frequencies. Despite a lower conversion efficiency, TOCs also have the advantage of being easier to fabricate and scale. However, matching the grain-size to the coherence length is crucial to the rQPM efficiency. **The objective of this thesis is to analyze the conditions for grain-size control in two test TOCs: PMN-PT and ZnSe that have potential rQPM applications**. In the case of PMN-PT, We have studied:

1) the fabrication of phase-pure ceramics,
2) the densification of transparent ceramics, and
3) the role of sintering additives in controlling the microstructure.

In the case of ZnSe and based on Baudrier-Raybaut's results, we have investigated:

1) an improved grain-growth method,
2) the effect of grain-size distribution on second order conversion efficiency, and
3) the possibility of generating broadband frequency spectra and converting short pulse by a nonlinear process.

This dissertation is divided into seven chapters. In **Chapter two**, the fabrication process of transparent PMN-PT ceramics is detailed. We also describe a novel combustion synthesis process to fabricate lead oxide nanopowders.

Chapter three presents the results of our study on the effect of sintering additives on the microstructure and phase-purity control in PMN-PT ceramics.

Chapter four summarizes simulation result on the second-order nonlinear susceptibility in pseudo-cubic PMN-PT.

Chapter five explores the non-stoichiometric grain-growth in CVDed ZnSe. In this work, solid-state grain-coarsening was used to fabricate ZnSe ceramics with the desired grain-size. The effect of these grain-size distributions on the efficiency of second-harmonic generation process by random quasi-phase-matching is analyzed theoretically.

Chapter six presents the rQPM SHG results obtained on our processed ZnSe ceramics and our ZnSe OPO, based on random quasi-phase-matching.

Finally, **Chapter seven** summarizes our results and offers suggestions to further study.

CHAPTER TWO: FABRICATION OF TRANSPARENT CERAMICS OF PMN-PT

2.1 PMN-PT Transparent Ceramics

$(1-x)Pb(Mg_{1/3}Nb_{2/3})O_3$-$xPbTiO_3$ belongs to the family of perovskite structure materials with the formula ABO_3 with a unit cell shown in Figure 13. The large Pb^{2+} cation occupies the A site at the corner of the unit cell whereas the small cations such as Mg^{2+},Nb^{5+},Ti^{4+} occupy the B site at the center of the unit cell. The oxygen ions are located at the center of the faces. The coordination number for the A sites is 12 and the coordination number for the B sites is 6. There are four A sites and two B sites cations directly bonded to each oxygen ion.

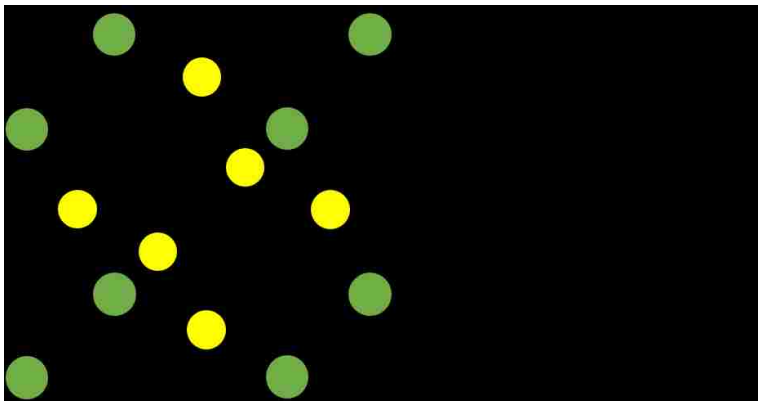

Figure 13. The perovskite structure ABO_3.

Figure 14 shows the phase diagram of (1-x)PMN-xPT. It has a rhombohedral structure (R*3m*) for $x < 0.3$ below T=400°C. In this region, solid solutions exhibit a relaxor behavior. For $x > 0.38$, solid solutions have a tetragonal structure (P*4mm*) and show a ferroelectric behavior. Between the rhombohedral and tetragonal phase domains, a variety of coexisting phases rhombohedral, tetragonal, but also orthorhombic and monoclinic symmetry defines the

morphotropic phase boundary (MPB) [50-52]. Giant piezoelectricity was reported in the MPB composition [53-55]. When the lead oxide concentration, x, is between 0.22<x<0.28 (highlighted in the red in Figure 14), PMN-PT exhibits a pseudo-cubic structure ($\alpha \approx \beta \approx \gamma \approx 89°56'$) of interest for our study. In this dissertation, we focus the composition x=0.25.

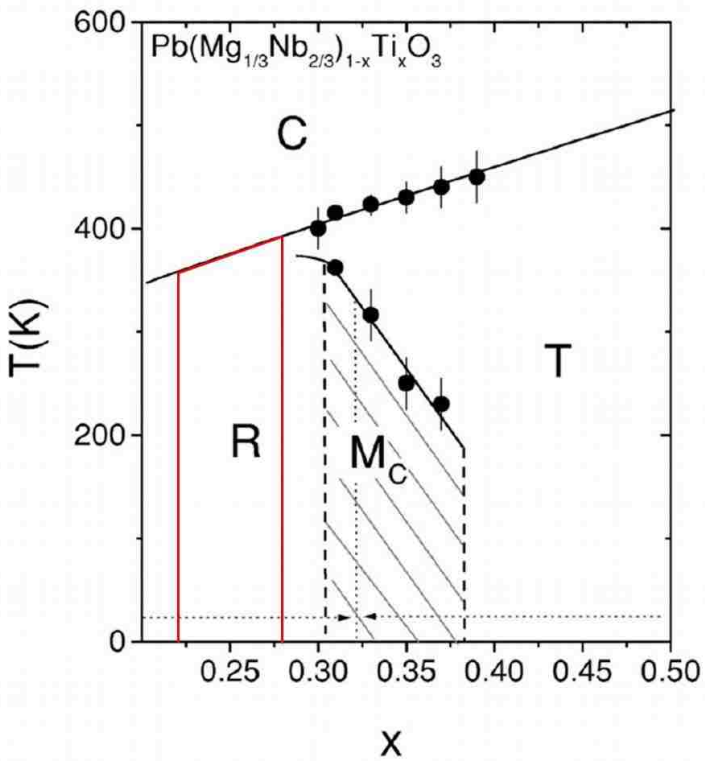

Figure 14. Phase diagram of PMN-PT [56].

PMN-PT ceramics have long been synthesized and studied, along with many other compositional analogs (such as PIN-PMN-PT, PZN-PT, PSN-PT, PYN-PT, PIN-PT where Z=Zr^{4+}, I=In^{3+}, S=Sc^{3+}, Y=Yb^{3+}) for high performance dielectrics and piezoelectrics, which have been reported by G.H. Haertling [15, 57] and W. Cao [58]. PMN-PT can be used as capacitors, sensors and electro-optical devices due to their high dielectric permittivity, high piezoelectricity, strong photo-refractive effect and high electro-optical coefficient. In the 1970s, PLZT ceramics

were fabricated using both pressure-assisted and pressure-less sintering techniques and exhibited at most 60% transmission in the visible for 0.5 mm-thick samples. More recently, optically transparent PMN-PT ceramics have now being sold as fast (sub-μs) electro-optical modulators (OptiCeramics^{TM}, Boston Applied Technologies, Inc., BATI) [49]. However, as we discussed before, grain-size control is very important in the rQPM process and the commercial materials do not provide a sufficient range of sizes. Assuming, SHG pumped at 4 μm, an approximate refractive index of n=2.43 at 4 μm and n=2.45 at 2 μm, we estimate that a useful grain-size of G=100 μm would be necessary. For this reason, we have investigated our own fabrication process to get transparent PMN-PT with controlled microstructure.

Figure 15. PMN-PT ceramics from Boston Applied Technologies, Inc. [49].

2.2 Ceramic Synthesis Routes

The optical transmission of the final ceramics is highly sensitive to the quality of the starting powders and sintering protocols. Soft mechano-chemical syntheses [59], sol-gel approaches [60], chemical co-precipitation methods [61], or “B-site precursor” methods [62] have

been reported to synthesize PMN-PT powders, but ceramics of this material have conventionally been prepared using reactive solid-state sintering [63-65]. The main challenge associated with the fabrication of high-quality PMN-PT is to avoid the parasitic pyrochlore phase ($A_2B_2O_7$, A and B metals). This pyrochlore phase not only decreases the dielectric and piezoelectric properties of the materials [66] but also degrades the optical transmission [49]. The reason of the formation of pyrochlore is the stereochemical activity of the $6s^2$ lone pair of Pb^{2+} tends to accommodate itself into an anion site and hence favors the formation of pyrochlore structure [67, 68]. In order to suppress this undesired pyrochlore phase, various methods have been proposed. The most effective method is to use $MgNb_2O_6$ (columbite) as the starting material [69, 70], which shows a similar octahedral structure with perovskite and helps form the PMN-PT perovskite pure phase at a lower temperature.

2.2.1 Powder Synthesis

Due to their high surface energy, powders with smaller particle sizes possess enhanced sinterability. It is therefore desirable to start with fine ceramic powders in order to produce pore-free ceramics. Very fine powders however, have a strong tendency to aggregate and pack inefficiently, leaving the green ceramics with macroscopic pores. Because of their size, these voids cannot be eliminated completely during sintering and powder compacts do not sinter to full density. For this reason, it is often preferred to sinter powders tens to hundreds of nanometers in size. Those powders can be synthesized via different routes, the most direct of which is a solid-state synthesis method. Concurrently to this method, we have also explored two other routes, which

provide better atomic scale homogeneity: the co-precipitation and the combustion synthesis methods.

2.2.1.1 Solid-State Synthesis

Commercially available lead oxide (PbO), magnesium niobate ($MgNb_2O_6$), and titanium oxide (TiO_2) powders were chosen for this synthesis. This pathway involving $MgNb_2O_6$ has been shown to lower the temperature for PMN-PT perovskite phase formation and prevent the formation of parasitic pyrochlore phase [71-73]. The different oxide powders were mixed by ball-milling in ethanol with zirconia ball as the grinding medium. Fine, pure and highly dispersed $MgNb_2O_6$ and TiO_2 powders are commercially available and relatively cheap, while PbO powder is only available in micron size and irregular shape as shown in Figure 16. The reaction is carried out at 850°C in an oxygen atmosphere to produce pure perovskite PMN-PT powders.

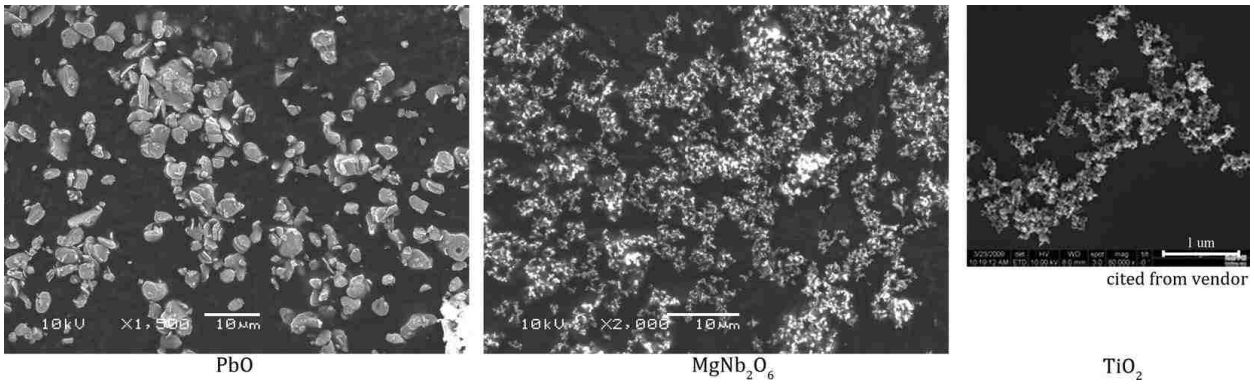

Figure 16. SEM images of raw oxide powders used in the solid-state synthesis method [74].

2.2.1.2 Co-precipitation Synthesis

In the co-precipitation method, Pb^{2+}, Mg^{2+}, Nb^{5+} and Ti^{4+} cations are dissolved in water from the salts $Pb(CH_3COO)_2 \cdot 3H_2O$, $Mg(NO_3)_2 \cdot 6H_2O$, $C_{10}H_5NbO_{20} \cdot 5H_2O$ and $C_{12}H_{28}O_4Ti$ respectively and precipitated by raising the pH with a base. When optimized, this ensures a good chemical homogeneity of the precipitate at the atomic scale. Nitric acid was used to adjust the pH of the starting solution and prevent the hydrolysis of Nb^{5+} and Ti^{4+} complexes. Ammonium hydroxide was used to increase the pH and precipitate the cations. We successfully produced powders with primary particle size smaller than 30 nm. However, this process leads to strong particle aggregation occurs during the calcination stage (Figure 17). XRD data reveals that, without the participation of $MgNb_2O_6$, it is difficult to form the perovskite phase by calcination at temperature below 800°C. The difficulty here is that the precipitating pH values of the various ions are widely different. Ti^{4+} starts to precipitate at pH=2, Nb^{5+} starts to precipitate at pH=4, Pb^{2+} starts to precipitate at pH=8 and Mg^{2+} starts to precipitate at pH=12. Hence, cations precipitate successively, which makes it difficult to get the perovskite phase, even in the presence of complexing agent such as EDTA.

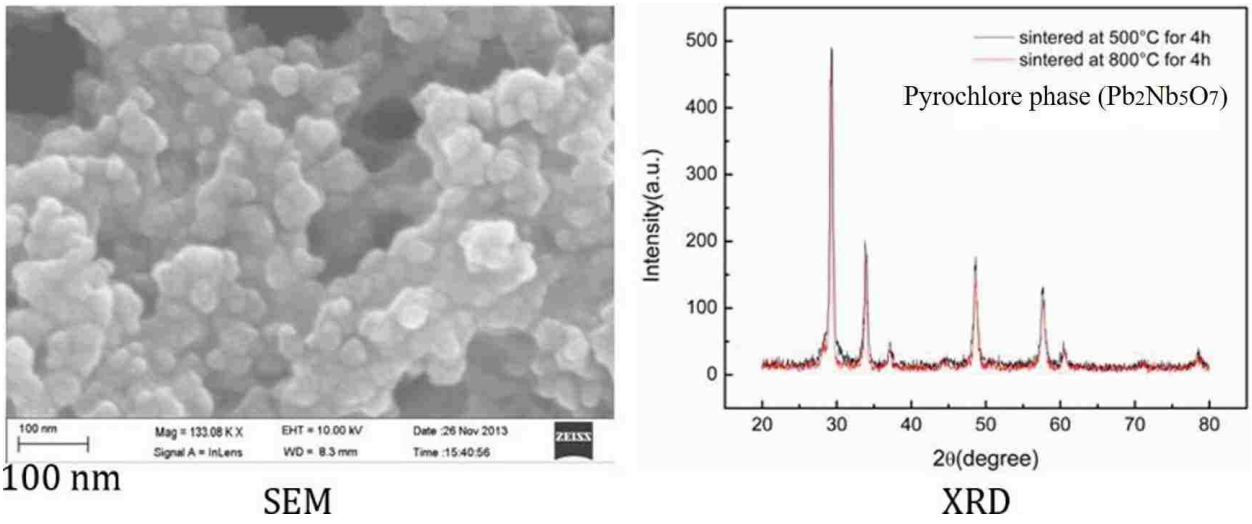

Figure 17. SEM and XRD images of co-precipitated PMN-PT powder.

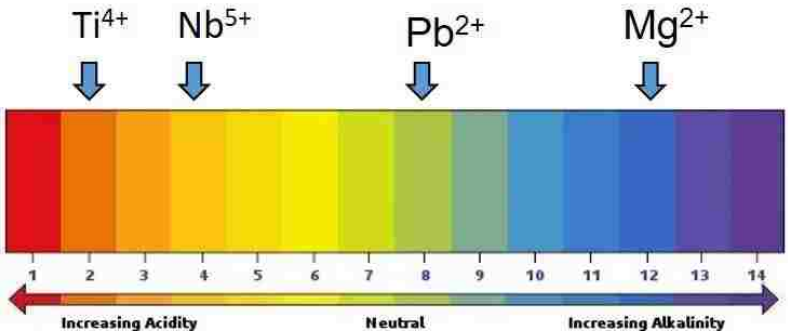

Figure 18. Precipitate PH value for cations.

2.2.1.3 Combustion Synthesis

In the combustion route, a clear precursor solution is prepared using the same method as for the co-precipitation procedure, except that glycine is added to the mixture. This solution is evaporated and the residue is ignited by further heating, glycine serving as a reducing fuel for the oxidizing nitrates during the combustion. The flame temperature is controlled by the ratio of glycine to nitrate. After combustion, the reaction products are collected in the form of a fine powdery soot. We found that, because of the large amount of nitric acid added to the solution in

order to maintain all cations in solution, it is difficult to regulate the ratio of the two reactants and control the flame temperature. As shown in Figure 19, the reaction products primarily contain the perovskite phase and some pyrochlore impurity. Post heat-treatment is hardly effective in converting the pyrochlore phase back to the perovskite.

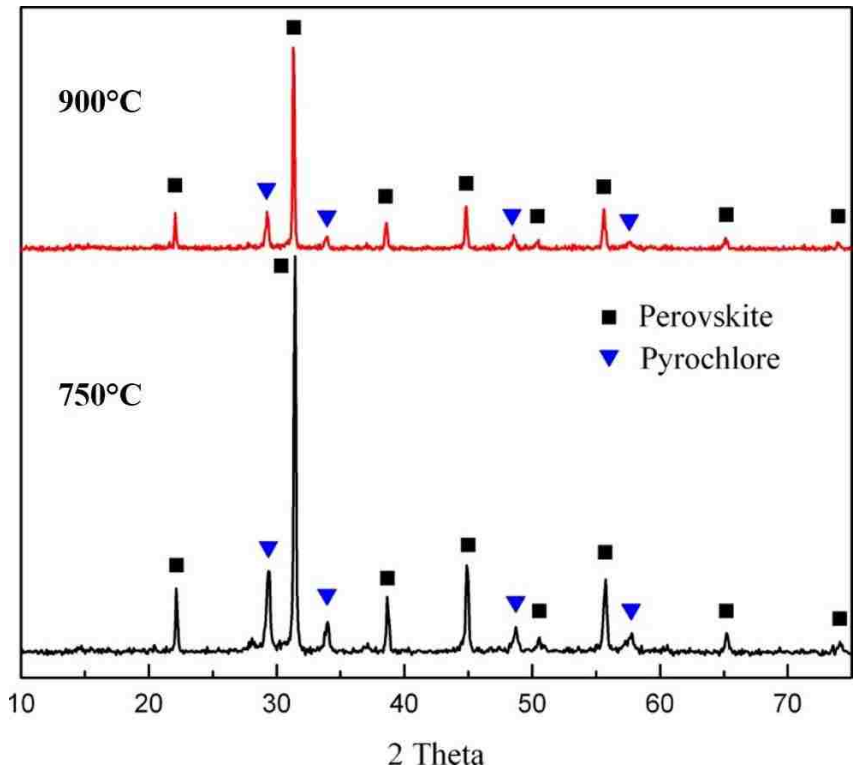

Figure 19. XRD image of the combustion synthesized PMN-PT powder.

2.2.2 Sintering Studies on Solid-State Synthesized PMN-PT Ceramic Powders

The standard procedure for producing ceramics includes ball-milling of the precursor oxides with 3 mm zirconia balls followed by sieving on a 200 mesh size sieve, a solid-state reaction to form pure perovskite PMN-PT, and a second ball-milling and sieving operation to remove agglomerates. The powder is then compacted and shaped by cold pressing at 200 MPa in an

isostatic press, pre-sintered, and finally hot-pressed. In the present work, 18 mm-diameter by 3 mm-thick pellets of PMN-PT powder (75PMN-25PT, 5 wt% excess PbO) were formed by cold-isostatic pressing and were subsequently sintered under various conditions. Consolidation method such as hot-press, conventional and two-step sintering was used for the densification and grain growth study.

2.2.2.1 Effect of the Sintering Atmosphere

Green-body samples were sintered in a tube furnace at different temperatures under oxygen atmosphere. The heating rate was 5°C/min and the dwell sintering time 4 h. 1000°C tube furnace pre-sintered ceramic were then placed in a graphite mold and sintered for 4 h in a graphite heating element hot-press furnace, with nitrogen atmosphere and 5°C per minute heating rate. Figure 20 shows the density of these PMN-PT ceramics after sintering. Upon inspection of Figure 20 and of the microstructures of those ceramics (such as Figure 21), we were able to conclude that the heating rate of 5°C/min for pressure-less sintering was too fast to obtain complete densification. At that rate, the grains grow faster than the rate at which the pores are eliminated, thus, the pores detach from the grain boundaries and become trapped inside the grains. Such intra-granular porosity is almost impossible to diffuse out and the ceramic stops densifying. At 1100 °C, the densification was hindered while the evaporation of lead continued.

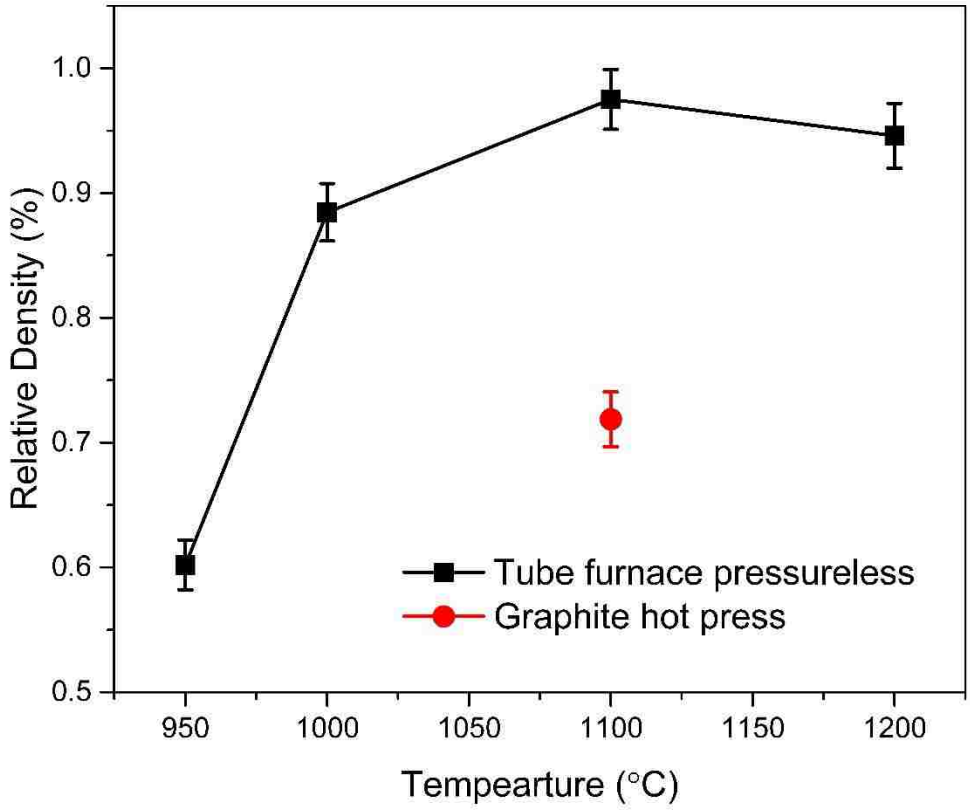

Figure 20. Densification of tube-furnace sintered and graphite hot-press sintered PMN-PT ceramics.

Soon after, we showed that a heating rate of 2.5°C/min is better suited for complete densification. Slower heating rate than 2.5°C/min did not result in enhanced density and lead to PbO loss by evaporation as per Eq. 14 below. Secondly, the density of the ceramic sintered at 1000°C decreased by 20% after hot-pressing at 1100°C in N_2 atmosphere and became strongly colored. This exemplifies the importance of the sintering atmosphere, as inert/reducing atmospheres promote the evaporation of PbO, the swelling of ceramics and the formation of color centers, as illustrated in Eq. 15:

$$Pb_3(MgNb_2)O_9\ (s) \rightarrow Pb_{3-x}(MgNb_2)O_{9-x}\ (s) + PbO\ (g) \quad (14)$$

$$PbO\ (s) \rightarrow PbO\ (g) \rightarrow Pb\ (g) + 1/2\ O_2\ (g) \quad (15)$$

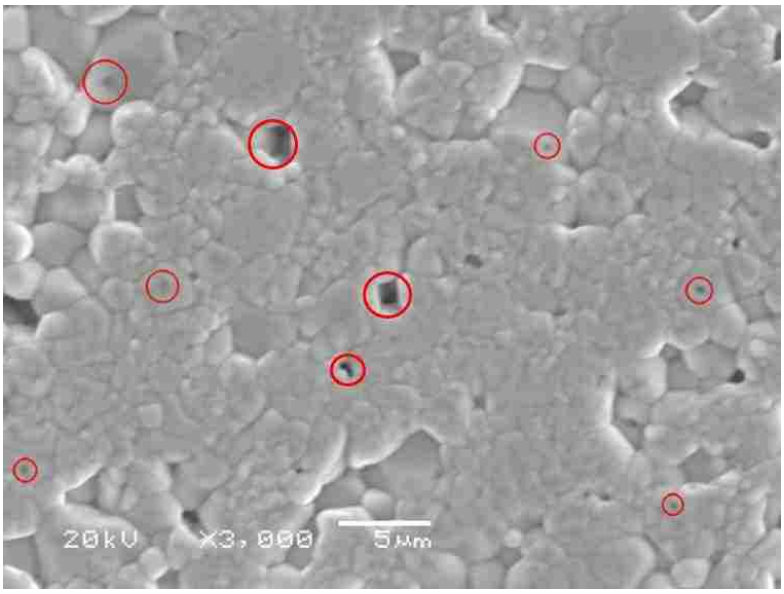

Figure 21. SEM image of a PMN-PT ceramic sintered at 950°C, 5°C/min showing remaining porosity (red circles).

As stated above, this material requires a high oxygen partial pressure in order to prevent PbO loss by volatilization. For these reasons, we have designed a dedicated hot-press capable of developing 100 MPa at a maximum temperature of 1200ºC in pure oxygen. This system is based on a floor-stand hydraulic press and on a commercial muffle box furnace with silicon carbide heating elements and a pressure molding set (Figure 22).

Figure 22. Photos of the hot-press with oxygen gas supply line in the back side of the furnace.

2.2.2.2 Characterization of Solid-State synthesized PMN-PT ceramics

SEM images of the microstructure surface of transparent PMN-PT ceramics still show intergranular and intragranular porosity. EDS mapping of the *L* transition of Pb (shown in blue color) indicates that the phase is chemically homogeneous at the sub-micron scale (Figure 23).

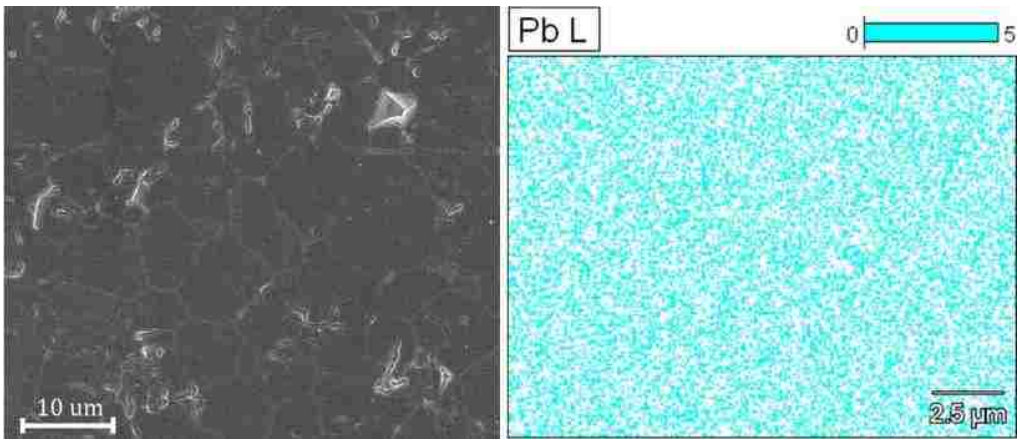

Figure 23. SEM and EDS of ceramics after hot-pressing.

The transmittance and photoluminescence of solid-state synthesized PMNPT transparent ceramic were measured. The samples were 2 mm thick, and as seen in Figure 24(a), the printed-paper under the ceramic samples can clearly be seen although the measured transmittance is still low (~30% at 1.5 μm). Some small residual porosity still exists in the samples and contributes to scattering losses. In Figure 24(b), the luminescence from the transparent ceramic excited at 405 nm is broad and strong, consistent with a charge transfer mechanism between a Pb^{2+} ion capturing a hole and a Ti^{4+} ion capturing an electron followed by charge recombination.

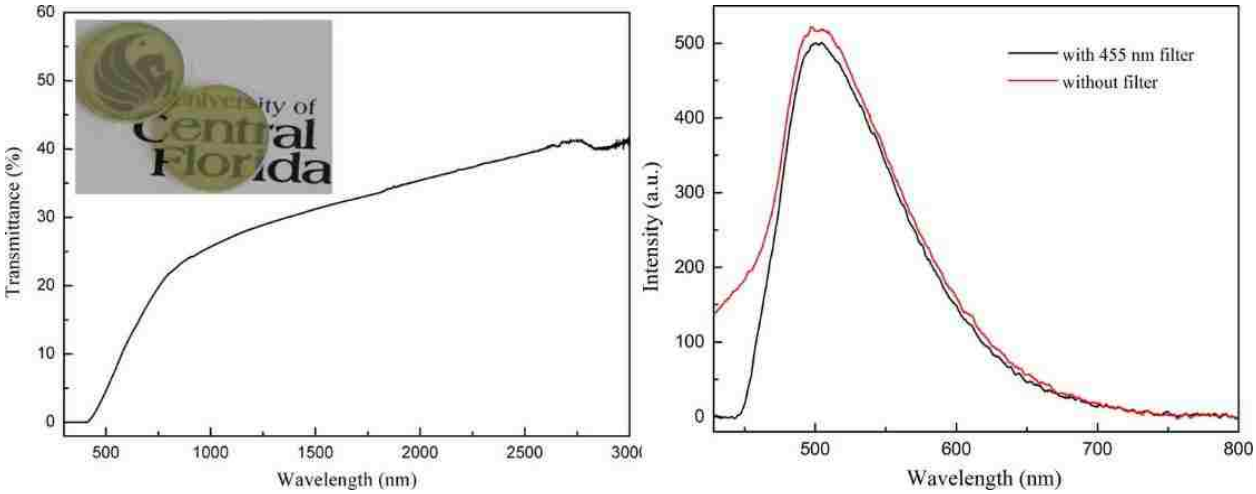

Figure 24. (a) Transmittance curve and inset photo of a 2mm thick PMN-PT ceramic; b) Photoluminescence of the ceramic under 405 nm laser excitation.

2.2.3 Novel Synthesis Approach Using Fine Lead Oxide Powders

The solid-state synthesized PMN-PT is translucent and the fabrication process is not optimal yet. Besides the sintering techniques, we can deal with raw materials to improve the transmittance. Fine, pure and highly dispersed $MgNb_2O_6$ and TiO_2 powders are commercially available and relatively cheap, while commercial PbO powder is only available in micron size and

irregular shape, which is not suitable to fabricate high-quality optical ceramics. There are several methods have been used to fabricate lead oxide nanoparticles like direct chemical synthesis [75], sonochemical method [76] and sol-gel pyrolysis method [77]. Among these available methods, combustion synthesis can produce uniform and ultrafine powders (normally less than 100 nm), which help reduce the sintering temperature [78-81]. The powder properties are highly dependent on the nature of fuel and of the fuel-to-oxidant ratio. The effects of different fuels and fuel-to-oxidant ratios on the powder properties have been extensively investigated by Chavan and Tyagi [82]and Bedekar [83] for many oxides. It is necessary to carefully control the fuel-to-oxidant ratio for getting the desired product [84]. The choice of the fuel is essentially determined by its ability to chelate metallic ions in solution. For example, the amino-acid glycine is a powerful complexing agent for a number of metallic ions [85] and has successfully been used to synthesize complex chromites [86], manganites [87], zirconates [88], ferrites, and oxide ceramics powders [89] because of its carboxylic acid function and amino group. In this work[1], we use glycine as the fuel and reductive agent while use nitrate as the oxidant. We fabricated lead oxide nanopowders by the glycine-nitrate process (GNP) and PMN-PT transparent ceramics by solid-state sintering based on the combustion synthesized lead oxide powders [90].

[1]These results have been published in Chen, X., Chen, S., Clequin, P. M., Shoulders, W. T., & Gaume, R. (2015). Combustion synthesis of lead oxide nanopowders for the preparation of PMN–PT transparent ceramics. *Ceramics International*, *41*(1), 755-760.

2.2.3.1 Experimental Procedure

In the combustion process, lead acetate trihydrate (99.999%, Aldrich) was used as the cation source. Glycine (≥99%, Aldrich) was used as a fuel and reductive agent while nitric acid (70%, Aldrich) was used as oxidant. We selected five different glycine-to-nitrate molar ratios (0.2, 0.5, 0.9, 1.3, 1.7) based on preliminary experiments. The required amount of $Pb(CH_3COO)_2 \cdot 3H_2O$ was dissolved in a quartz crucible with 50 ml of water. Solutions with different glycine-to-nitrate ratios were stirred for 20 mins and then heated on a hot-plate. Two-color optical pyrometer (Ircon, UX 70P) was used to measure the flame temperatures during combustion. After combustion, the powders were calcined at 420°C in oxygen atmosphere for 4 h, to remove trace of organic compounds and oxidized any metallic lead that may have formed. The temperature of 420°C is selected because it is under the melting points of lead oxides (888°C for PbO and 500°C for Pb_3O_4) and above that of lead (327°C). It was found that after calcination, the powder still contains lead and a subsequent heat treatment at 340°C was found effective to form lead ball which can then be removed from the oxide powder by sieving. Ball milling was used to deagglomerate the powders: a ratio of 8 g of grinding balls (ZrO_2) and 1g of ethanol per gram of powder was used for 20 h at 250 rpm. This mixture was dried in a vacuum oven at 60°C for 24 h and then sieved.

2.2.3.2 Results and Discussion

Auto-ignition of the lead acetate, glycine and nitric acid solution results in a voluminous ash. In order to fabricate PMN-PT ceramics with right stoichiometry, it is necessary to know the stoichiometry of the lead oxide produced by the combustion process. Hence, the powders were calcined at 420°C in an oxygen atmosphere for 4 h after combustion and try to shift the valence

state of lead to Pb^{2+}. Table 4 shows the reaction temperature, powder composition and yield as a function of the glycine-to-nitrate ratio. When glycine and nitrate are same amount, the reaction temperature is the highest and the yield is the lowest, which can be explained that more volatilization happened at high temperature. Phase composition can be determined by the X-ray diffraction pattern which is shown in Figure 25. In the following analysis, we only consider the powder obtained with 1.7 G/N ratio because the yield is much larger than powders achieved with other ratios. Table 5 shows the result of quantitative X-ray diffraction analysis on this powder. For the powder with 1.7 glycine-to-nitrate ratio, the yield is 87% and the phase composition is a combination of 73% PbO and 27% Pb_3O_4. Figure 26 shows the SEM images of lead oxide powders obtained with different glycine-to-nitrate ratios. The particles are highly agglomerated and the morphology of the particles vary from platelet-like at low G/N values (<0.9) while for higher G/N ratios, the particles are spherical with an average particle size of 60 nm.

Table 4 Effect of the glycine-to-nitrate ratio on powder composition.

Glycine: Nitrate	Reaction Temperature (°C)	Powder Composition	Yield (%)
0.2	640	Pb_2O_3+$PbO_{1.44}$	26
0.5	740	Pb_2O_3+$PbO_{1.44}$	10
0.9	-	PbO+$Pb_{12}O_{19}$	5
1.3	600	PbO+Pb_3O_4	78
1.7	590	PbO+Pb_3O_4	87

(Note: A very quick reaction was observed for the combustion process with 0.9 glycine-to-nitrate ratio and temperature cannot be measured with sufficient accuracy using two-color optical pyrometer.)

Table 5 Quantitative analysis the powder with 1.7 glycine-to-nitrate ratio.

Glycine: Nitrate	Powder Composition	Yield (%)
1.7	73%PbO+27%Pb_3O_4	87%

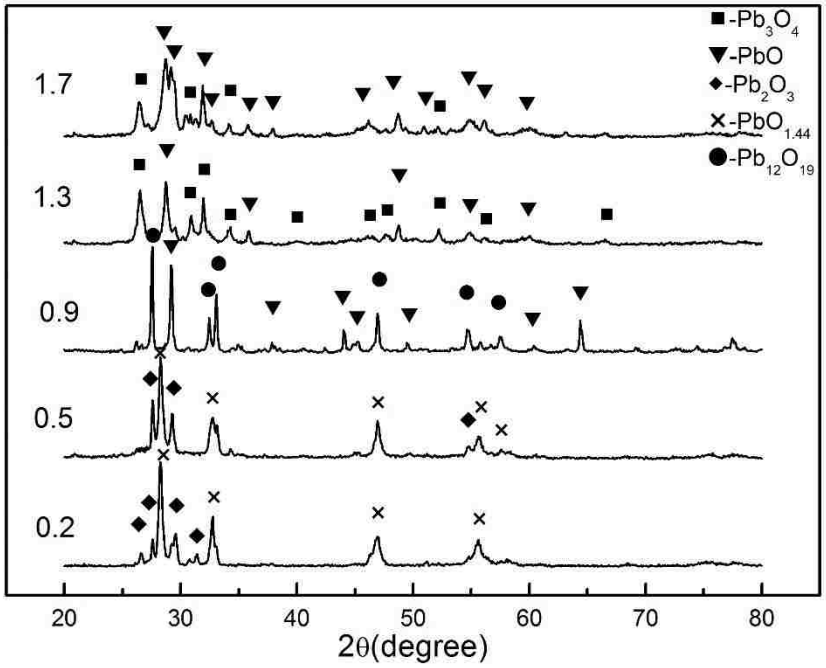

Figure 25. Powder X-ray diffraction of the powders with different glycine-to-nitrate ratios.

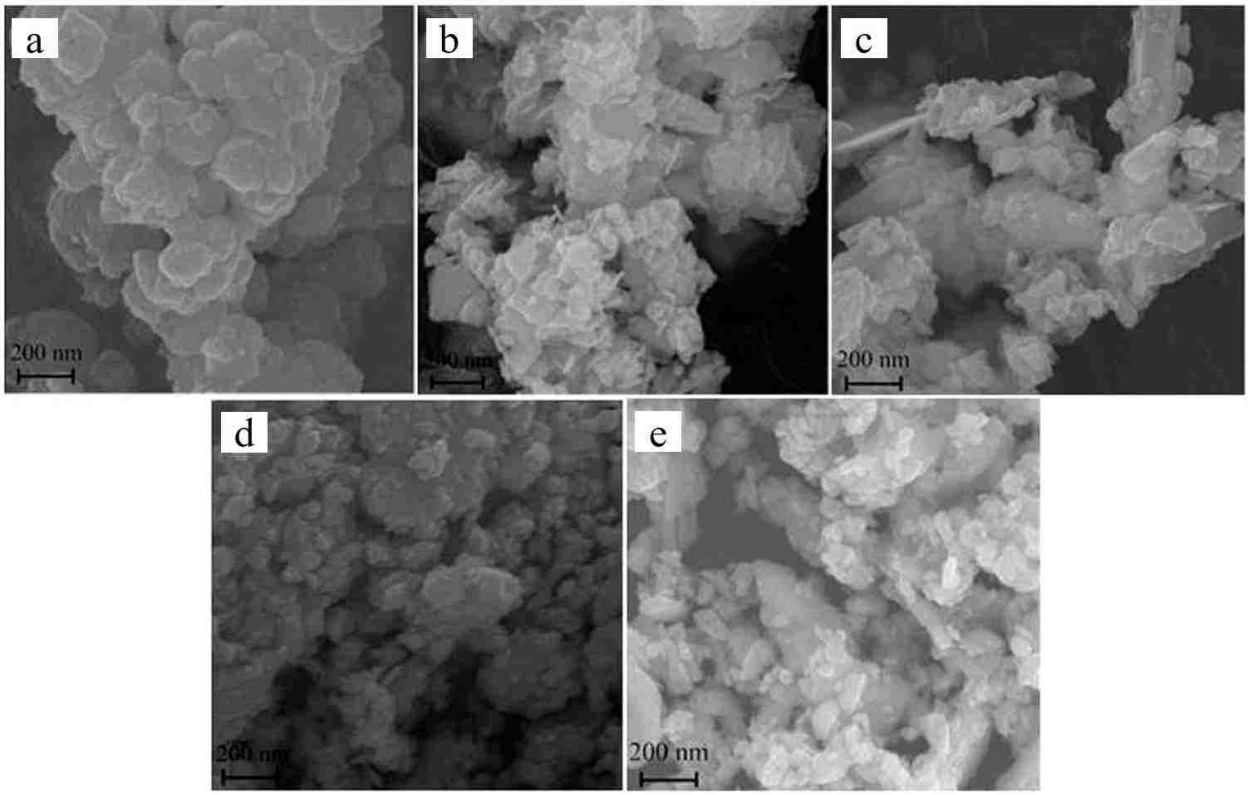

Figure 26. SEM of powders obtained with different glycine-to-nitrate ratios (a) 0.2; (b) 0.5; (c) 0.9; (d) 1.3; (e) 1.7.

As we can see, the lead oxide powder obtained with 1.7 G/N ratio is a combination of two different phases. To address this problem, we proceeded to a second calcination in order to oxidize all the lead and obtain single phase Pb_3O_4. For this second calcination, we use the same temperature as the first one but with a shorter time. We only increase the temperature to 420°C (about 10°C/min) slowly, and keep at 420°C for about 1 h. This calcination takes place under oxygen flow. Figure 27 shows the XRD of lead oxide powder before and after second calcination.

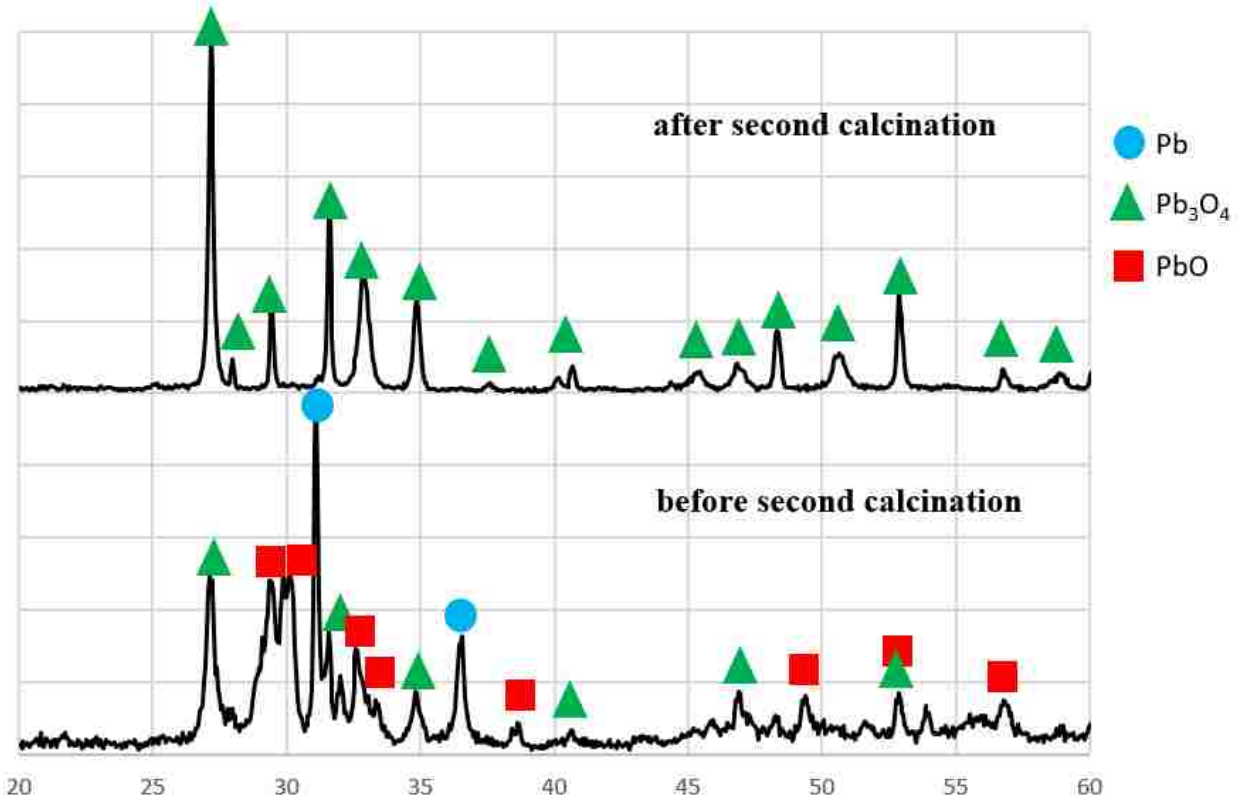

Figure 27. Powder X-ray diffraction of lead oxide powder before and after second calcination.

After second calcination, we got pure Pb_3O_4 phase nanopowders and the particle size does not show measurable coarsening and stay within 200 nm (Figure 28). We can also see a big color difference between these two powders since PbO has a yellow/pale red color and Pb_3O_4 has an intense orange color (Figure 29).

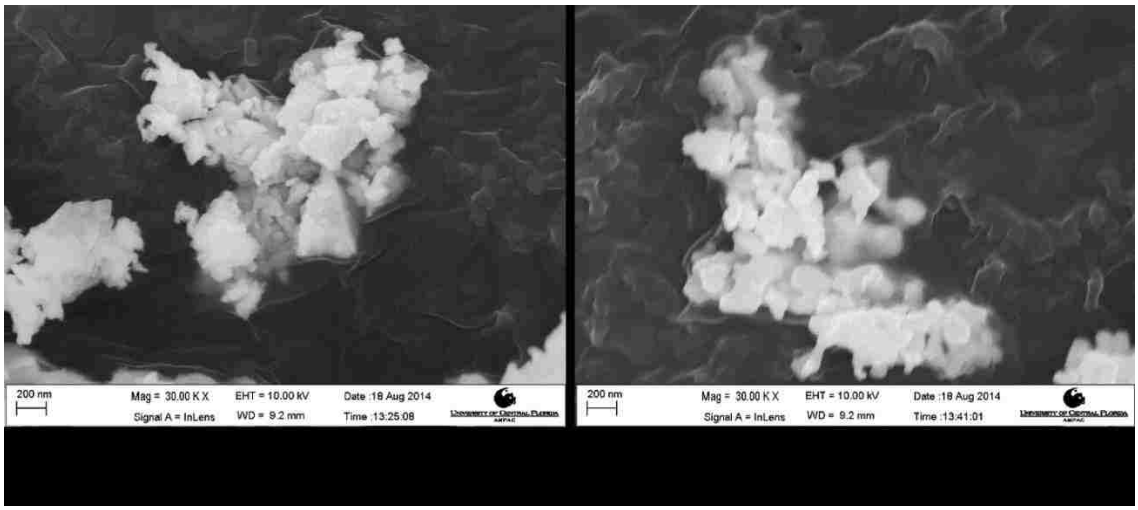

Figure 28. SEM images of lead oxide powder before and after second calcination.

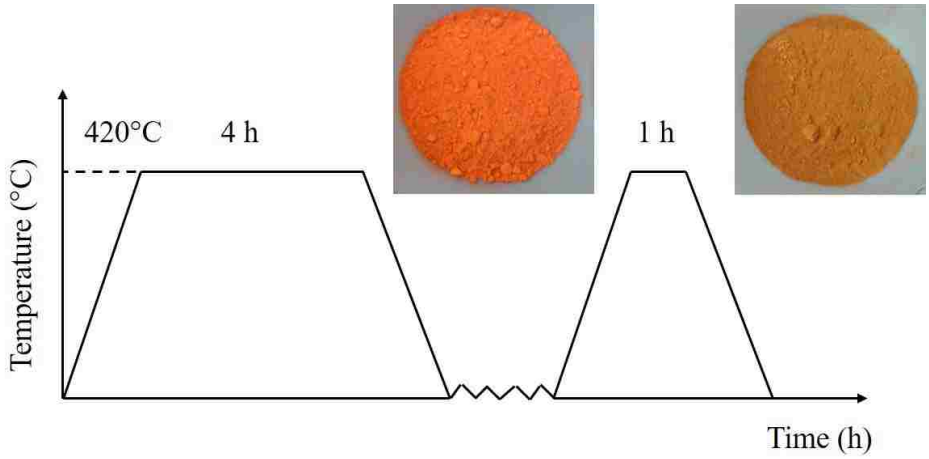

Figure 29. Photos of lead oxide powder before and after second calcination.

2.2.4 Fabrication of Transparent PMN-PT ceramics

Based on the discussion in section 2.2.3, we fabricated lead oxide nanopowders by combustion process with a 1.7 glycine-to-nitrate ratio. Then we fabricated PMN-PT transparent ceramics with composition $0.75Pb(Mg_{1/3}Nb_{2/3})O_3$-$0.25PbTiO_3$ doped with 3 at.% La. Magnesium niobate (H. C. Starck), titanium oxide (≥99.5%, Aldrich), lanthanum oxide (99.99%, Alfa Aesar) and combustion synthesized/commercial lead oxide were used as starting powders. An additional

3 mol % lead oxide were added to compensate the evaporation of lead oxide during sintering. These mixing powders were ball-milled for 20 h and pressed into pellets by uniaxial press and then followed by cold-isostatic pressing (CIP) at 200 MPa. The densification rate of the PMN-PT green-body fabricated with combustion synthesized lead oxide was measured by the Thermo-Mechanical Analysis (TMA) (Setaram, Dilatometry-System evolution) (Figure 30). We found that the densification is three times higher than that of a PMN-PT green body made with commercial lead oxide. PMN-PT ceramics were sintered in a tube furnace at 800°C for 4 h and followed by a dwell at 1150 °C for 4 h in an oxygen atmosphere. X-ray diffraction pattern of the ceramic shows a pure perovskite phase after reactive sintering (Figure 31). In order to check the microstructures, we polished the samples with alumina polishing slurry and thermal etched at 800°C for 30 mins. Figure 32 compares the microstructures of PMN-PT ceramics made with combustion synthesized lead oxide and commercial lead oxide. The grain size of ceramic made with combustion synthesized lead oxide is 3 μm, which is smaller than that of ceramic made with commercial lead oxide (9 μm). The former is also fully densified while the latter still has some intergranular and intragranular porosities, which degrade the transparency of the ceramic as we can see in Figure 33. In conclusion, lead oxide powders synthesized by combustion method have smaller particle size than commercial powders, which help promote the densification of green-bodies and improve the transparency of PMN-PT ceramics.

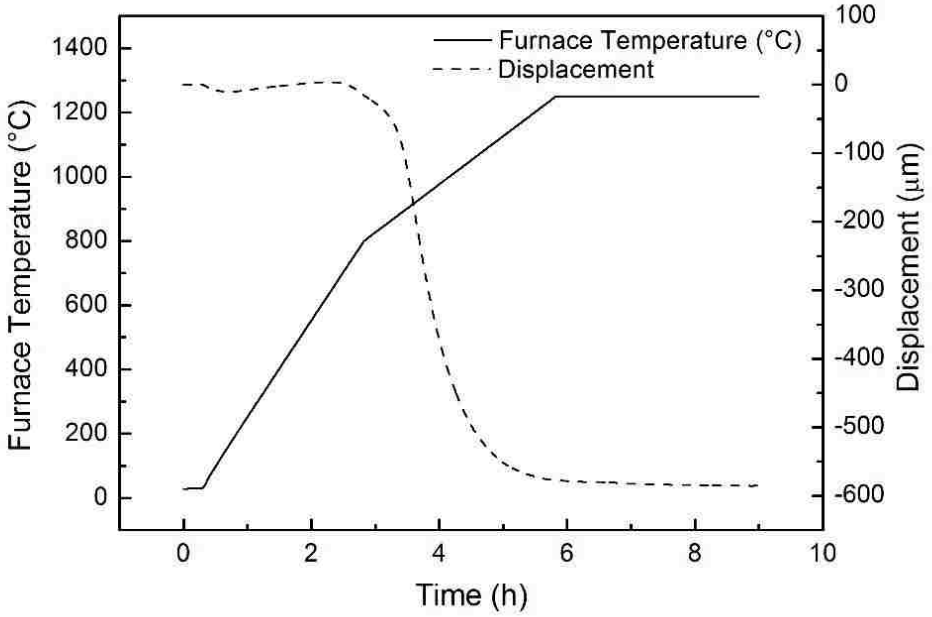

Figure 30. Thermo-Mechanical Analysis of PMN-PT green body made from combustion-synthesized lead oxide.

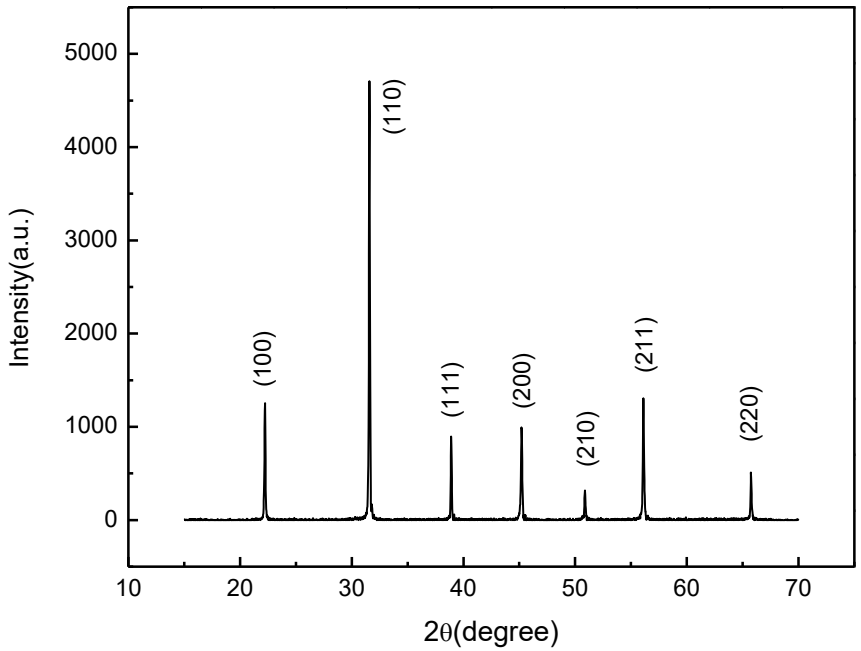

Figure 31. X-ray diffraction of PMN-PT ceramic made from combustion-synthesized lead oxide.

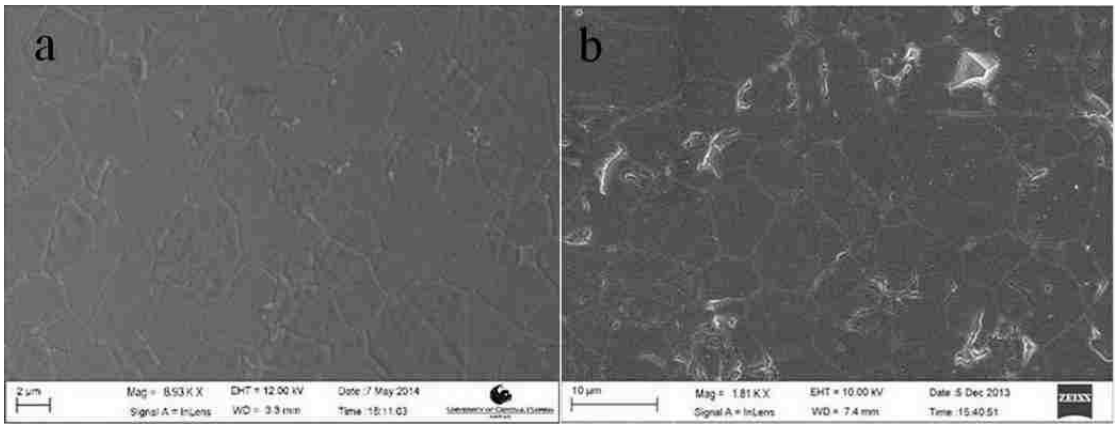

Figure 32. SEM images of PMN-PT ceramics made from (a) combustion-synthesized lead oxide and (b) commercial lead oxide.

Figure 33. Photographs of PMN-PT ceramics made from (a&b) combustion-synthesized lead oxide; (c&d) and from commercial lead oxide.

2.3 Comparison between In-house and Commercial Samples

In order to check the difference between home-made PMN-PT and commercially available PMN-PT, we carried out a direct comparison of physical properties and optical performance. We were provided a transparent PMN-PT sample from Boston Applied Technologies, Inc. (BATI)

with unspecified composition, which has better transmittance than our home-made sample. In order to improve the performance of our sample, we performed comparative characterizations including energy dispersive X-ray spectroscopy (EDS), X-ray diffraction (XRD) and Raman spectroscopy on these two samples.

2.3.1 Energy Dispersive X-ray Spectroscopy

The results of comparative elemental quantification by EDS suggest that the amount of lead in the commercial sample is less than that of our (UCF) sample. Extra lead may form a liquid phase at grain boundary during sintering, which influences the grain growth and densification. The formulas of those two samples are slightly different. By varying the composition in the PMN-PT material system, the interaxial angle of rhombohedral structure may be different and leads to different second-order nonlinearity.

Table 6 EDS results obtained on BATI and UCF samples.

	O (at. %)	Mg (at. %)	Nb (at. %)	Ti (at. %)	Pb (at. %)	Corresponding formula
BATI	60.96	5.00	11.89	4.09	18.06	0.78PMN-0.22PT
UCF	60.00	5.00	10.00	5.00	20.00	0.75PMN-0.25PT

2.3.2 X-ray Diffraction Analysis

With the assistance of sensitive X-ray optics on PANalytical Empyrean XRD system, small changes in lattice spacing can be measured for a better understanding of structural property

differences between samples. From the strain data in Figure 34, it is clear that two UCF samples are experiencing enlarged lattice spacing and a large amount of residual tensile stress, whereas the sample obtained from BATI possesses slightly decreased lattice spacing and compressive stress. The presence of residual stress in our samples might result in stress-induced birefringence and degrade the optical transmission. Figure 35 shows the lattice spacing shift between BATI and UCF samples. However, both ion doping and residual stress can cause the variation of lattice spacing. Considering that ion radius of 12-fold coordinated Pb^{2+} and La^{3+} are 1.49Å and 1.06Å respectively, a decrease of lattice spacing is expected as is the case in BATI sample. Therefore, we can make the conclusion that, there is no or negligible residual stress in BATI's sample, while there are residual tensile stress with values larger than we have calculated in our samples.

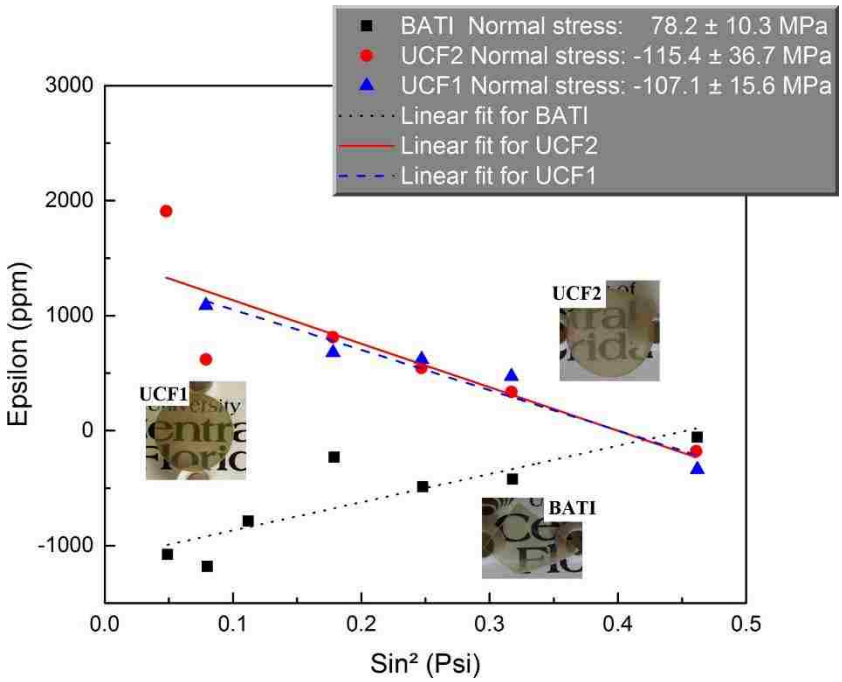

Figure 34. Strain data of BATI and UCF sample.

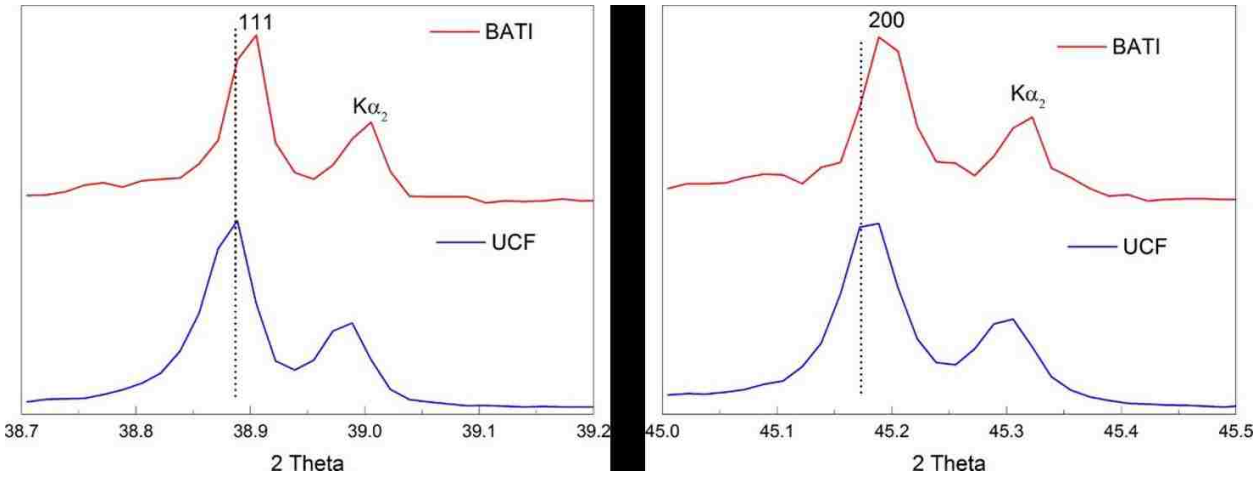

Figure 35. Shift of lattice spacing of BATI and UCF sample.

2.3.3 Raman Spectroscopy

Raman spectroscopy (Figure 36) reveals relatively broad overlapping bands, which are typical for perovskite relaxor ferroelectric materials. The excitation wavelength is 515 nm. The Raman spectra shows similar result with previous work on 0.81PMN–0.19PT [91]. There are three bands centered near 780, 580 and 270 cm^{-1}, which corresponds to Nb-O-Mg stretching mode, oxygen bending vibration and B-site ion against O stretching vibration inside the octahedral, respectively.

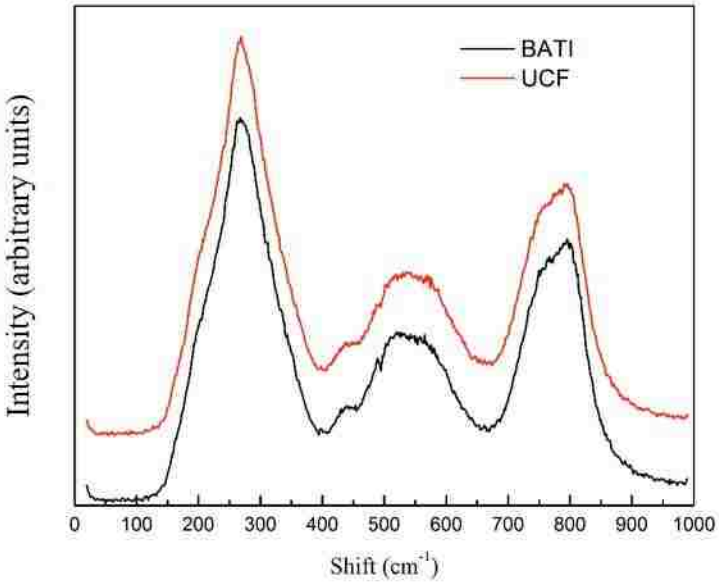

Figure 36. Raman spectroscopy of BATI and UCF sample.

CHAPTER THREE: EFFECT OF DOPANTS ON THE PHASE-PURITY AND MICROSTRUCTURE CONTROL IN PMN-PT CERAMICS

In general, dopants present in sufficient quantities can have a dramatic effect on the microstructure and crystal chemistry, and directly influence the properties, like dielectric, ferroelectric, piezoelectric and electro-optics properties [92, 93]. Dopants can enhance sinterability and suppress abnormal grain growth, which help fabricate ceramics with high density and controlled grain size. Dopants in PMN-PT raise an interesting situation for they can behave as charge donors or acceptors, depending on the site they occupied. In 1989, Zhilun [94] reported that ceramics with excess PbO in PZT-PNN family could be sintered at 900°C, which is lower than the normal sintering temperature 1200°C and the properties are improved [95]. They concluded that low-melting frits will form a liquid phase during early and middle stage of sintering, which promotes densification. However, the additives may enter the lattice during the final stage of sintering, which will modify the properties. In a system containing the PMN composition, too high sintering temperature and too long sintering time will lead to a second phase because of the evaporation of PbO. The second phase (pyrochlore) degrades the dielectric properties and also the transparency of the ceramics. Thus, excess PbO helps inhibit the formation of pyrochlore phase. The sintering aid lanthanum (La^{3+}), which is widely used in the fabrication of transparent PMN-PT ceramics, promotes the overall transparency by aiding the densification and by promoting the formation of the pure perovskite phase [96-98]. However, the mechanism by which lanthanum controls grain growth and favors full densification is not fully known. In this chapter, we are going to address this question by comparing the effect of various dopants on phase and microstructure evolution in 0.75PMN-0.25PT ceramics [99]. Ionic radius and valence are two aspects that may

influence the potency of dopants to promote densification and ultimately improve the transparency of ceramics. In order to illustrate the effect of radius on grain growth control and site occupation, Gd^{3+} and Y^{3+} were chosen to compare with La^{3+} because both of them have the same valence as La^{3+}. Ba^{2+} was considered based on previous work in PLZT transparent ceramics, which have same structure with PMN-PT [100]. 0.75PMN-0.25PT ceramics with different dopants were sintered at different temperature. The influence of dopants on the phase purity, densification behavior and microstructure evolution were investigated[2].

3.1 Experimental Procedure

Lead oxide (PbO, 99.9%, Alfa Aesar), magnesium niobium oxide columbite ($MgNb_2O_6$, 99.9%, H.C. Starck) and titanium oxide (TiO_2, ≥99.5%, Aldrich) powders were used as starting materials for the preparation of 0.75PMN-0.25PT ceramic samples. 3 mol% dopants were added in the form of lead oxide, barium oxide (99.99%, Aldrich), lanthanum oxide (99.99%, Alfa Aesar), yttrium oxide (99.9%, Alfa Aesar) or gadolinium oxide (99.99%, Alfa Aesar). An additional 3 mol% lead oxide was added to compensate the evaporation during the sintering. The powders were mixed with ethanol and ball-milled with zirconia balls for 20 h. After ball-milling, the slurry was dried at 80°C in an oven and the powders were sieved through a 200-mesh screen. Pellets were pressed into shape by uniaxial press and followed by cold-isostatically pressed at 200 MPa. The green-bodies were pre-sintered at 850°C for 2 h, and followed by sintering at different

[2]These results have been published in Chen, X., Chen, S., Bruner, A., & Gaume, R. (2018). Effects of dopants on the microstructure and phase-purity control in PMN-PT ceramics. *Ceramics International*, *44*(15), 17909-17913.

temperatures (850, 950, 1050, 1150, and 1250°C) for 4 h in pure oxygen. Archimedes' method was used to measure the densities of the samples and deionized water was used as the immersion medium. X-ray diffraction (PANalytical Empyrean) was used to check the phase composition of the ceramics while their microstructures were observed by scanning electron microscopy (Zeiss, Ultra-55). The grain sizes were measured by the linear intercept method (more than 200 grains counted) using ImageJ (National Institute of Health) from the SEM images. The SEM microstructures were obtained on unpolished ceramics in order to prevent damage and the contamination by abrasives of porous samples.

3.2 Results and Discussion

3.2.1 Transient Liquid-Phase Sintering

X-ray diffraction is used to check the phase content of 0.75PMN-0.25PT ceramics with different dopants at different sintering temperatures (Figure 37). A platinum foil was placed on the top of samples and used as an internal standard. X-ray analysis was performed after considering the correction of the instrument shift. Ba-doped samples show the same phenomenon as the Pb-doped samples at different sintering temperatures. La-doped PMN-PT is peculiar as pure perovskite phase regardless of the sintering temperature. All samples except La-doped samples show a liquid phase in the intermediate stage because of the excess PbO [101, 102]. The capillary force induced by the liquid phase on the solid particles contributes to densification and this may be the reason why densification proceeds at a lower temperature with these dopants (Figure 38). On the other hand, the slow densification rate of La-doped samples helps maintain an open porosity network and favors the outgassing of the initial excess of PbO, which contributes to the formation

of phase pure PMN-PT at a temperature as low as 850^{o}C. At 1150^{o}C, PMN-PT perovskite phase is the only remaining phase for all samples. However, excessive evaporation of lead results in perovskite decomposition and the formation of columbite, as in the case of Y-doped PMN-PT samples at 1250^{o}C. At 1250^{o}C, the final relative densities of all samples are greater than 98%.

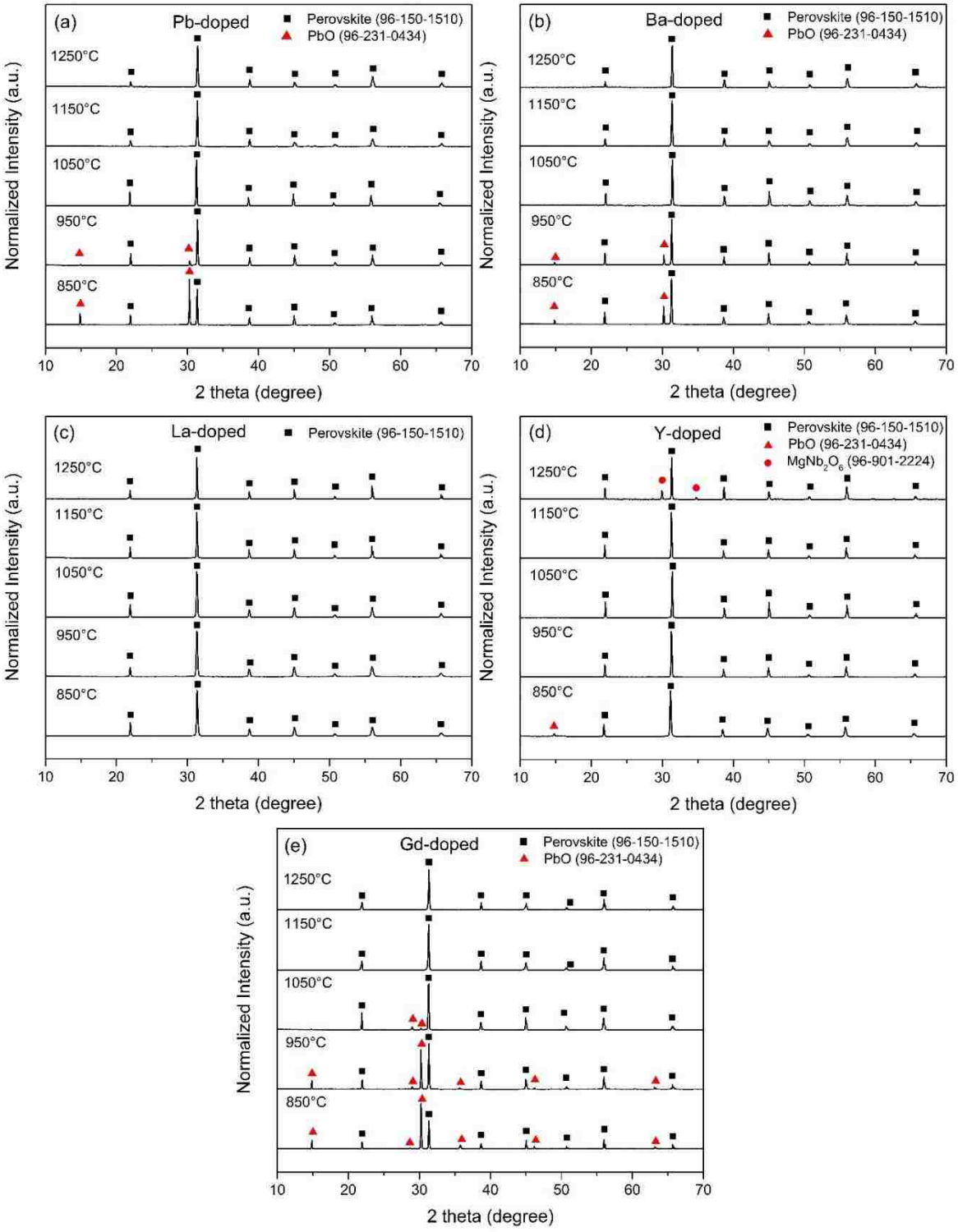

Figure 37. X-ray diffraction of 0.75PMN-0.25PT ceramics doped with (a) Pb^{2+}, (b) Ba^{2+}, (c) La^{3+}, (d) Y^{3+} and (e) Gd^{3+}.

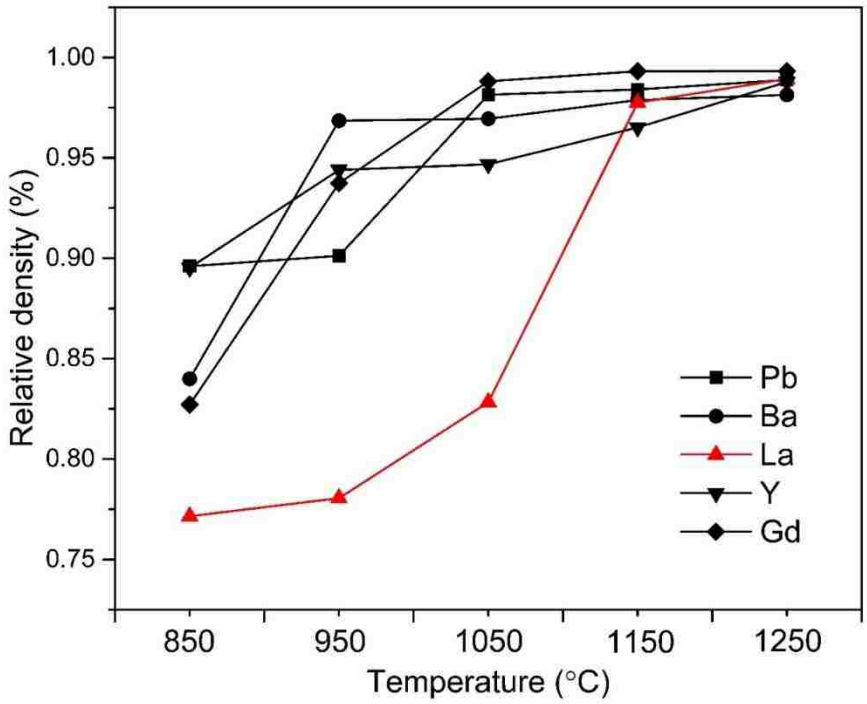

Figure 38. Densification of 0.75PMN-0.25PT ceramics with different dopants as a function of sintering temperature.

3.2.2 Microstructure Evolution

It is well known that the presence of a liquid phase will influence the microstructure, not only the size but also the shape of the grains. Figure 39 shows the microstructures of ceramics with different dopants at different sintering temperatures. As what we see in the SEM images, all samples except the La-doped samples produce faceted grains. Ba^{2+} and Pb^{2+}-doped samples exhibit same microstructure evolution between 850 and 1250°C. In the case of Y^{3+} and Gd^{3+} doping, faceted grains appear at 1050°C. This implies that, for these dopants samples, nonstationary grain-

growth governs the development of the microstructure. Nonstationary grain growth happens under the condition:

$$\frac{\sigma_s}{h} > \gamma_{sl} \tag{16}$$

Step free energy, σ_s, which is the energy per unit length of the edge of a nucleus formed on a flat surface. *h* stands for the step height and γ_{sl} is the solid-liquid interfacial energy [103]. However, La-doped PMN-PT did not present a liquid phase during sintering compared with other doped samples. One potential explanation is that the solid-vapor interfacial energy for La-doped samples, which is larger than the solid-liquid interfacial energy under good wetting condition, dominates the ratio of step free-energy to step height (Figure 40). So the condition for non-stationary grain growth is not satisfied in La-doped samples. This helps produce a uniform grain-size distribution and eventually enhance the transparency of the samples.

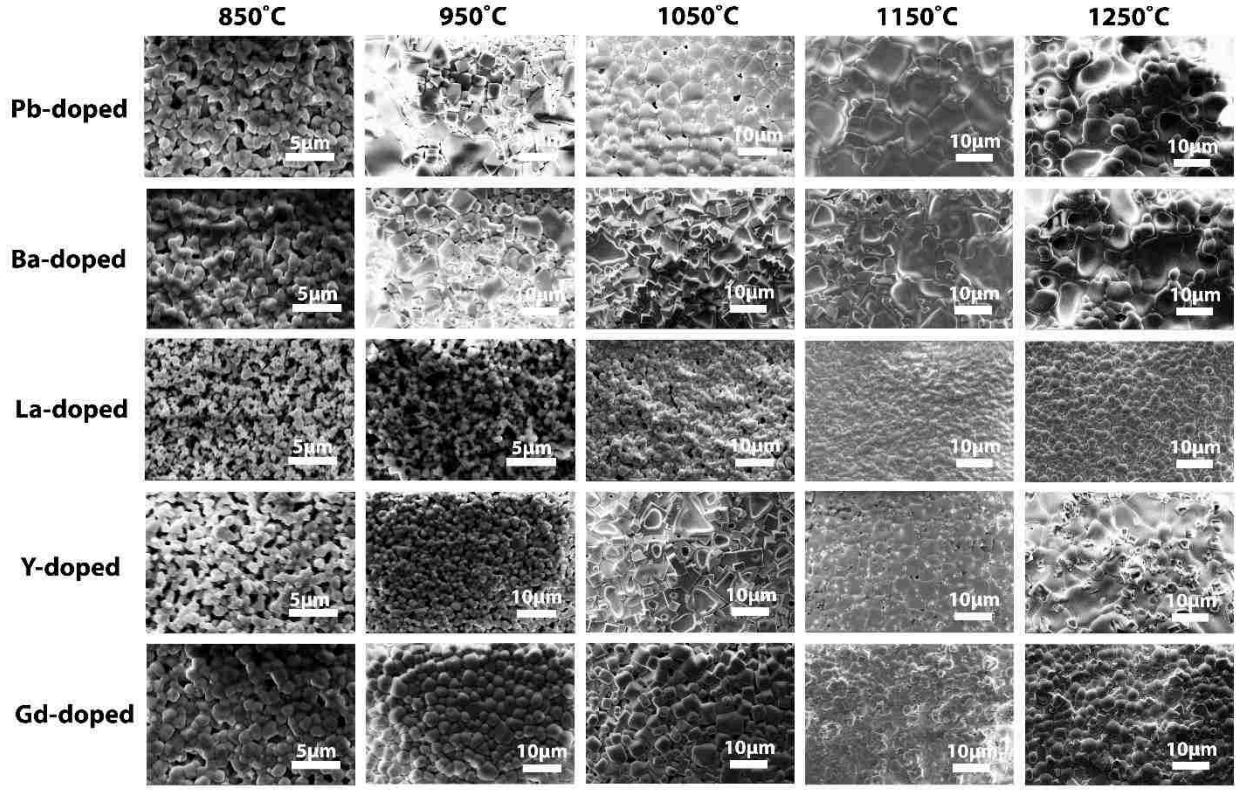

Figure 39. SEM of 0.75PMN-0.25PT ceramics with different dopants sintered at different temperatures.

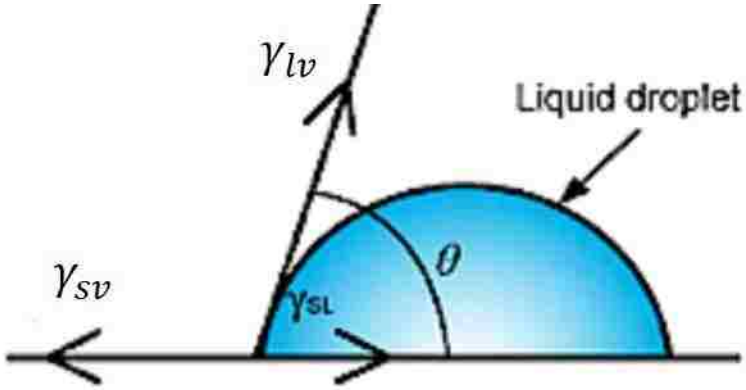

Figure 40. Contact angle for a liquid droplet on a solid surface in good wetting condition.

3.2.3 Dopant Site Occupation Considerations

Besides the presence of liquid phase, grain growth is also influenced by the charge compensation mechanisms resulting from specific dopant site occupation. The dopants' valence state and their site occupation with influence the oxygen vacancy concentration and thereby the grain boundary mobilities. At room temperature, 0.75PMN-0.25PT crystallizes into a ABO_3 rhombohedral perovskite structure. Pb^{2+} occupies the A site and Mg^{2+}, Nb^{5+}, Ti^{4+} occupy the B site [104]. The rhombohedral structure is considered as a pseudo-cubic structure [105]. In an ideal cubic perovskite, the ionic radii satisfy the relation: $r_A + r_O = \sqrt{2}(r_B + r_O)$ [106]. The Goldschmidt tolerance factor for perovskite structure can be calculated by

$$t = \frac{r_A + r_O}{\sqrt{2}(r_B + r_O)} \tag{17}$$

Using the radii of Pb^{2+}, O^{2-} and weighted average B-site radius for 0.75PMN-0.25PT, the ideal tolerance factor of 0.75PMN-0.25PT is t=0.997. The site occupation behavior cannot solely be determined by the tolerance factor but one should also consider the strain and distribution effects [107, 108]. However, when compare between similar ions, the tolerance factor can help show a useful trend [109]. Here, we define t_A and t_B as the tolerance factors of a perovskite unit cell for a 3 at% cationic substitution on the A and B sites respectively, taking into account the coordination number.

$$t_A = \frac{0.03r + 0.97 \times r_{Pb} + r_O}{\sqrt{2}(r_B + r_O)} \tag{18}$$

$$t_B = \frac{r_A + r_O}{\sqrt{2}(0.97 \times r_B + 0.03r + r_O)} \tag{19}$$

where *r* stands for the radius of the substituting cation. We assumed that the local strain is similar in A and B site. If the incorporation into one site results in a tolerance factor much closer to 1 than the incorporation into the other site, then the dopants prefer to take the first site. Figure 41 shows the tolerance factors t_A and t_B for all lanthanide (Ln^{3+}) ions, which ranges from 0.848 to 1.061 Å for Lu^{3+} and La^{3+}, respectively. The crossover point corresponds to a radius of 1 Å. It is clear that large ions ($r(R_{VI}^{3+}) > 1Å$) prefer to occupy the A site and small ions ($r(R_{VI}^{3+}) < 1Å$) prefer to occupy the B site.

Table 7 Ionic radii of the dopants.

Dopants	**Ionic Radii (*Å*)**	
	$\mathbf{r_{CN\text{-}VI}}$	$\mathbf{r_{CN\text{-}XII}}$
Ba^{2+}	1.360	1.600
Pb^{2+}	1.180	1.490
La^{3+}	1.061	1.320
Gd^{3+}	0.938	1.246
Y^{3+}	0.892	1.220

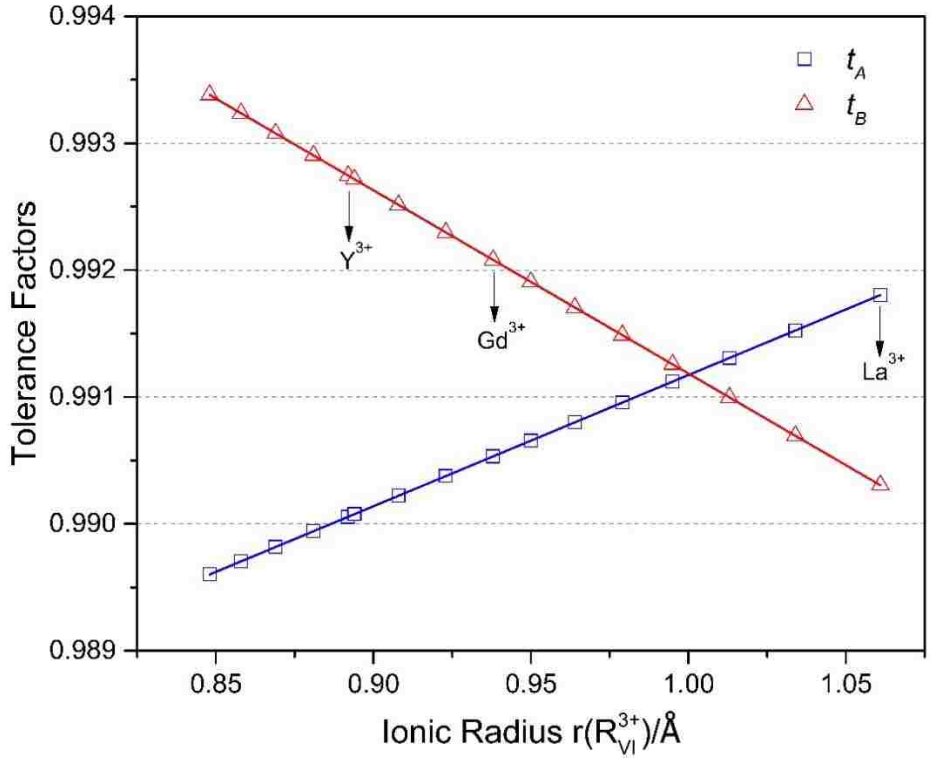

Figure 41. The tolerance factors t_A and t_B as a function of ionic radius.

For these two cases, we consider the following two alternative reactions:

$$M_2O_3 \xrightarrow{4ABO_3} 2M_A^{\bullet} + O_i'' + 2AO \tag{20}$$

$$M_2O_3 \xrightarrow{4ABO_3} 2M_B' + V_O^{\bullet\bullet} + 2BO_2 \tag{21}$$

A stands for Pb^{2+}, *B* stands for the effective $(Mg_{1/4}Nb_{1/2}Ti_{1/4})^{4+}$ site and *M* stands for the dopant ions. For ionic radii $r > 1$ Å, the ion (La^{3+}) prefer to occupy the A-site while Y^{3+} and Gd^{3+} tend to occupy the B-site because of smaller ionic radii. As lanthanum goes into the A-site, pre-existing oxygen vacancies are consumed, which leads to a lower oxygen vacancy

concentration compared to Gd^{3+}-doped and Y^{3+}-doped samples. This lower oxygen vacancy concentration will decrease the diffusion rates and grain-boundary mobilities, as supported by our grain-growth data (Figure 42) and similar work on La-doped PMN-PT [110].

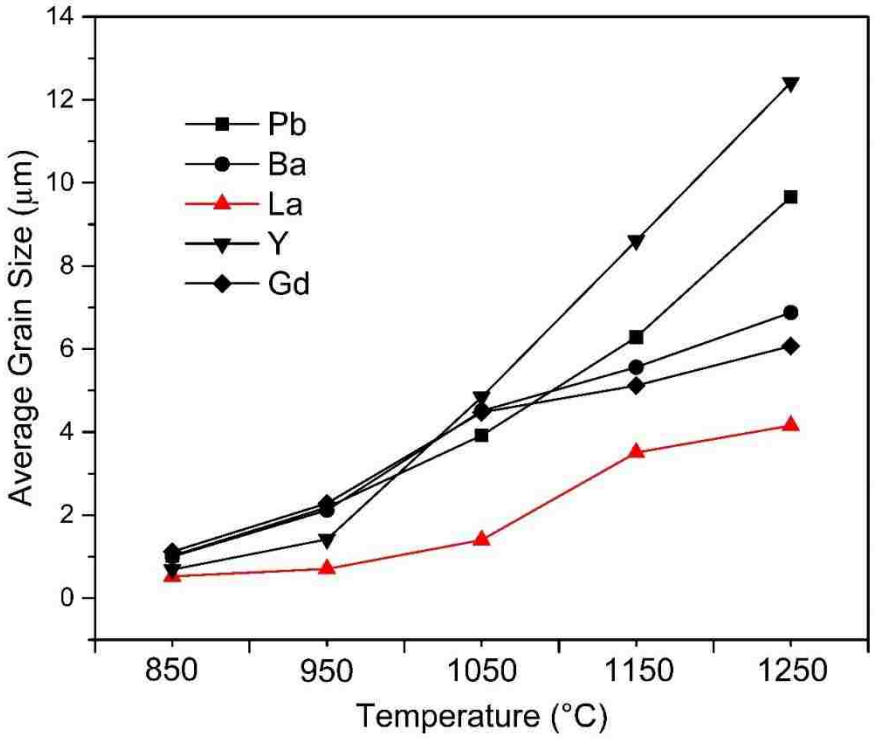

Figure 42. Grain growth of 0.75PMN-0.25PT ceramics with different dopants sintered at different temperatures.

3.3 Conclusion

In this chapter, we showed the phase and microstructure evolution of PMN-PT ceramics with different dopants during sintering. **La-doped PMN-PT samples do not form a liquid phase during sintering which helps the formation of a pure perovskite phase and unimodal rounded**

grains while samples with other dopants exhibit faceted grains. We found that the preferential A-site occupancy of La^{3+} due to its larger ionic radius lowers the oxygen vacancy concentration. As a result, **grain growth of La-doping is suppressed compared to samples doped with the smaller Y^{3+} and Gd^{3+} ions**.

CHAPTER FOUR: SECOND-ORDER NONLINEAR SUSCEPTIBILITY IN PSEUDO-CUBIC PMN-PT

We have selected PMN-PT for our nonlinear optics study and successfully fabricated PMN-PT transparent ceramics. In this chapter, we are going to simulate the second-order nonlinear susceptibility in pseudo-cubic PMN-PT before doing experiment. The variations of the inverse of dielectric tensor $(\varepsilon^{-1})_{ij}$ of a ferroelectric material are given, to a first-order with respect to the external electric field, by:

$$\Delta(\varepsilon^{-1})_{ij} = \sum_k r_{ijk} E_k \tag{22}$$

where r_{ijk} are the electro-optic (EO) tensor coefficients and E_k is the components of electric field. If one assumes the Born-Oppenheimer approximation, the EO tensor can be expressed as a sum of three separate contributions: an electronic, ionic and piezoelectric one. The electronic term is due to the interaction of the electric field with valence electrons. This term can be linked to the nonlinear susceptibility since $\chi^{(2)}_{ijk}$ represents the second-order term in the expansion of the induced polarization with respect to the field, i.e. the first-order change of the linear dielectric susceptibility $\Delta\varepsilon_{ij}$. Hence, using the fact that $(\varepsilon^{-1})_{ik}\varepsilon_{kj}=\delta_{ij}$ and expressing the variation of the inverse of the permittivity tensor:

$$\Delta(\varepsilon^{-1})_{ij} = -\sum_{k,l}(\varepsilon^{-1})_{ik}\Delta\varepsilon_{kl}(\varepsilon^{-1})_{lj} \tag{23}$$

we have:

$$r^{el}_{ijk} = -2\sum_{m,l}(\varepsilon^{-1})_{im}\chi^{(2)}_{mlk}(\varepsilon^{-1})_{lj} \tag{24}$$

which, in the frame of the principal axes of the crystal, becomes:

$$\chi_{ijk}^{(2)} = -\frac{1}{2} n_i^2 n_j^2 r_{ijk}^{el} \tag{25}$$

Here, n_i are the refractive indices along the principal axes. This relationship shows that, at least in part, the SHG nonlinear susceptibility of a ferroelectric material is related to its high-frequency EO coefficients (UV-VIS-NIR). However, in most ferroelectrics, the main contribution to r_{ijk} comes from a lower-frequency ionic component (far infrared). This term comes from the relaxation of the atomic positions due to the applied electric field E_k and the variations of the dielectric tensor coefficients ε_{ij}. It is usually expressed as a contribution of all transverse optic modes *m* at **q**=**0**:

$$r_{ijk}^{ion} = -\frac{1}{\sqrt{V}} \frac{1}{n_i^2 n_j^2} \sum_{\mathrm{m}} \frac{\alpha_{ij}^{m} \mathrm{p_{mk}}}{\omega_m^2} \tag{26}$$

where V is the volume of the unit cell, α^m is the Raman susceptibility of mode *m*, and p_{mk} the dipole moment induced by mode *m*:

$$\mathrm{p_{mk}} = \sum_{\mathrm{k'}} Z_h^* u_m(k', h) \tag{27}$$

Here, Z^* and u_m indicate the effective charge and the atomic displacement of atom h, respectively.

The piezoelectric contribution, due to the relaxation of the unit cell dimensions, can be expressed as:

$$\mathrm{r}_{ijk}^{piezo} = \sum_{\mathrm{m,l}} \pi_{ijml} d_{kml} \tag{28}$$

where π_{ijml} are the elasto-optic coefficients and d_{kml} are the piezoelectric strain coefficients. Naturally, this contribution depends on the state of stress of the ferroelectric crystal - a condition that would need proper averaging (Reuss, Voigt, Hill) in a polycrystalline ceramic- but it is assumed that such unit cell relaxation is negligible at optical frequencies.

To further characterize the potential nonlinear SHG response of PMN-PT in relation to its ferroelectricity, we have used the Laudau-Devonshire expansion of the volumic free-energy. Following Ishibashi and Orihara [111] and using Landau-Khalatnikov (LK) equations to describe the nonlinear dynamics of charges and its effect on the dielectric response, we have expressed the NLO coefficients for the low-symmetry (rhombohedral ferroelectric FE). Naturally, all $\chi^{(2)}$ processes vanish in the paraelectric (PE) high-symmetry (cubic) phase because of inversion symmetry [112] and only third-order NL susceptibility coefficients remain above T_c. However, $\chi^{(2)}$-processes are non-zero in the FE phase because a spontaneous polarization P_0 breaks the inversion symmetry.

Our starting point is the expression of the free energy per unit volume in terms of the polarization components:

$$\mathrm{F} = \frac{\alpha}{2\varepsilon_0}\mathrm{P_i P_i} + \frac{\beta_1}{4\varepsilon_0^2}(\mathrm{P_i P_i})^2 + \frac{\beta_2}{2\varepsilon_0{}^3}\left(\mathrm{P_x^2 P_y^2} + \mathrm{P_y^2 P_z^2} + \mathrm{P_z^2 P_x^2}\right) + \cdots \qquad (29)$$

where the polarizability is $\alpha = \mathrm{a}(T - T_0)$ in which, for a second-order phase transition, $T_0 = T_C$. When bulk FE material is exposed to a high intensity incident IR radiation, we should add an electric field term to the free energy, $\mathrm{F_E} = \mathrm{F} - \mathbf{E}\cdot\mathbf{P}$, where **E** is the electric field come from the incident IR radiation. The LK equation for the polarization vector **P** is:

$$\widehat{O}P_i = -\frac{\partial F}{\partial P_i} + E_i \tag{30}$$

In the PE phase, we have **P**=0. Using the Taylor series expansion:

$$P_i = P_i^{(1)} + P_i^{(2)} + P_i^{(3)} = \varepsilon_0 \chi_{il}^{(1)} E_l + \varepsilon_0 \chi_{ilm}^{(2)} E_l E_m + \varepsilon_0 \chi_{ilmn}^{(3)} E_l E_m E_n \tag{31}$$

We can write the NLO coefficients by comparing to the Taylor expansion of f_i(**P**):

$$f_i(P) = f_{il}(0)P_l + \frac{1}{2} f_{ilm}(0)P_l P_m + \frac{1}{6} f_{ilmn}(0)P_l P_m P_n \tag{32}$$

According to the equations above, we can get a general form for $\chi^{(2)}$:

$$\chi_{ilm}^{(2)}(-(\omega_1 + \omega_2); \omega_1, \omega_2) = \frac{\varepsilon_0^2}{2} f_{ilm}^0 \chi_i(\omega_1 + \omega_2) \times \chi_l(\omega_1)\chi_m(\omega_2) \tag{33}$$

For rhombohedral symmetry, all non-vanishing, nonlinear-susceptibility tensor elements are given by Table 8.

Table 8 Non-vanishing second-order NLO tensor elements for the rhombohedral ferroelectric phase [113].

Process, K	Susceptibility, $\chi^{(2)}_{ilm}$
Second-harmonic generation $K = 1/2$ $\chi^{(2)}_{ilm}(-2\omega;\omega,\omega)$ Symmetric on exchange of (l,m)	$\chi^{(2)}_{zzz} = \chi^{(2)}_{xxx} = \chi^{(2)}_{yyy} = \chi^{\mathrm{SHG}}_1 = \dfrac{\epsilon_0[(\hat{O}_2 - q)(vs^2 + 2uh_1) + 2q(v\sigma^2 + uh_2)]}{8(\hat{O}_2 + q)(\hat{O}_2 - 2q)}$
	$\chi^{(2)}_{xxy} = \chi^{(2)}_{xxz} = \chi^{(2)}_{yyz} = \chi^{(2)}_{yyz} = \chi^{(2)}_{zzx} = \chi^{(2)}_{zzy} = \chi^{\mathrm{SHG}}_3 = \dfrac{\epsilon_0[\hat{O}_2(2vs\sigma + 2uh_2) + q(2v\sigma^2 + 2uh_3)]}{8(\hat{O}_2 + q)(\hat{O}_2 - 2q)}$
	$\chi^{(2)}_{xyy} = \chi^{(2)}_{xzz} = \chi^{(2)}_{yxx} = \chi^{(2)}_{yzz} = \chi^{(2)}_{zxx} = \chi^{(2)}_{zyy} = \chi^{\mathrm{SHG}}_2 = \dfrac{\epsilon_0[\hat{O}_2(v\sigma^2 + uh_2) + q(vs^2 + 2uh_1)]}{8(\hat{O}_2 + q)(\hat{O}_2 - 2q)}$
Optical rectification $K = 1/2$ $\chi^{(2)}_{ilm}(0;-\omega,\omega)$	$\chi^{(2)}_{zzz} = \chi^{(2)}_{xxz} = \chi^{(2)}_{yyz} = \chi^{\mathrm{OR}}_1 = \dfrac{\epsilon_0[(p+q)(v\lvert s\rvert^2 - 2ug_1) - 2q(v\lvert\sigma\rvert^2 + ug_2)]}{8(q-p)(p+2q)}$
	$\chi^{(2)}_{xxy} = \chi^{(2)}_{xxz} = \chi^{(2)}_{yyx} = \chi^{(2)}_{yyz} = \chi^{(2)}_{zzx} = \chi^{(2)}_{zzy} = \chi^{\mathrm{OR}}_3$ $= \dfrac{\epsilon_0[(p+q)(vs\sigma^* + ug_2) - q(vs^*\sigma + ug_2 + v\lvert\sigma\rvert^2 + 2ug_1)]}{8(q-p)(p+2q)}$
	$\chi^{(2)}_{xyx} = \chi^{(2)}_{xzx} = \chi^{(2)}_{yxy} = \chi^{(2)}_{yzy} = \chi^{(2)}_{zxz} = \chi^{(2)}_{zyz} = \chi^{\mathrm{OR}}_4$ $= \dfrac{\epsilon_0[(p+q)(vs^*\sigma + ug_2) - q(vs\sigma^* + ug_2 + v\lvert\sigma\rvert^2 + 2ug_1)]}{8(q-p)(p+2q)}$
	$\chi^{(2)}_{xyy} = \chi^{(2)}_{xzz} = \chi^{(2)}_{yxx} = \chi^{(2)}_{yzz} = \chi^{(2)}_{zxx} = \chi^{(2)}_{zyy} = \chi^{\mathrm{OR}}_2 = \dfrac{\epsilon_0[p(v\lvert\sigma\rvert^2 + ug_2) - q(v\lvert s\rvert^2 + 2ug_1)]}{8(q-p)(p+2q)}$

Table 8 makes use of the following notations:

$$\hat{O}_n = \Theta(n\omega) - p \tag{34}$$

$$\Theta(\omega) = \frac{-i\gamma\omega - m\omega^2}{Ne^2} \tag{35}$$

$$p = \frac{\alpha}{\varepsilon_0} + \frac{P_0^2}{\varepsilon_0^2}(3\beta_1 + 2\beta_2) \tag{36}$$

$$q = \frac{2\beta_2}{\varepsilon_0^2} P_0^2 \tag{37}$$

$$u = \frac{2\beta_2}{\varepsilon_0^2} P_0 \tag{38}$$

$$v = \frac{6\beta_1}{\varepsilon_0^2} P_0 \tag{39}$$

$$P_0 = \sqrt{\frac{-\varepsilon_0 \alpha}{\beta_1 + 2\beta_2}} \tag{40}$$

$$\sigma(\omega) = \frac{q}{\varepsilon_0[\hat{O}_1(\hat{O}_1 - q) - 2q^2]} \tag{41}$$

$$s(\omega) = \frac{(\hat{O}_1 - q)}{\varepsilon_0[\hat{O}_1(\hat{O}_1 - q) - 2q^2]} \tag{42}$$

$$h_1 = \sigma^2 + 2s\sigma;\ h_2 = s^2 + 3\sigma^2 + 2s\sigma;\ h_3 = \sigma^2 + 4s\sigma \tag{43}$$

Here the only material-derived parameters are the temperature-dependent polarizability, α, the nonlinear polarizability coefficients β_1, and β_2, the concentration of dipoles, N (dependent on the known crystal structure), their reduced mass, m and their relaxation coefficient, γ. We must stress that the use of this particular formalism and LK operator expression for $\Theta(\omega)$ is meant to describe the behavior of non-relaxor type ferroelectric materials (such as $PbTiO_3$) but may be somewhat approximate in the case of PMN-PT. Nevertheless, we can hope to estimate, at least semi-quantitatively, the magnitude of the complex-valued $\chi^{(2)}$ coefficients of the rhombohedral FE phase of PMN-PT as a function of frequency (from $\omega=0$ to the soft-mode frequency $\omega=\omega_0$, with $\omega_0{}^2 = Ne^2 \frac{aT_0}{\varepsilon_0 m}$) and as a function of temperature (from T=0 to $T=T_C$). Using a Curie temperature of T_c=155°C for 0.75PMN-0.25PT and parameters estimated from [114], we obtained the results shown in Figures 43-45.

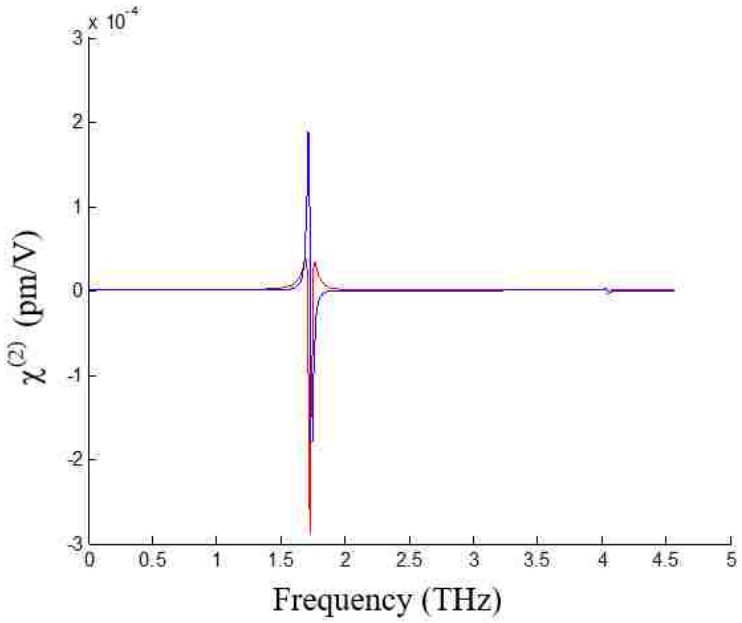

Figure 43. SHG nonlinear susceptibility coefficient $\chi^{(2)}_{xxy}(-2\omega;\omega,\omega)$ versus frequency at T=50°C. (Real part is in red and imaginary part in blue).

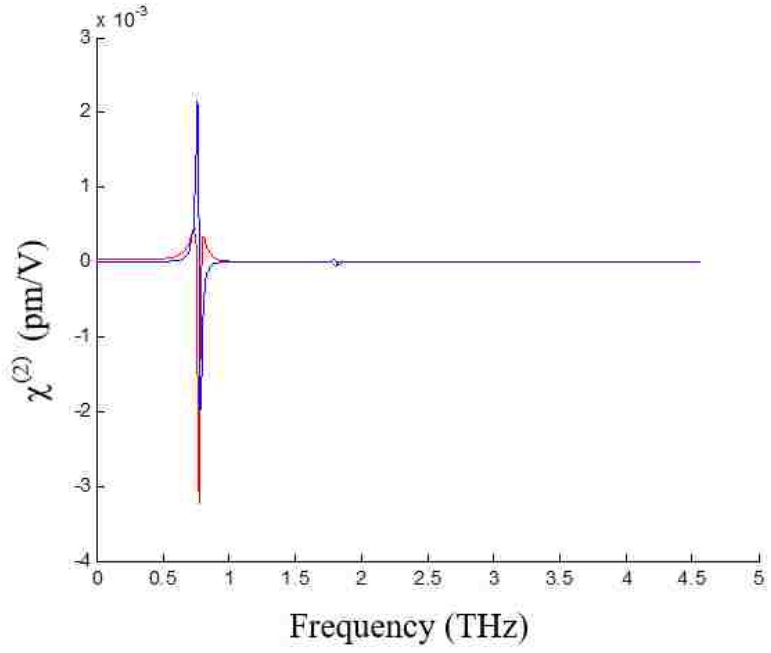

Figure 44. SHG nonlinear susceptibility coefficient $\chi^{(2)}_{xxy}(-2\omega;\omega,\omega)$ versus frequency at T=134°C. (Real part is in red and imaginary part in blue).

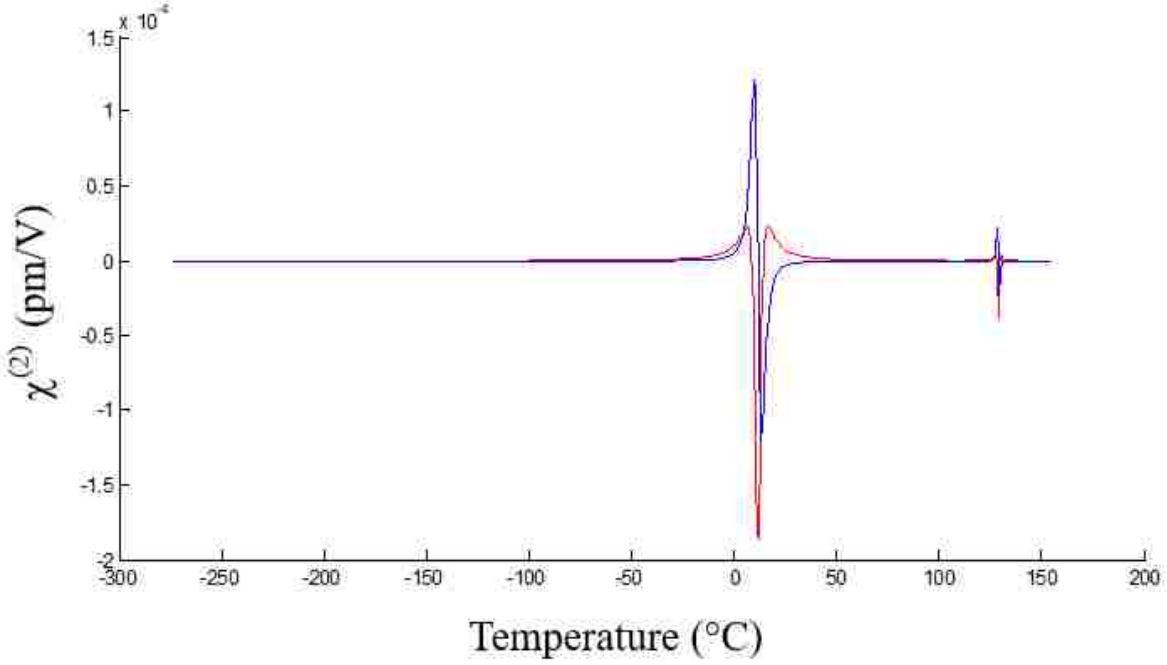

Figure 45. Effect of temperature on the SHG nonlinear susceptibility coefficient $\chi^{(2)}_{xxy}(-2\omega;\omega,\omega)$ at a frequency of 2 THz. (Real part is in red and imaginary part in blue).

From the simulation result, we found the second-order nonlinear susceptibility in this material is maximized in the Terahertz range. After comparing the $\chi^{(2)}$ value with other common nonlinear materials [115], we found the second-order susceptibility of PMN-PT is very small (Table 9). One explanation is that rhombohedral PMN-PT is too close to the cubic structure ($\alpha \approx \beta \approx \gamma \approx 89°56'$), which does not provide enough departure from centrosymmetry.

Table 9 Second-order susceptibility value for well-known nonlinear crystals.

Nonlinear Crystal	**$\chi^{(2)}$ (pm/V)**	**Frequency (THz)**
$LiNbO_3$	152.4	2
GaAs	46.1	2
GaP	21.7	2
PMN-PT	2×10^{-4}	1.7

CHAPTER FIVE: NON-STOICHIOMETRIC GRAIN-GROWTH IN ZnSe CERAMICS FOR $\chi^{(2)}$ INTERACTION

As we discussed in Chapter one, despite the lack of long range order, ZnSe ceramics can serve as efficient nonlinear frequency converters by way of the (rQPM) process. The commercially available low-loss (bulk absorption coefficient at 10.6 μm is less than 0.0005 cm^{-1}) polycrystalline ZnSe infrared optics was produced by chemical vapor deposition (CVD). Chemical vapor deposition (CVD) is a widely used material-processing technology [116-118]. The schematic of a ZnS CVD system, similar to the one use for ZnSe synthesis, is shown in Figure 46. The ZnSe CVD process involves the reaction of zinc vapor with hydrogen selenide gas in a higher-temperature deposition zone according to:

$$Zn(g) + H_2Se(g) \overset{Ar}{\Rightarrow} ZnSe(s) + H_2(g) \quad (44)$$

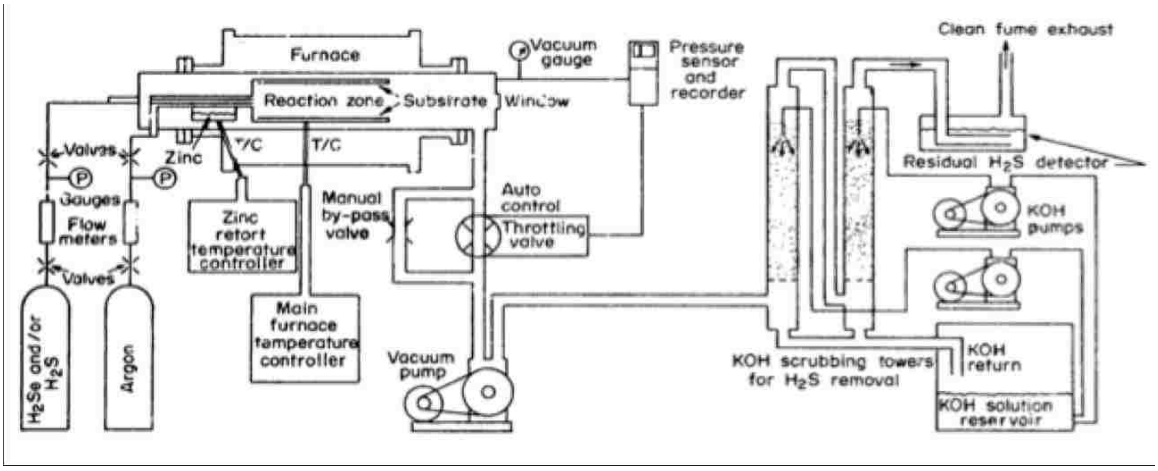

Figure 46. Schematic of a ZnS CVD system [119].

CVDed ZnSe is used in a broad range of applications, including optical components for high resolution Forward Looking Infrared (FLIR) thermal imaging equipment. Its low losses and

high resistance to thermal shock have made this material unique to high power CO_2 laser system. Figure 47 is the transmission of commercial CVDed ZnSe. The typical grain-size of commercial CVDed ZnSe is in the range of 50-70 µm.

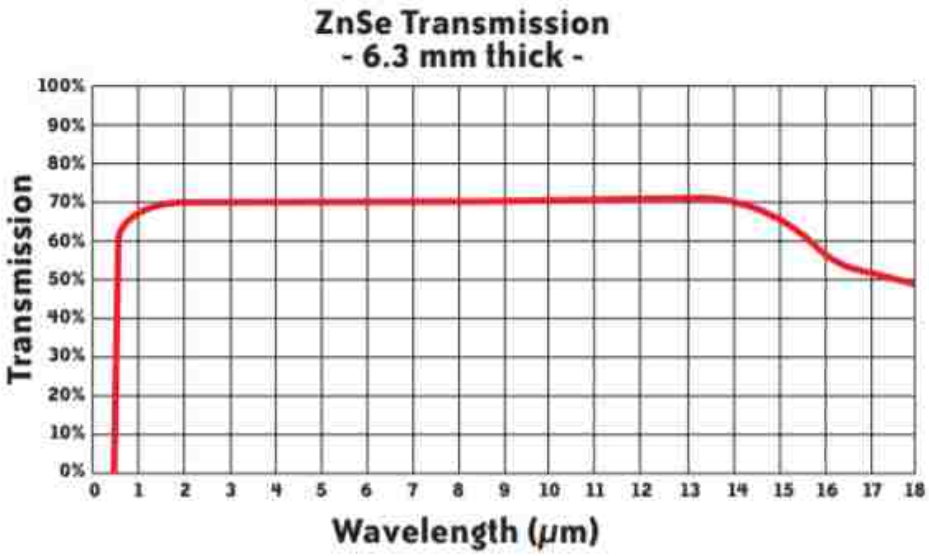

Figure 47. Transmission of commercial CVD Zinc Selenide (II-VI corp.) [120].

This chapter investigates heat-treatment conditions necessary to develop adequate microstructures for rQPM in CVD-grown ZnSe ceramics. Non-stoichiometric grain growth of CVD-grown ceramics limits contamination from impurities compared to melt- or solution-grown crystals and hot-pressed ceramics. It also prevents the formation of scattering centers due to stress-induced birefringence and the presence of hexagonal ZnSe when carried out below the sphalerite-wurtzite transition temperature at 1425°C. It also improves grain growth kinetics because the off stoichiometry will form Schottky or Frenkel point-defects and then increase the vacancy concentration, which promote the grain boundary mobility and grain growth speed. This study builds upon the previous work by Terashima *et al.* [121-123] and Triboulet *et al.* [124-128] in

which heat-treatments were performed on CVD-grown ZnSe for the production of single-crystals. Here, the effects of the heat-treatment atmosphere [129] on the average grain-size and grain-size distribution are more specifically investigated and the experimentally-determined grain-size distributions are used to predict the rQPM efficiency of second-harmonic (SH) generation in this material[3].

5.1 Experimental Procedure

Polycrystalline coupons of CVD-grown ZnSe (II-VI Inc., USA) with an average grain size of 75 μm were used as the starting material. Cubic samples measuring 5x5x5 mm^3 were diced from these coupons and all faces were mechanically polished so that grain-growth would not be suppressed [130]. Samples were annealed at 850 or 1000°C for 6 to 168 h in a vacuum, or in a saturated vapor pressure of zinc or selenium vapor. These vapors were produced by either placing fine zinc shots (Atomergic Chemetals Corp.) or selenium granules (United Mineral & Chemical Corp.) in a small boat next to the sample before sealing the quartz ampoule in which the treatment was performed. Ampoules were sealed off at a pressure of $3.4x10^{-6}$ atm. The microstructure of polished ZnSe was inspected by polarized optical microscopy after a 15 min chemical etch in a 30 mol% NaOH solution held at 95°C. The grain-size was determined by the line intercept method using the Image J software (National Institutes of Health). Grain-size distributions were obtained using a minimum of 1000 grains. Laser scattering tomography was used to check the precipitate

[3] This work has been submitted to Chen, X. and Gaume, R.. Non-Stoichiometric grain-growth in ZnSe ceramics for $\chi^{(2)}$ interaction. *Optical Materials Express*, 2018.

after solid-state grain-coarsening [131-133]. Optical transmission was measured using an ultraviolet–visible–near infrared (UV–VIS–NIR) spectrometer (Cary 500, Varian Inc., CA, USA) and the mid-infrared transmission spectra were acquired on a FT-IR spectrophotometer (Nicolet 6700，Thermo Scientific).

Figure 48. Quartz ampoule used in the experiment.

5.2 Results and Discussion

5.2.1 Starting Materials Characterization

These samples have 70% transmittance in the range 1.5 μm to 14 μm, which is in compliance with the transmittance data provided by the vendor (Figure 49). The X-ray diffraction pattern shows that the crystal structure of ZnSe is cubic zincblende and that no significant texture is present (Figure 50).

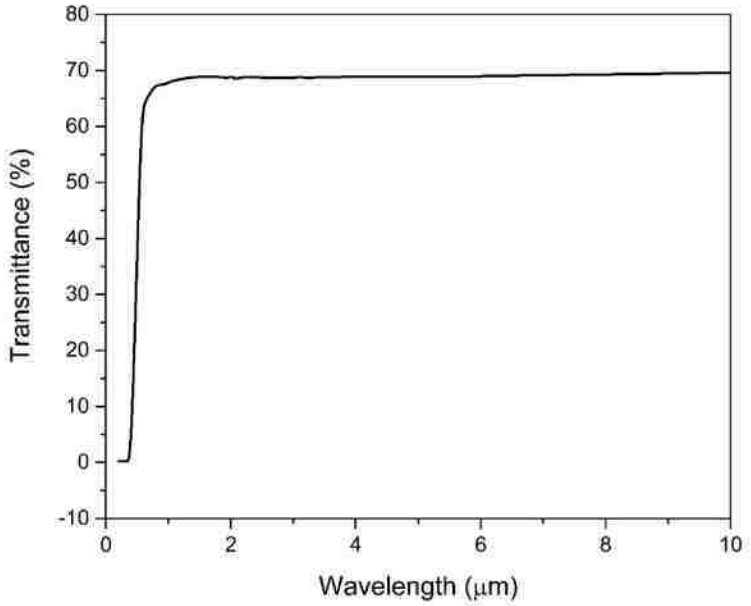

Figure 49. Transmittance spectra of starting CVD polycrystalline ZnSe.

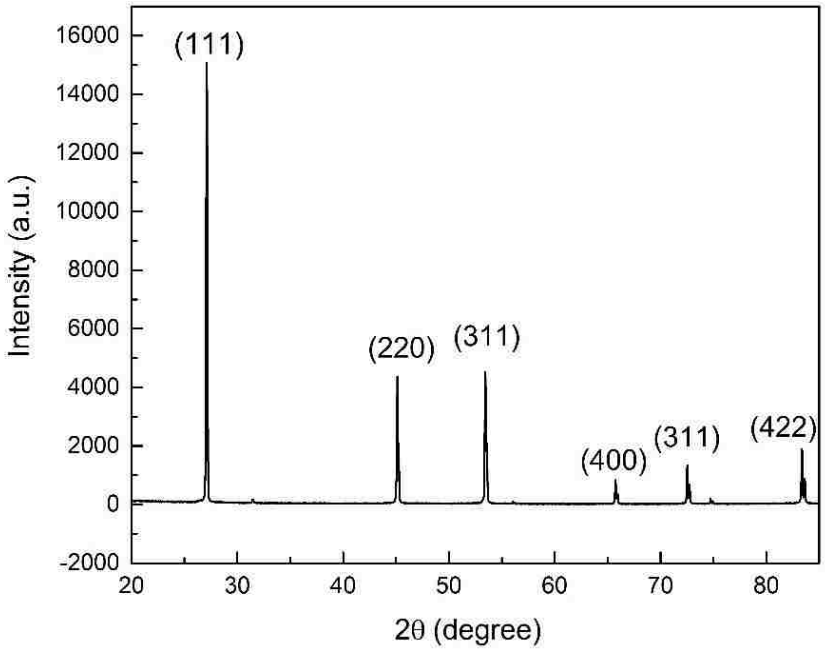

Figure 50. X-ray diffraction of purchased ZnSe.

5.2.2 Grain-Coarsening Kinetics in CVD-grown ZnSe

Figure 51 shows the microstructures of ZnSe ceramics obtained before and after annealing under vacuum, Zn and Se vapors. As noticed previously [121, 128], annealing in selenium vapor leads to the development of a coarser microstructure than in zinc vapor or vacuum. Twining is present in all cases, even in the starting material. There is no significant difference in the amount of twins before and after grain-coarsening.

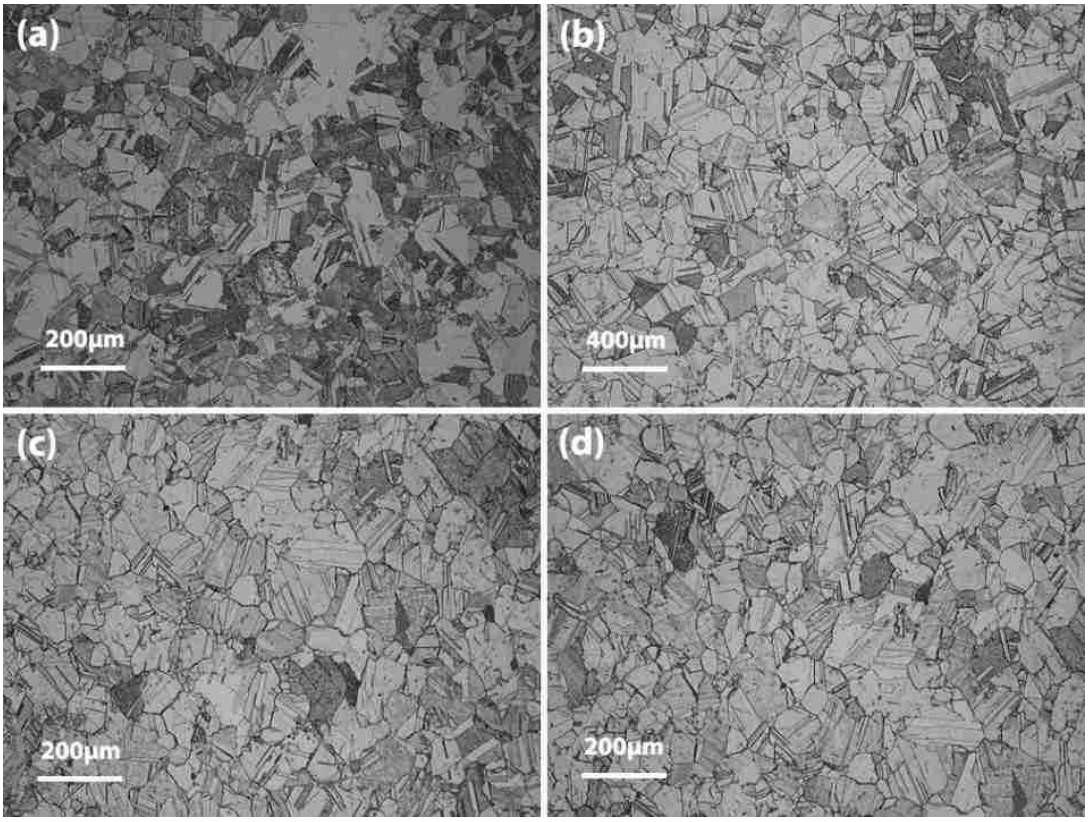

Figure 51. Sample microstructures: (a) before annealing, (b) after annealing in Se vapor at 850°C for 168 h, (c) after annealing in Zn vapor at 850°C for 168 h, (d) after annealing in vacuum at 850°C for 168 h. Note the change of scale for figure (b).

The average grain-size as a function of the annealing time for the different temperature and atmosphere conditions is represented in Figure 52. The error bars represent the 95% confidence interval for the population mean, calculated according to:

$$\bar{x} \pm t(\alpha, N-1) * \frac{s_x}{\sqrt{N}} \tag{45}$$

where $\bar{x}$ is the mean value and s_x is the standard deviation of the sampled data set. With a grain population N=1000, the significance level is α=(1-0.95)/2. The grain-growth kinetics is expected to follow a typical grain-growth model [134]:

$$d^m(t) - d^m(0) = k \cdot t \tag{46}$$

where $d(t)$ is the average grain-size at time t, k a temperature-dependent factor and m the grain-growth exponent, with a value between 2 and 4, typically. The fit to Eq. 46 yields m=3 for a heat-treatment in Se vapor at 850°C, and m=6 in the cases of Zn vapor or vacuum at the same temperature. In addition, it was found that the grain-growth exponent in Se atmosphere remained constant at 1000°C. After 168 h, crystallites as large as 1.5 mm can be obtained at 1000°C in selenium vapor. Vapor transport equilibration affects the sample stoichiometry thereby affecting the diffusion rate of species and the mobility of grain-boundaries. Large grain-growth exponent in vacuum and zinc vapor atmosphere suggest the presence of low-solubility precipitates that pin the grain-boundaries. This fact is supported by the high density of scattering centers revealed by laser scattering tomography in those latter samples (Figure 53). Figure 54 shows the experimental determined phase diagram of ZnSe. Focus on the red square data, we can see that the solid-solubility of Zn (~10^{-5} mol of Zn per mole of ZnSe) is ten times lower than that of Se (~10^{-4} mol

of Zn per mole of ZnSe) in zincblende ZnSe at 850°C [135]. Based on the data from Figure 51(b), one can calculate the activation energy for grain-growth using:

$$k = k_0 \exp(-\frac{E_a}{RT}) \tag{47}$$

where k_0 is the pre-exponential constant of the diffusion coefficient, E_a is the activation energy for grain-growth, T is the absolute temperature and R is the perfect gas constant. Using the grain-size data over the temperature range, an Arrhenius plot of Figure 55 shows a mean activation energy value of $\overline{E_a}$=19.7 kJ/mol, similar to that reported by Triboulet *et al.* [128]. The coefficient of variation (CV) for the activation energy, defined as the standard deviation divided by the mean, is 7%, showing consistency within this data set. As the annealing time increases, the offset of the Arrhenius plot, ln(k_0), progressively converges towards a single value suggesting that diffusion-driven grain-boundary mobility reaches an equilibrium across the entire sample size for long annealing times.

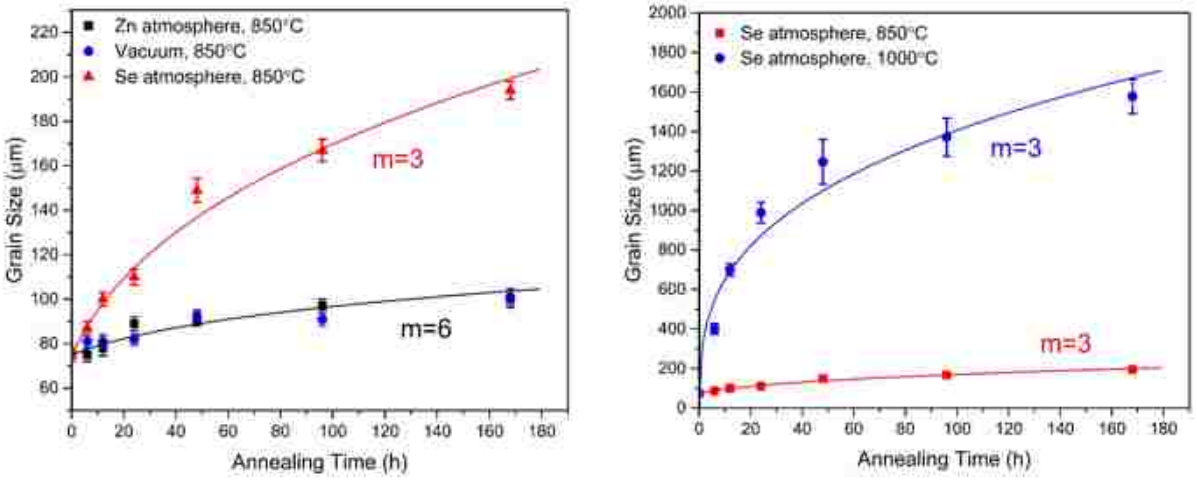

Figure 52. Grain-size as a function of annealing time (a) at 850°C in different atmospheres and (b) at 850°C and 1000°C in Se atmosphere. d_0= 75 µm.

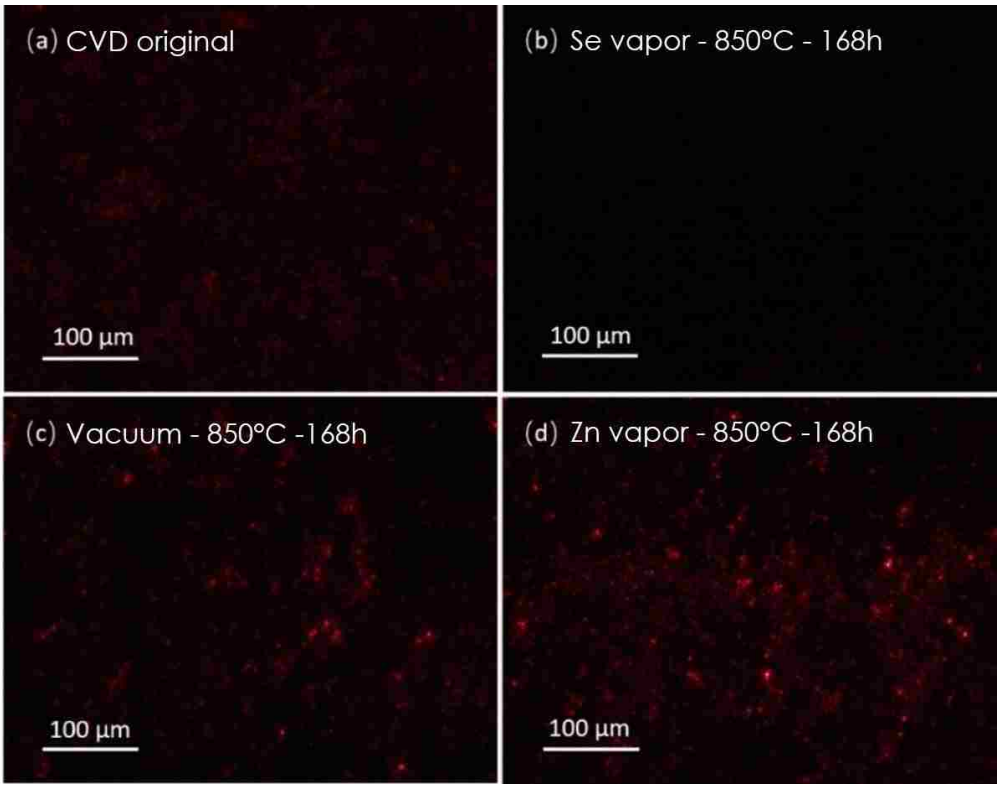

Figure 53. Laser scattering tomography images of (a) original CVD-grown ZnSe ceramic and ZnSe ceramic samples annealed at 850°C for 168 h (b) in selenium; (c) in vacuum and (d) in zinc vapor.

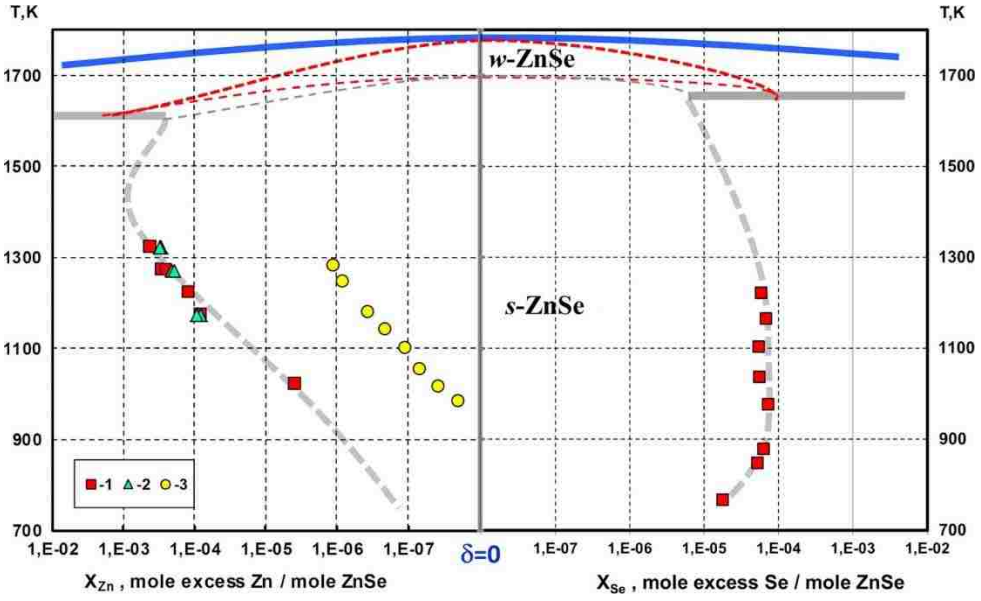

Figure 54. ZnSe homogeneity region [135].

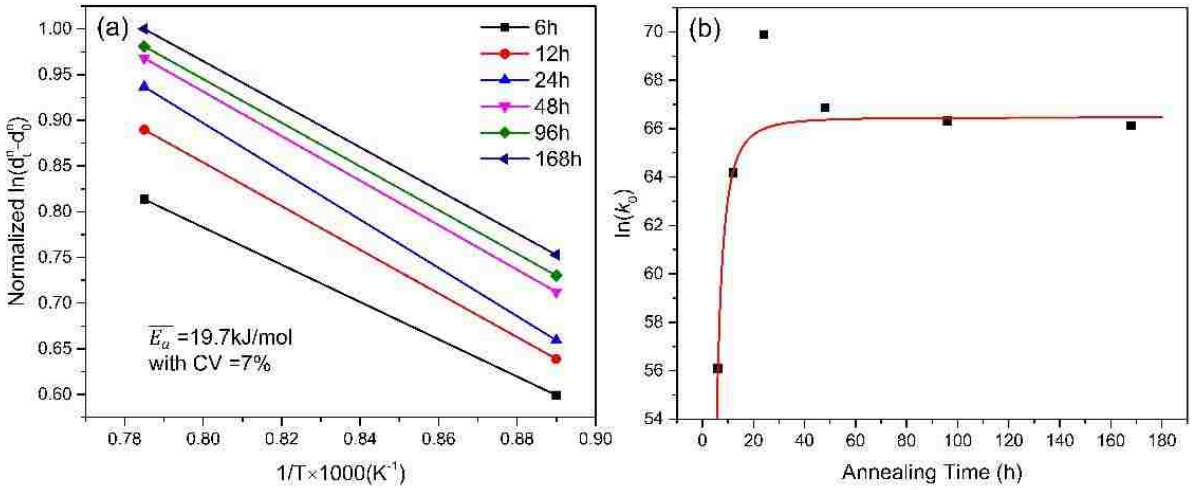

Figure 55. Arrhenius plot for ZnSe grain-growth kinetics and (b) ln(k_0) as a function of annealing time in Se vapor.

To analyze the effect of heat-treatment conditions on the grain-size distribution, we performed a comparison between heat-treated samples with the same average grain-size. This average grain-size was chosen to be 100 µm, *i.e.* a size optimized for MWIR random quasi-phase matched second harmonic generation at an incident wavelength of 4.7 µm and SH at 2.35 µm. In selenium atmosphere, 100 µm average grain-size is obtained after annealing at 850°C for 12 h. Conversely, a 168 h-long heat-treatment is necessary under vacuum or zinc atmosphere at the same temperature. Grain-size histograms (Figure 56) were built using Freedman-Diaconis rule to determine the binning size for a data set of N=1000 grains, according to:

$$bin\ size = 2 * \frac{IRQ}{\sqrt[3]{N}} \tag{48}$$

where IRQ is the interquartile range of the data. These size histograms can be fitted to a lognormal distribution [136]:

$$f(d) = \frac{1}{\beta d\sqrt{2\pi}} * \exp(-\frac{(\ln d - \alpha)^2}{2\beta^2}) \quad (49)$$

where *d* is the lognormally-distributed grain size. α and β are the mean and standard deviation of the logarithm of the grain size, respectively. The mean μ and standard deviation σ of the grain-size are respectively defined by:

$$\mu = \exp(\alpha + \frac{\beta^2}{2}) \quad (50)$$

$$\sigma^2 = \exp(2\alpha + \beta^2)\,[\exp(\beta^2) - 1] \quad (51)$$

Figure 56 shows that, regardless of the stoichiometry shift, the size-distribution remains lognormal with a similar standard deviation value. Therefore, the excess of selenium only favors a faster grain-growth compared to stoichiometric and zinc-rich ZnSe.

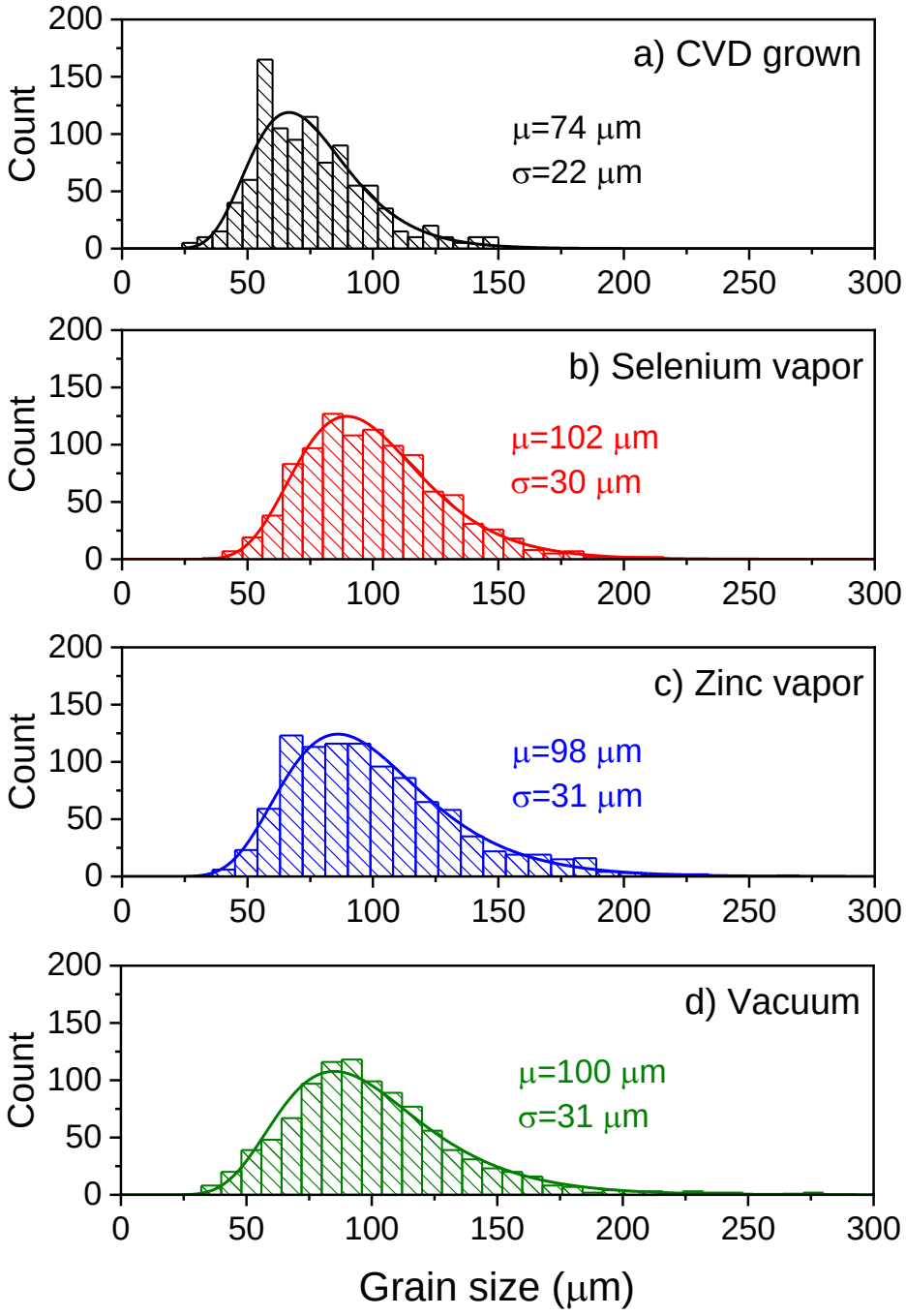

Figure 56. Grain-size distributions of a) original CVD-grown ZnSe ceramics; and of annealed ceramics with comparable average grain-sizes (100 μm) after treatment at 850°C under b) Se vapor for 12 h, c) Zn vapor for 168 h and d) vacuum for 168 h. The mean grain-size value and its standard deviation are indicated for each fit.

It is worth noting that the off-stoichiometry defects introduced by the heat-treatment in the presence of selenium deteriorate the transmittance of the samples in the near-infrared (Figure 57). However, the color centers can be removed by a subsequent post-treatment at 700°C for 2 h in a vacuum. This short heat-treatment does not affect the average grain-size nor its distribution, and restores the transmittance to the level of the original CVD material.

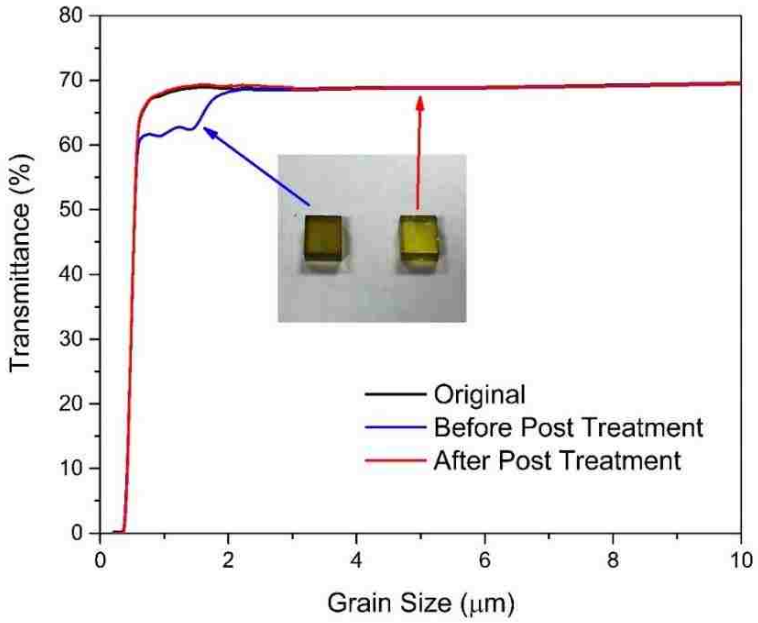

Figure 57. Transmittance spectra of the starting CVD polycrystalline ZnSe, a 12h-annealed sample in selenium vapor and of a 12h-annealed sample in selenium vapor further treated at 700°C for 2 h in a vacuum..

5.2.3 Effect of Grain-Size Distribution on SHG Efficiency

Random quasi-phase-matched second harmonic generation can be simply modeled using a one-dimensional (1D) layered structure along which light propagates and composed of grains with

random crystalline orientations and thicknesses (Figure 58). The refractive index and dispersion are assumed to be the same for all grains. One can show that, within the r^{th} grain, the electric field amplitude at frequency 2ω generated by the fundamental field is [47]:

$$E_{2\omega,r} = -\frac{\omega\chi_r^{(2)}}{n_{2\omega}c\Delta k}{E_\omega}^2 \int_{Z_{r-1}}^{Z_r} e^{i\Delta kz}dz = -\frac{\omega\chi_r^{(2)}}{n_{2\omega}c\Delta k}{E_\omega}^2(e^{i\Delta kX_r}-1)e^{i\Delta k\sum_{j=1}^{r-1}X_j} \quad (52)$$

where c is the speed of light, $n_{2\omega}$ the refractive index at angular frequency 2ω, E_ω the electric field at the fundamental frequency, $\Delta k = k_{2\omega} - 2k_\omega$ the phase mismatch, X_r the size of the r^{th} grain and $\chi_r^{(2)}$ the effective nonlinear optical coefficient of grain r given its particular orientation.

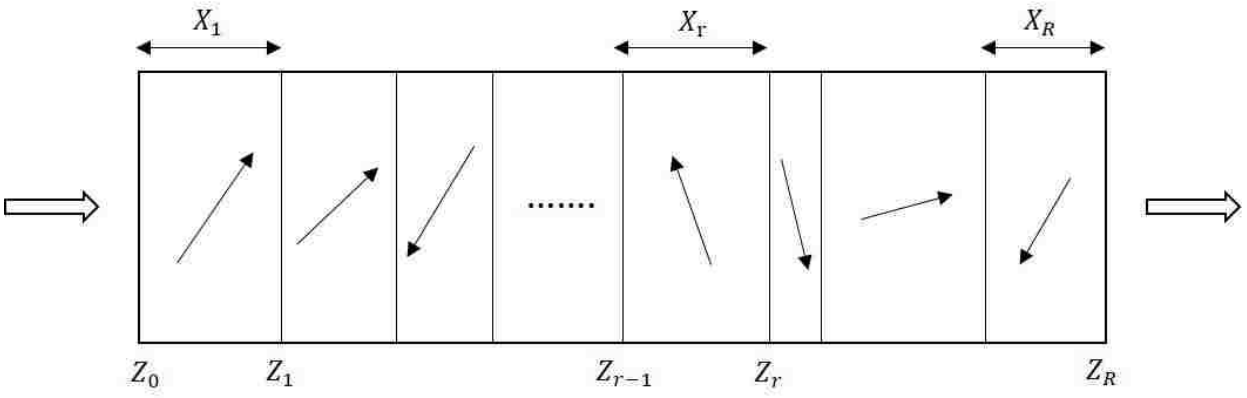

Figure 58. Random quasi-phase-matching in a polycrystalline medium. Each block represents a crystallite with random thickness and crystallographic orientation. Light propagates through the thickness of this one-dimensional layered structure.

The random orientation of the grains means that the normalized component of the nonlinear polarization in the direction of the incident electric field ranges from 1 to -1. In order to numerically implement this, we used a random number generation algorithm so that $\chi_r^{(2)} = \cos(\pi y_r)\,\chi^{(2)}$ by

sampling y_r uniformly in the interval [0, 1] [137]. After propagation through R crystallites, the amplitude of the electric field at 2ω can be deduced from Equation 52:

$$E_{2\omega} = -\frac{\omega\chi^{(2)}}{n_{2\omega}c\Delta k}E^2(\omega)\left(\sum_{p=1}^{R}\cos(\pi y_p)\right)\left(e^{i\Delta k X_p}-1\right)e^{i\Delta k\sum_{j=1}^{p-1}X_j}) \quad (53)$$

and the relative conversion efficiency is:

$$\frac{I_{2\omega}}{I_\omega} = \frac{n_{2\omega}|E_{2\omega}|^2}{n_\omega|E_\omega|^2} = \frac{\omega^2(\chi^{(2)}E_\omega)^2}{n_\omega n_{2\omega}c^2\Delta k^2}\left(\sum_{p=1}^{R}\cos(\pi y_p)(e^{i\Delta k X_p}-1)\,e^{i\Delta k\sum_{j=1}^{p-1}X_j}\right)^2 \quad (54)$$

For a given average grain-size, the effect of size-distribution on the conversion efficiency can be best analyzed through a Monte Carlo simulation [47]. Figure 59 shows the simulation results for a SHG process in polycrystalline ZnSe pumped at 4.7 μm wavelength at which the coherence length is 100 μm. In this figure, three cases are compared: (i) an ideal sample with a monodisperse grain-size of 100 μm, (ii) a sample having undergone grain-growth in selenium vapor with a size-distribution given by Fig. 56b (μ=102 μm and σ=30 μm) and (iii) the original CVD-grown ZnSe with 75 μm average grain-size (Fig. 56a). As expected, the conversion efficiency scales linearly with the number of grains, and the narrow grain-size distribution yields a higher conversion efficiency. The conversion efficiency of a selenium-treated sample reaches 83% of that of an ideal monodisperse microstructure and performs 62% better than an untreated CVD-grown ceramic.

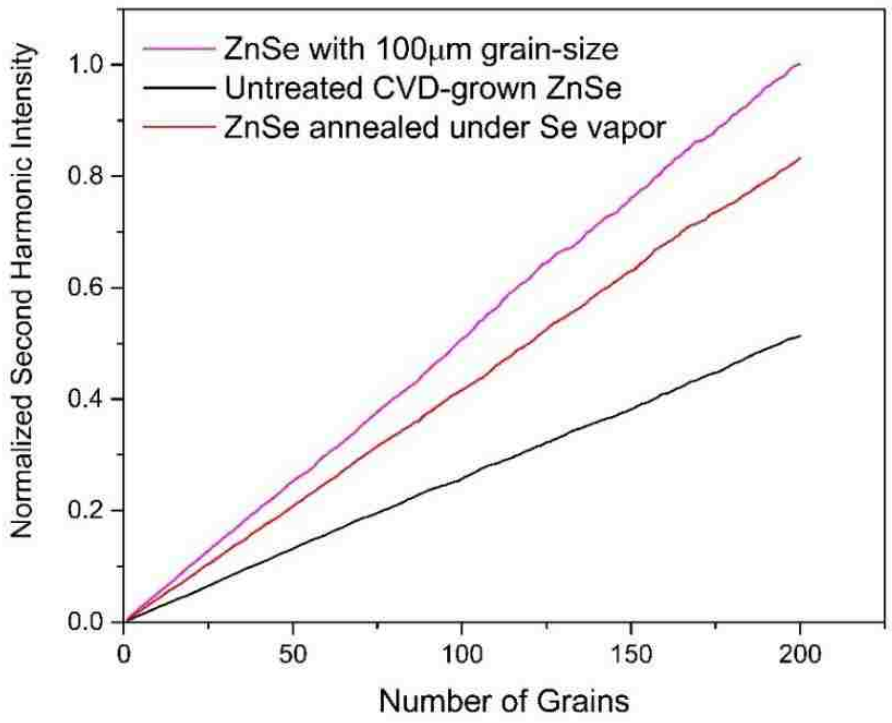

Figure 59. Monte Carlo simulations of the normalized SH intensity as a function of number of grains for varied ZnSe ceramics (see text for details).

5.3 Conclusion

Solid-state grain-coarsening treatments of CVD polycrystalline ZnSe can be used to match the grain-size of this nonlinear material to the coherence length of a mid-IR pump. We have shown that the use of non-stoichiometric grain-growth heat-treatments allow for the control of the speed of the process and of the final grain-size distribution. **When exposed to selenium vapor at 850°C, a faster homogeneous grain-growth could be obtained compared to treatments in a Zn vapor or a vacuum.** We have quantified the effect of grain-size distribution in the process of random quasi-phase-matching and shown that the conversion efficiency scales linearly with the number of

grains and a narrow grain-size distribution yields a higher conversion efficiency. Our Monte-Carlo simulations show that, for particular pumping conditions in the mid-infrared, **the conversion efficiency of a selenium-treated sample could reach 83% of that of an ideal monodisperse microstructure and perform 62% better than an untreated CVD-grown ceramic**.

CHAPTER SIX: CHARACTERIZATION OF NONLINEAR OPTICAL PROPERTIES OF ZnSe CERAMICS

To characterize ZnSe ceramics from the viewpoint of random quasi-phase-matching [42, 138, 139] and their suitability for acting as a nonlinear medium in an ultra-broadband subharmonic femtosecond OPO, we have built a nanosecond mid-IR laser setup. Since the final goal is to demonstrate a broadband frequency comb based on frequency division (subharmonic) process $\omega \rightarrow \omega/2$ in a ring-cavity resonator, with ω corresponding to the pump 2.35 μm wavelength and $\omega/2$ corresponding to the 4.7 μm wavelength, we decided to characterize the samples from the viewpoint of the inverse process of second harmonic generation (SHG) first ($\omega \rightarrow 2\omega$ with ω in the range of 3-5 μm, and 2ω at 1.5-2.5 μm). Both processes are related to each other (through effective second-order nonlinearity in a three-wave mixing process) and hence the samples that are the best from the viewpoint of SHG would be the proper candidates for the subharmonic femtosecond OPO generation. An advantage of the SHG method, in addition to the fact that the process is straightforward, is that we can compare second-order nonlinear coefficient of randomly phase-matched ZnSe ceramics to that of known nonlinear materials.

6.1 Second Harmonic Generation in ZnSe Ceramics

6.1.1 Setup for Second Harmonic Generation

For SHG characterization, we have built an optical parametric oscillator (OPO) based on periodically poled lithium niobate (PPLN) crystal, tunable over the range 2.8 -5 μm (Figure 60).

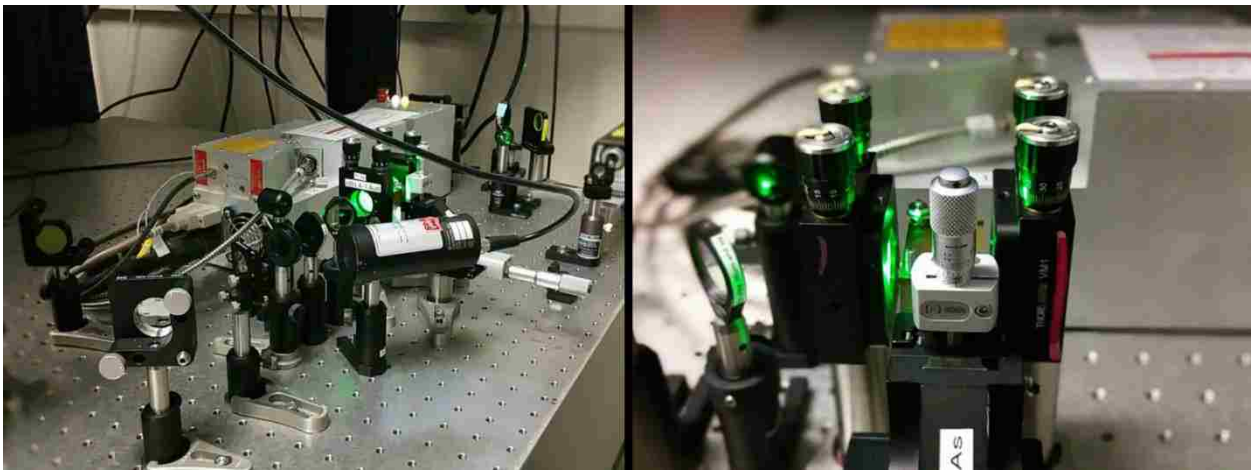

Figure 60. Optical parametric oscillator based on periodically poled lithium niobate (PPLN) crystal, tunable over the range 2.8 -5 μm. Left: OPO and the pump laser. Right: PPLN OPO including mirrors and the oven for PPLN crystal.

The OPO is pumped by a 1064 nm Q-switched diode-pumped Nd:YAG laser (Spectra-Physics Model T40-X30S) with a TEM_{00} transverse mode, 20-ns pulse duration, and 1.5-mJ pulse energy, operating at 100 Hz -1 kHz repetition rate. We used a simple flat-flat PPLN OPO. The front and rear OPO mirrors (M1 and M2 in Figure 61) have same characteristics and are transmissive for the pump and the idler waves, and highly reflective (98%) for the signal wave. The PPLN crystal is 20 mm long, 25 mm wide and 1 mm thick. The pump laser beam size inside the PPLN crystal is around 250 μm. After PPLN OPO, a 45º beam splitter (BS) is used to reject the OPO signal wave (1.35-1.7 μm), as well as the pump, and transmits only the OPO idler wave at 2.8-5 μm. An additional long pass filter is used to make sure that only a long wavelength component (> 2.5 μm) goes through. The beam is focused to a 60-μm spot with a CaF_2 lens. A ZnSe sample is placed in the focus and scanned in the XY-plane at different rotation angles φ. The SHG signal is measured using an InGaAs detector with a short-pass filter to block the fundamental wave at frequency ω.

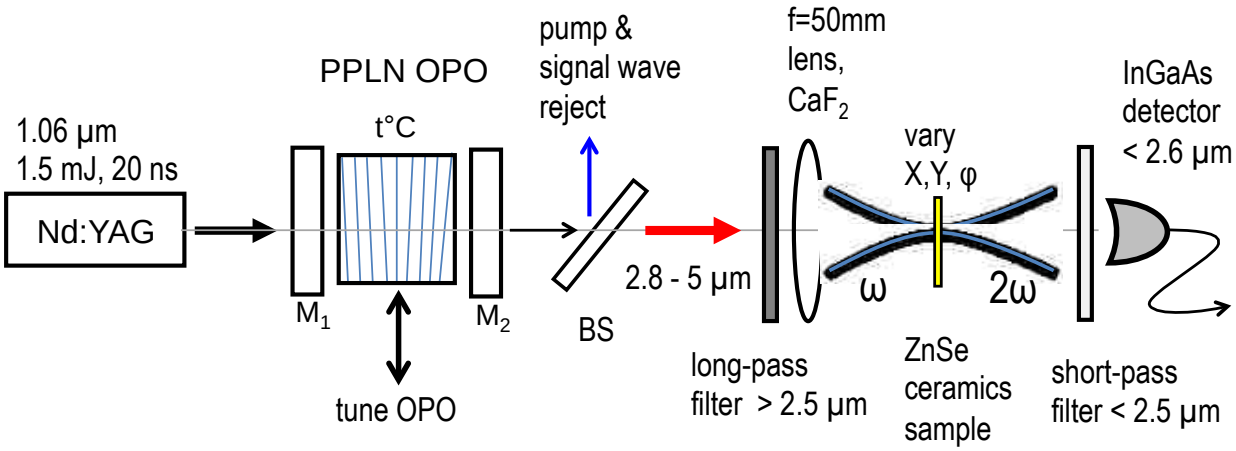

Figure 61. Setup for characterization of ZnSe ceramic samples via SHG.

6.1.2 Characterization of the Beam

The tunable wavelength of the PPLN OPO was achieved by linear motion of the crystal across the beam at a certain crystal temperature (Figure 62). The PPLN OPO idler wave energy amounted to 50-100 µJ with the linewidth in the range 10-50 cm^{-1}.

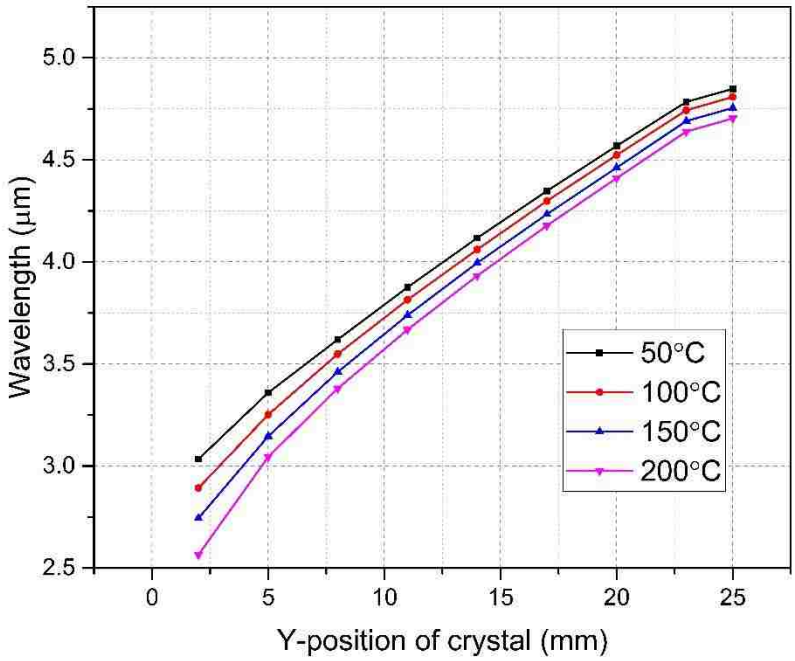

Figure 62. Wavelength tuning of PPLN OPO as a function of Y-position of the crystal.

The propagation of Gaussian beam is shown in Figure 63. Beam waist (w_0) is defined as the beam radius where beam width is the smallest. The beam radius varies as the distance from the waist because of the divergence. We defined the Rayleigh's range (z_0) as the distance where the area of the beam is twice bigger than the area in the waist.

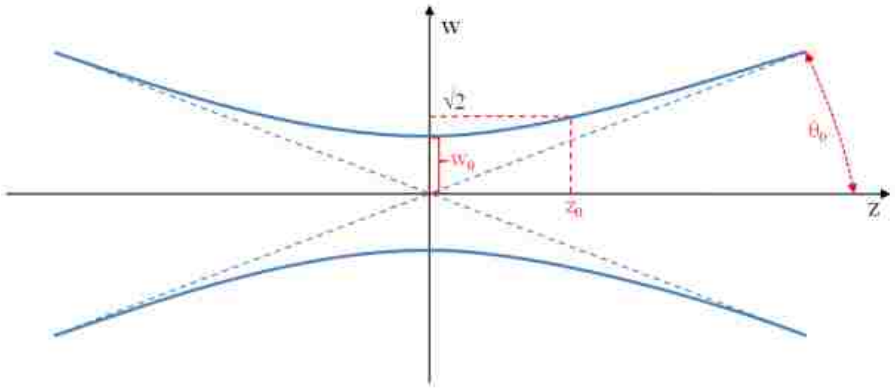

Figure 63. Propagation of the Gaussian beam.

In laser application, the beam quality (M^2) is very important because it defines the smallest possible beam area in the focal point, which can be calculated by:

$$w_0\theta_0 = \frac{w_0^2}{z_0} = \theta_0^2 z_0 = M^2 \frac{\lambda}{\pi} \tag{55}$$

where θ_0 is a beam divergence. For perfect Gaussian beam, M^2 equals to 1. However, in normal case, M^2 is always greater than 1 because of nonhomogeneity and diffraction loses. We used the knife-edge method to determine the M^2 parameter. The principle of knife-edge method is shown in Figure 64. We used a CaF_2 lens with f=50 mm to focus the OPO beam. In this work, we picked up 5 different wavelengths (3.1 μm, 3.5 μm, 3.98 μm, 4.29 μm, 4.73 μm). The distance between the focus point and CaF_2 lens, the pulse energy, beam waist w_0 and M^2 are shown in Figure 65. The beam quality parameter was calculated to be $M^2 \approx 1.5$.

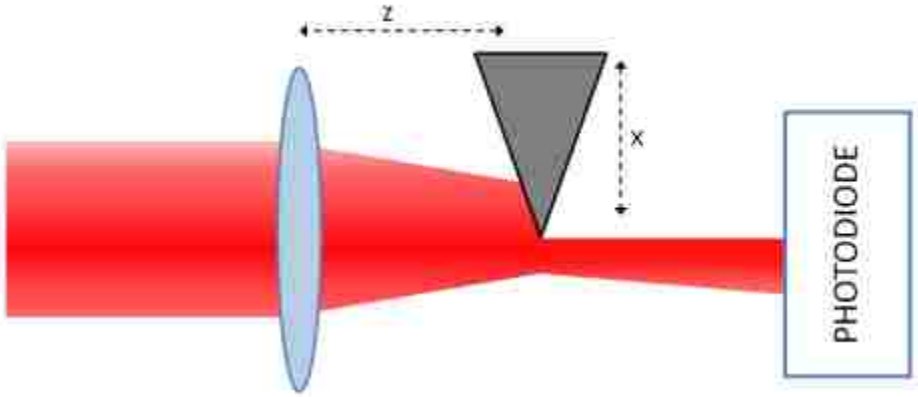

Figure 64. Principle of knife-edge method.

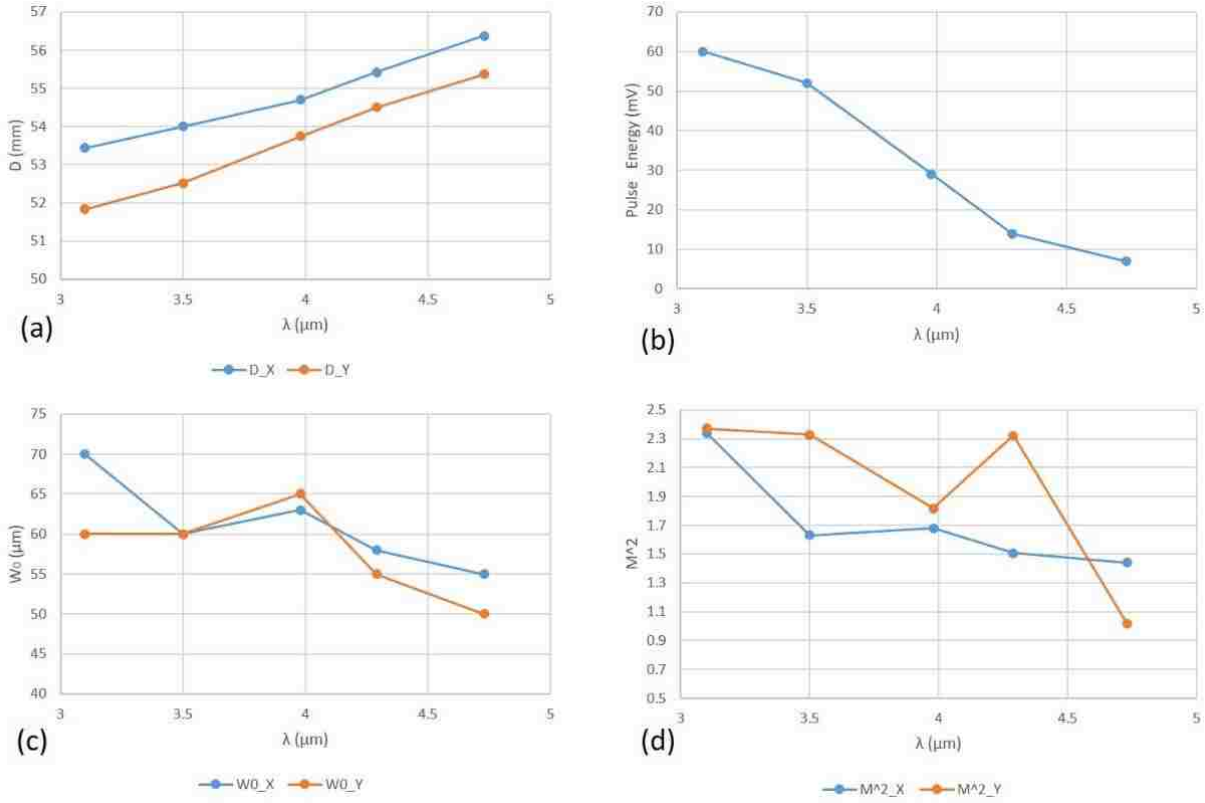

Figure 65. (a) The distance between the focus point and CaF_2 lens; (b) pulse energy; (c) beam waist w_0 and (d) beam quality M^2 as a function of wavelength.

6.1.3 Results and Discussion

The purchased ZnSe ceramic samples were cut and polished into plane-parallel slabs (5×5 mm) with different thicknesses suitable for SHG experiments. Alumina powder dispersions were used as polishing agent. Polishing spec is very important when characterized the optical properties (Table 10). Zygo is used to check the polishing quality (Figure 66). The root mean square (RMS) value is only 0.005 μm.

Table 10 Polishing standard specification.

Polishing Surface	5x5 mm facets
Flatness	λ/8@632 nm
Scratch/Dig	20/10
Parallelism	<30 arcsec
Chamfer	0.1mm @45_0
Clear Aperture	90% of the side
Height Tolerance	±0.5 mm
Width Tolerance	±0.5 mm
Length Tolerance	±0.05 mm

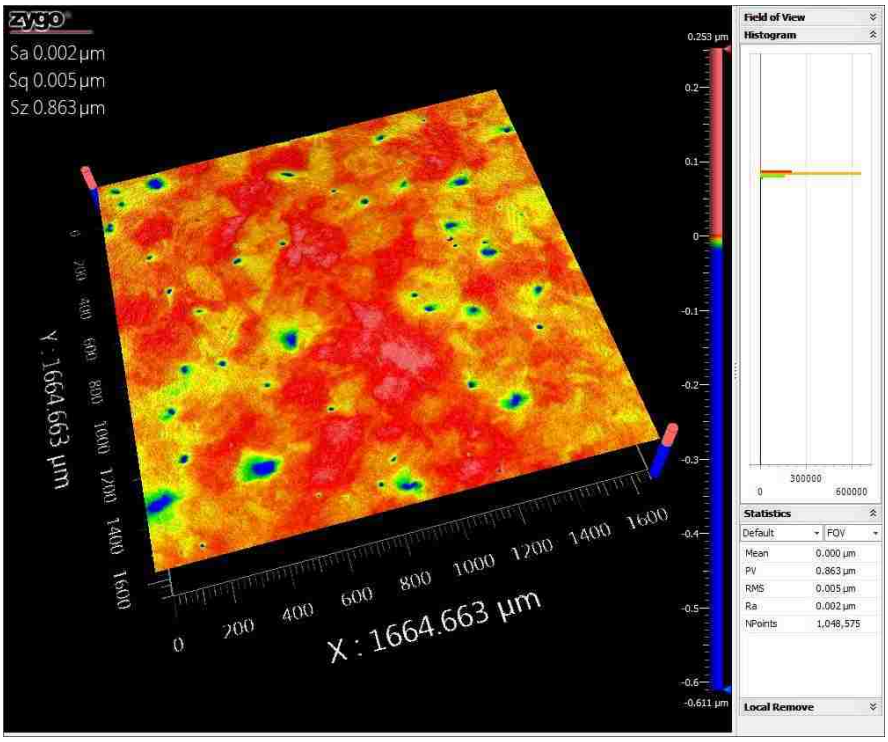

Figure 66. Polishing finish from Zygo.

6.1.3.1 Second-Harmonic Generation of ZnSe Samples with Different Thickness

There are four samples with different thickness (0.5 mm, 1 mm, 2 mm and 5 mm) from the same origin (II-VI Inc., USA). Step motors (MFA-CC, Newport) were used to scan the whole ceramics samples. The step was set as 50 µm and pump wavelength we used here is 3.86 µm. The second harmonic generation signal are shown in Figure 67 and Table 11. Maximum value will be used in a broadband frequency comb based on frequency division (subharmonic) process. Here, we only use average value to characterize the second-order nonlinear optical properties of ZnSe ceramics (Figure 68). The main feature of the random quasi-phase-matching is proven experimentally that the frequency conversion is proportional to the sample thickness.

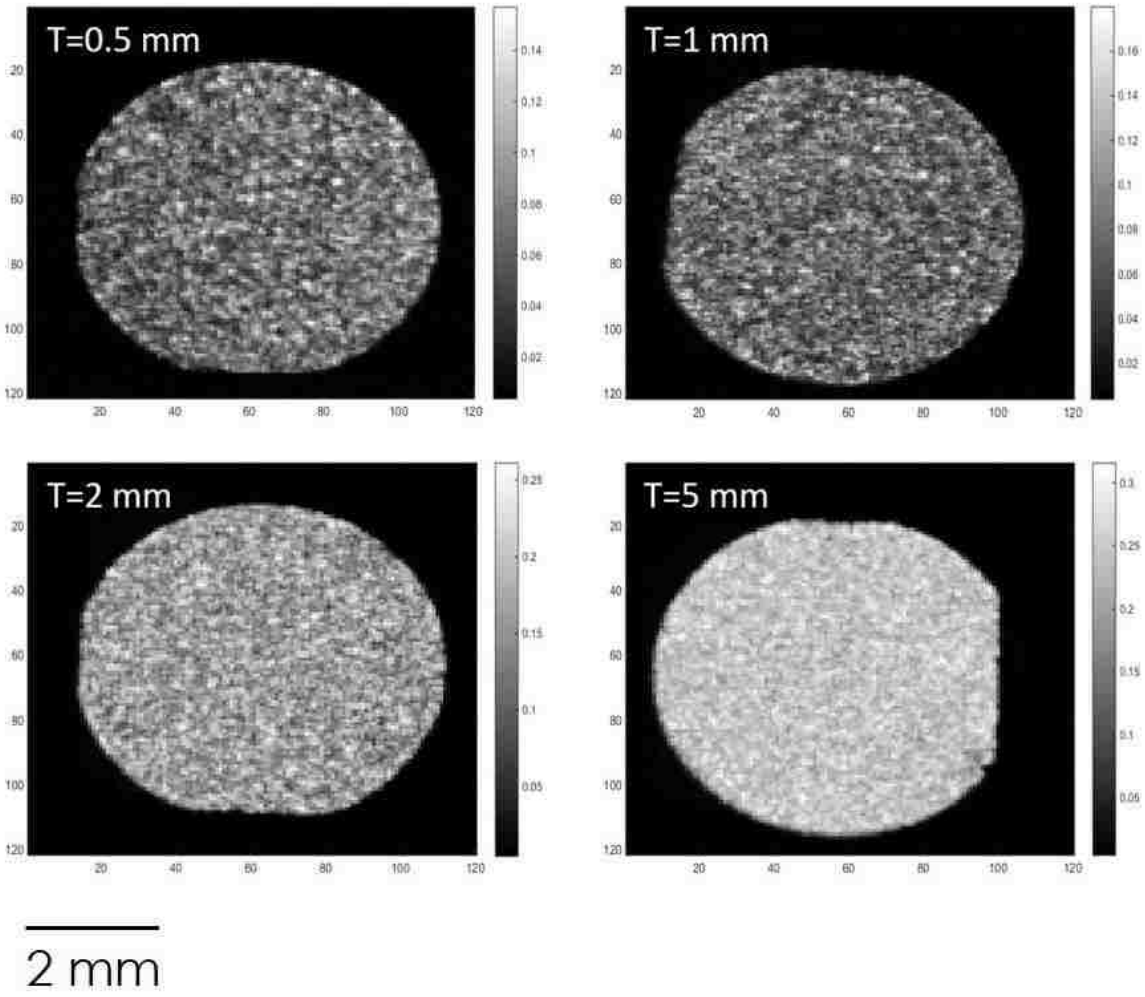

Figure 67. Second-harmonic generation scanning signal as a function of sample thickness.

Table 11 Maximum and average value of second harmonic generation signal.

Thickness (mm)	Maximum Signal (w)	Average Signal (w)	Standard Deviation
0.5	0.1568	0.0721	0.0219
1	0.18	0.0782	0.0245
2	0.2611	0.1589	0.0354
5	0.3156	0.2376	0.0328

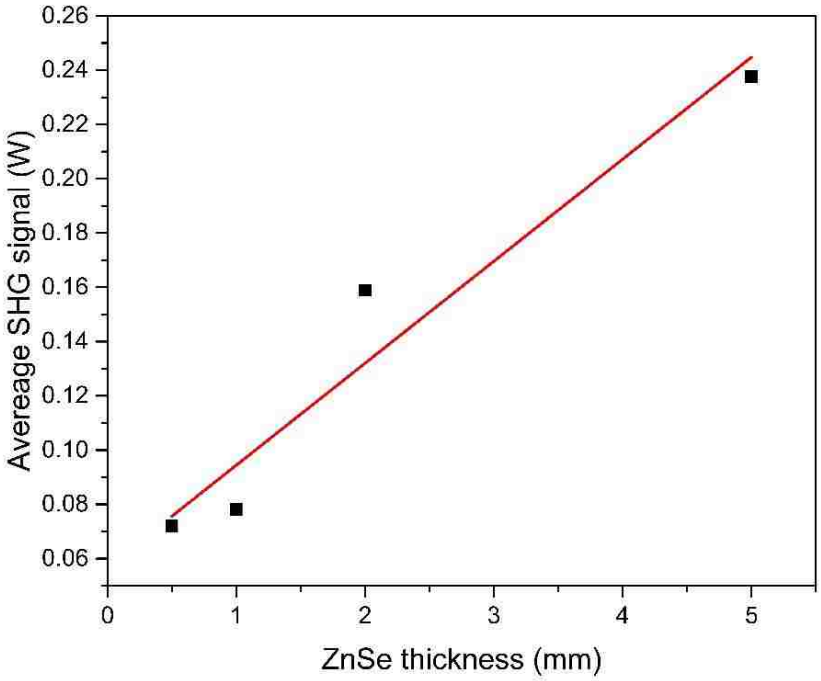

Figure 68. Average second-harmonic generation as a function of ZnSe ceramics thickness.

6.1.3.2 Second-Harmonic Generation of ZnSe Samples with Different Grain Size

Based on Chapter 5, we studied non-stoichiometric grain-growth in CVD-grown ZnSe ceramics. Through this method, we fabricated four samples with same thickness (1.5 mm) but different grain-size in order to study the effect of grain size on the second-harmonic generation. The pump wavelength we used here is 4.7 μm and hence the coherence length is 100 μm. The second-harmonic generation signal were reported in Table 12 and Figure 69. When grain size close to coherence length (100 μm), the SHG signal is higher and when grain size is twice of the coherence length, the SHG signal is lower. This experiment confirmed the theory. When we change the crystal orientation at each coherence length, the electric field and intensity is the highest and. While, when we change crystal orientation every twice of the coherence length, the electric field and intensity is the lowest.

Table 12 Conditions and second-harmonic generation signal of ZnSe ceramic samples.

	ZnSe#1	**ZnSe#2**	**ZnSe#3**	**ZnSe#4**
Thickness (mm)	1.5	1.5	1.5	1.5
Grain Size (μm)	75	100	101	194
Average SHG Signal (mV)	293	329	306	75

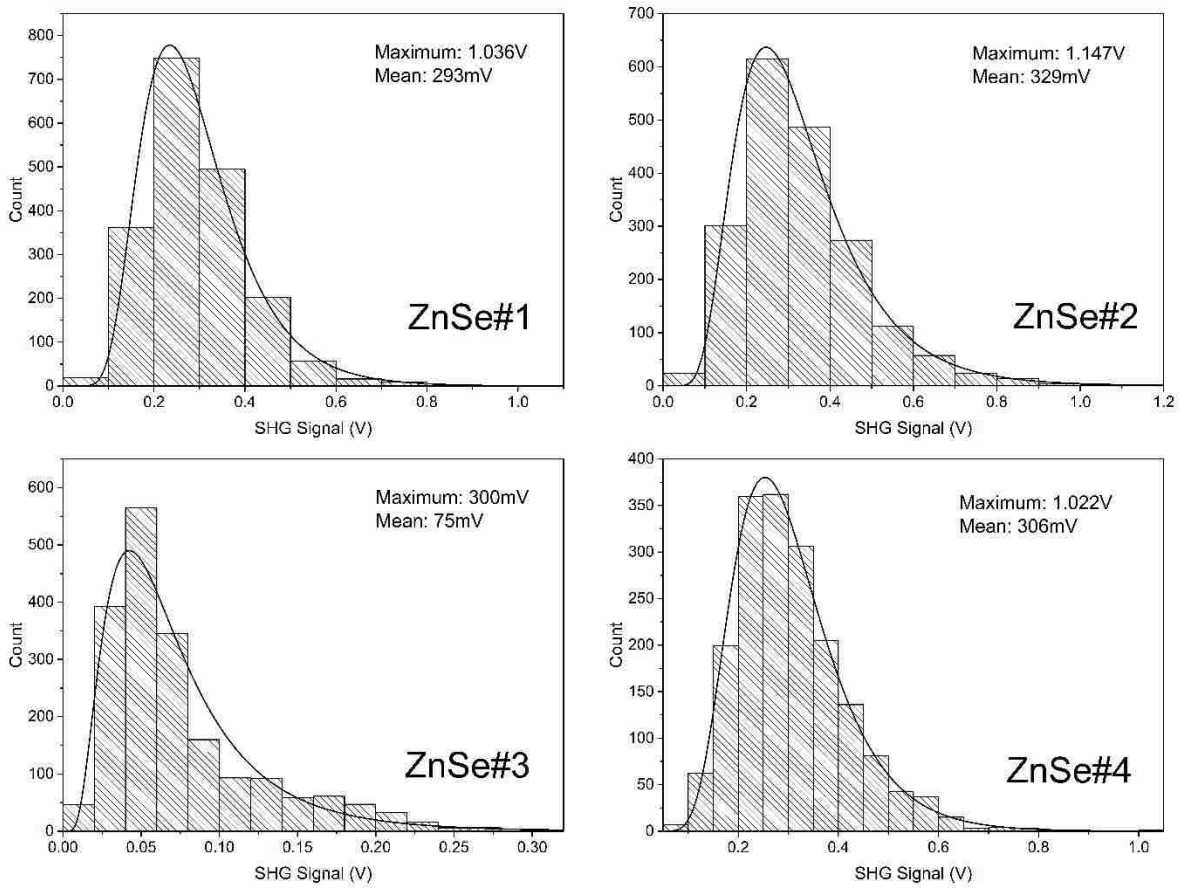

Figure 69. Second-harmonic generation signal histogram.

6.2 Optical Parametric Oscillation in ZnSe ceramics

The OPO was pumped by a Kerr-lens locked Cr:ZnS laser. The center wavelength is 2.35 μm, the pulse duration is 62 femtosecond and repetition rate is 79 MHz. The OPO cavity (Figure 70) was composed of an in-coupling dielectric mirror (M1) with a high transmission (>85%) for the 2.35 μm pump and a high reflection (>95%) for 3-8 μm, two gold-coated parabolic mirrors (M2 and M3) with a 30° off-axis angle and one gold-coated flat mirrors (M4). A 1.5 mm thick

ZnSe ceramic was placed at Brewster angle between two parabolic mirrors. ZnSe wedge was used inside the cavity for variably outcoupling the OPO signal/idler waves[4].

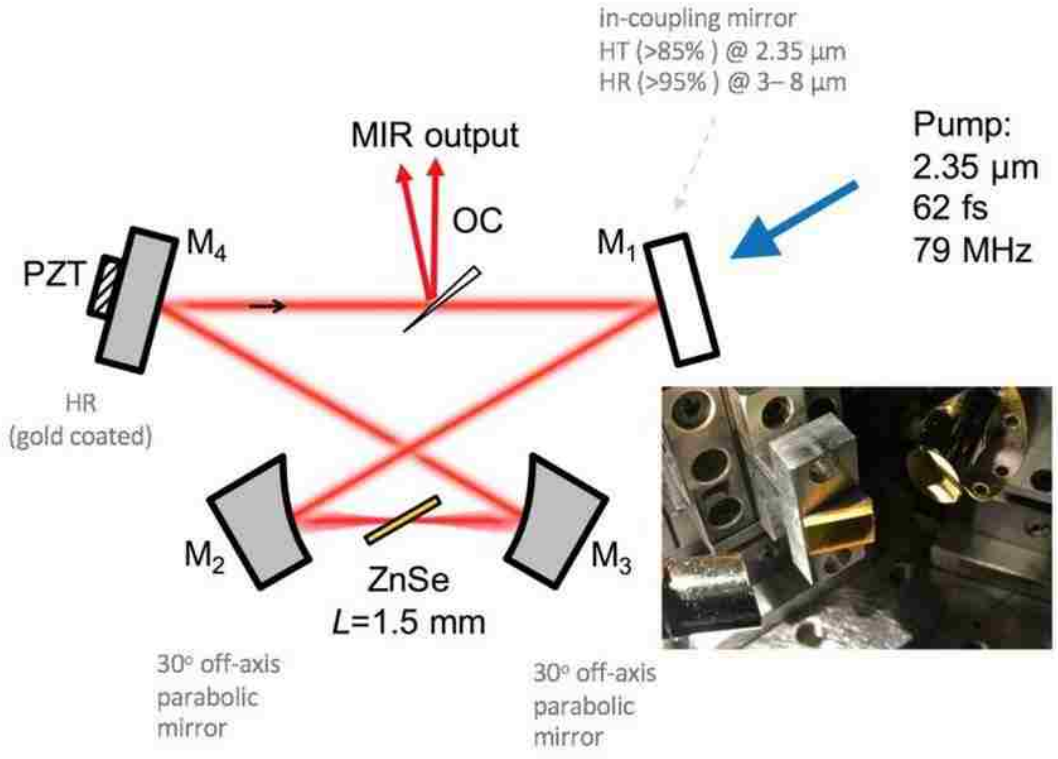

Figure 70. Schematic of the Optical Parametric Oscillator.

The OPO was operating in a doubly resonant frequency-divide-by-2 mode at degeneracy. We used a monochromator and a mercury cadmium telluride (MCT) detector to measure the output spectrum, which spanned 3–7.5 µm (at -40 dB level) and was centered at the 4.7 µm subharmonic of the pump (Figure 71) [44].

[4]These results have been published in Ru, Q., Lee, N., Chen, X., Zhong, K., Tsoy, G., Mirov, M., Vasilyev, S., Mirov S.B. & Vodopyanov, K. L. (2017). Optical parametric oscillation in a random polycrystalline medium. *Optica*, *4*(6), 617-618.

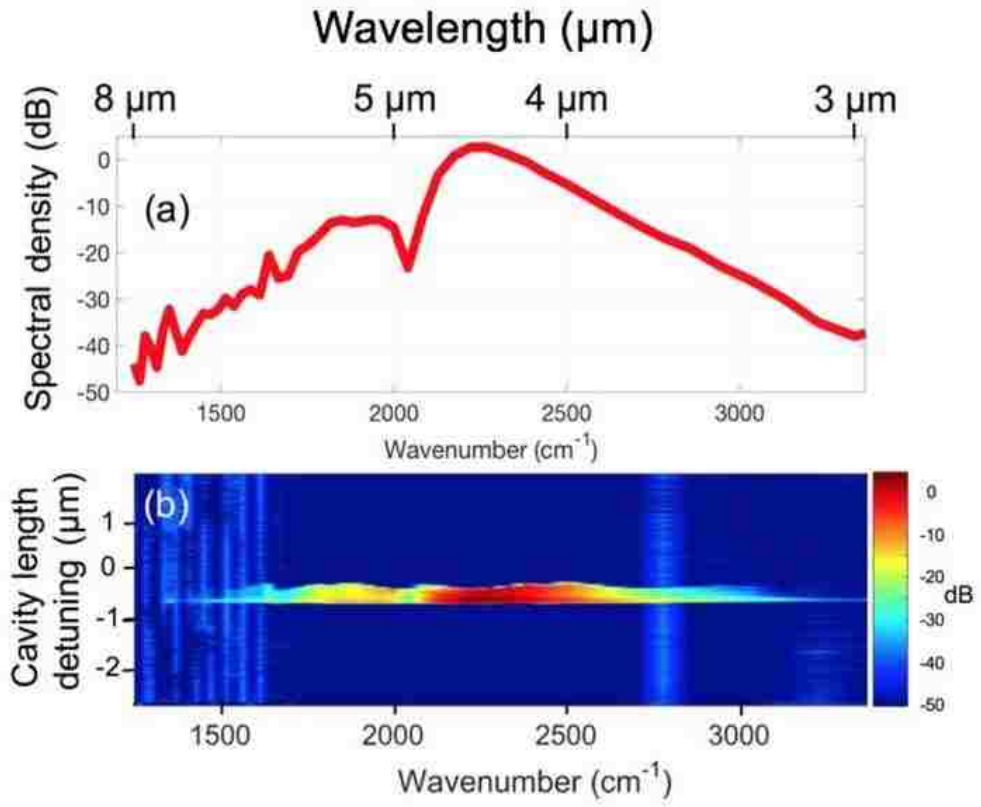

Figure 71. Top: the OPO output spectrum showing a continuous spectral span of 3-7.5 μm. Bottom: 2D spectrum.

6.3 Conclusion

We have experimentally proven the main feature of the random quasi-phase-matching, that is, the frequency conversion linearly depends on sample thickness. In random quasi-phase-matching, nonlinear conversion efficiency is maximized when the average grain size of ceramics is close to the coherence length. We also demonstrate **the first OPO based on random quasi-phase-matching in ZnSe ceramics and produced an ultra-broadband spectrum spanning 3-7.5 μm**.

CHAPTER SEVEN: CONCLUSIONS

There are a lot of technologies that rely on the conversion of short laser pulses from one spectral domain to another. Nonlinear optical (NLO) materials are key components in the conversion of ultrashort laser pulses by allowing all frequencies of a pulse to be converted simultaneously. The use of quasi phase-matching (QPM) materials results in a narrow bandwidth of efficiently converted frequencies and the fabrication of periodically-poled crystals is challenging. Optical ceramics with non-centrosymmetric point group, offer new options in widening the NLO spectral bandwidth. Despite the lack of long range order, these materials can serve as efficient nonlinear frequency converters by way of the random quasi-phase-matching (rQPM) process. Compared to ordered crystals, disordered polycrystalline materials show a significant enhancement in spectral and angular acceptances and a better tolerance to both propagation angle and temperature, which are essential in converting femtosecond pulse lasers. Additionally, these materials have good thermal and mechanical properties and their fabrication is scalable in size, making them highly suitable for high-energy applications. In this dissertation, we investigated the fabrication of transparent and microstructure-engineered ferroelectric ceramics of the PMN-PT composition. Solid-state grain-coarsening was used to fabricate ZnSe ceramics with a desired grain-size. We have characterized the nonlinear optical properties of ZnSe ceramics by second-harmonic-generation and demonstrated an OPO based on random quasi-phase-matching in transparent ZnSe ceramics.

First, we have developed a novel glycine–nitrate combustion method to fabricate lead oxide nanopowders, which have smaller particle size than commercial powders. We have fabricated PMN-PT transparent ceramics with better transparency using these combustion synthesized lead

oxide powders, which helps improve the densification of green-bodies and the transparency of PMN–PT ceramics.

We have investigated the phase and microstructure evolution of PMN-PT ceramics sintered with different dopants and found that, compared to other dopants, La-doped PMN-PT samples do not form a liquid phase during sintering and favor the formation of a pure perovskite phase with unimodal rounded grains. We found that the preferential A-site occupancy of La^{3+} resulting from its larger ionic radius lowers the oxygen vacancy concentration. As a result, grain growth of La-doped PMN-PT is suppressed compared to samples doped with smaller ions such as Y^{3+} and Gd^{3+}.

Our simulation of the second-order nonlinear susceptibility in pseudo-cubic PMN-PT ceramics indicate that the second-order susceptibility is too small to be practical most likely because of the small departure from centrosymmetry.

We have developed a solid-state non-stoichiometric coarsening treatment of CVD polycrystalline ZnSe to match the grain-size of this nonlinear material to the coherence length of a mid-IR pump. We have shown that the use of non-stoichiometric grain-growth heat-treatments provides an accelerated means to coarsen the microstructure and allow for the control of the speed of the process and of the final grain-size distribution. When exposed to selenium vapor at 850°C, a faster homogeneous grain-growth could be obtained compared to treatments in a Zn vapor or a vacuum. We have quantified the effect of grain-size distribution in the process of random quasi-phase-matching and shown that the conversion efficiency scales linearly with the number of grains and a narrow grain-size distribution yields a higher conversion efficiency. Our Monte-Carlo simulations show that, for particular pumping conditions in the mid-infrared, the conversion

efficiency of a selenium-treated sample could reach 83% of that of an ideal monodisperse microstructure and perform 62% better than an untreated CVD-grown ceramic.

Finally, we have proven using experimental method that nonlinear conversion efficiency is maximized when the average grain-size of the ceramic is equal to the coherence length for the wavelengths of interest. The main feature of rQPM is the linear dependency of the frequency conversion yield with sample thickness. We firstly demonstrate an OPO based on random quasi-phase-matching in ZnSe ceramics and produced an ultra-broadband spectrum spanning 3-7.5 μm.

APPENDIX A: PUBLICATIONS

Journal Publications:

Chen, X. & Gaume, R. Non-stoichiometric grain-growth in ZnSe ceramics for khi2 interaction. *Optical Materials Express*, submitted.

Chen, X., Chen, S., Bruner, A., & Gaume, R. (2018). Effects of dopants on the microstructure and phase-purity control in PMN-PT ceramics. *Ceramics International*, *44(*15*)*, 17909-17913.

Ru, Q., Lee, N., **Chen, X.**, Zhong, K., Tsoy, G., Mirov, M., Vasilyev, S., Mirov S.B. & Vodopyanov, K. L. (2017). Optical parametric oscillation in a random polycrystalline medium. *Optica*, *4*(6), 617-618.

Chen, X., Chen, S., Clequin, P. M., Shoulders, W. T., & Gaume, R. (2015). Combustion synthesis of lead oxide nanopowders for the preparation of PMN–PT transparent ceramics. *Ceramics International*, *41*(1), 755-760.

Conference Proceedings

Ru, Q., Lee, N., **Chen, X.**, Zhong, K., Vasilyev, S., Mirov, M., Vasilyev, S., Mirov S.B. & Vodopyanov, K. L. (2018, May). Optical parametric oscillation in random polycrystalline χ (2) medium. In *CLEO: Science and Innovations* (pp. STh4F-3). Optical Society of America.

Ru, Q., Kawamori, T., Lee, N., **Chen, X.**, Zhong, K., Mirov, M., Vasilyev, S., Mirov S.B. & Vodopyanov, K. L. (2018, February). Optical parametric oscillation in a random poly-crystalline medium: ZnSe ceramic. In *Nonlinear Frequency Generation and Conversion: Materials and Devices XVII* (Vol. 10516, p. 1051615). International Society for Optics and Photonics.

Oral Presentations

Chen, X., Chen, S. & Gaume, R., Effect of dopants on the microstructure evolution and sintering kinetics of PMN-PT ceramics, Materials Science & Technology 2017, Pittsburgh, Pennsylvania.

Chen, X., Chen, S., Clequin, P., Shoulders, W.T., and Gaume, R., Combustion synthesis of lead oxide nanopowders for the preparation of PMN-PT transparent ceramics, Glass and Optical Materials Division (GOMD) Meeting 2015, Miami, Florida.

APPENDIX B: PERMISSION FOR COPYRIGHTED MATERIALS

Section 2.2 in Chapter 2 adapted with permission from:

• Chen, X., Chen, S., Clequin, P. M., Shoulders, W. T., & Gaume, R. (2015). Combustion synthesis of lead oxide nanopowders for the preparation of PMN–PT transparent ceramics. *Ceramics International*, *41*(1), 755-760

https://www.sciencedirect.com/science/article/pii/S0272884214013807

Chapter 3 adapted with permission from:

• Chen, X., Chen, S., Bruner, A., & Gaume, R. (2018). Effects of dopants on the microstructure and phase-purity control in PMN-PT ceramics. *Ceramics International*, *44(*15*)*, 17909-17913.

https://www.sciencedirect.com/science/article/pii/S0272884218317097

Section 6.2 in Chapter 6 adapted with permission from:

• Ru, Q., Lee, N., Chen, X., Zhong, K., Tsoy, G., Mirov, M., Vasilyev, S., Mirov S.B. & Vodopyanov, K. L. (2017). Optical parametric oscillation in a random polycrystalline medium. *Optica*, *4*(6), 617-618.

https://www.osapublishing.org/optica/abstract.cfm?uri=optica-4-6-617

LIST OF REFERENCES

1. Baer, T., *Large-amplitude fluctuations due to longitudinal mode coupling in diode-pumped intracavity-doubled Nd: YAG lasers.* JOSA B, 1986. **3**(9): p. 1175-1180.
2. Kane, T.J. and R.L. Byer, *Monolithic, unidirectional single-mode Nd: YAG ring laser.* Optics letters, 1985. **10**(2): p. 65-67.
3. Krell, A., et al., *Transparent sintered corundum with high hardness and strength.* Journal of the American Ceramic Society, 2003. **86**(1): p. 12-18.
4. Patel, P.J., et al. *Transparent ceramics for armor and EM window applications*. in *Inorganic Optical Materials II*. 2000. International Society for Optics and Photonics.
5. Greskovich, C. and S. Duclos, *Ceramic scintillators.* Annual review of materials science, 1997. **27**(1): p. 69-88.
6. Jiang, H., et al. *Transparent electro-optic ceramics and devices*. in *Optoelectronic Devices and Integration*. 2005. International Society for Optics and Photonics.
7. Wei, G., *Transparent ceramic lamp envelope materials.* Journal of Physics D: Applied Physics, 2005. **38**(17): p. 3057.
8. Peuchert, U., et al., *Transparent cubic-ZrO2 ceramics for application as optical lenses.* Journal of the European Ceramic Society, 2009. **29**(2): p. 283-291.
9. Segal, D., *Chemical synthesis of ceramic materials.* Journal of Materials Chemistry, 1997. **7**(8): p. 1297-1305.
10. Xicheng, W., *SYNTHESIS OF Pb (Zr xTi 1-x) O 3 CERAMIC POWDER BY WETCHEMICAL METHOD [J]*. JOURNAL OF THE CHINESE CERAMIC SOCIETY, 1997. **5**.

11. Tas, A.C., et al., *An investigation of the chemical synthesis and high-temperature sintering behaviour of calcium hydroxyapatite (HA) and tricalcium phosphate (TCP) bioceramics.* Journal of Materials Science: Materials in Medicine, 1997. **8**(2): p. 91-96.

12. Ikesue, A., et al., *Fabrication and optical properties of high-Performance polycrystalline Nd: YAG ceramics for solid-State lasers.* Journal of the American Ceramic Society, 1995. **78**(4): p. 1033-1040.

13. Ikesue, A., I. Furusato, and K. Kamata, *Fabrication of Polycrystal line, Transparent YAG Ceramics by a Solid-State Reaction Method.* Journal of the American Ceramic Society, 1995. **78**(1): p. 225-228.

14. Wen, L., et al., *Synthesis of nanocrystalline yttria powder and fabrication of transparent YAG ceramics.* Journal of the European Ceramic Society, 2004. **24**(9): p. 2681-2688.

15. Haertling, G.H., *Ferroelectric ceramics: history and technology.* Journal of the American Ceramic Society, 1999. **82**(4): p. 797-818.

16. Munir, Z., U. Anselmi-Tamburini, and M. Ohyanagi, *The effect of electric field and pressure on the synthesis and consolidation of materials: A review of the spark plasma sintering method.* Journal of Materials Science, 2006. **41**(3): p. 763-777.

17. Kim, B.-N., et al., *Spark plasma sintering of transparent alumina.* Scripta Materialia, 2007. **57**(7): p. 607-610.

18. Li, J.F., et al., *Ferroelectric and piezoelectric properties of fine-grained Na0. 5K0. 5NbO3 lead-free piezoelectric ceramics prepared by spark plasma sintering.* Journal of the American Ceramic Society, 2006. **89**(2): p. 706-709.

19. Chaim, R., R. Marder-Jaeckel, and J. Shen, *Transparent YAG ceramics by surface softening of nanoparticles in spark plasma sintering.* Materials Science and Engineering: A, 2006. **429**(1): p. 74-78.

20. Seidel, M., et al., *Multi-watt, multi-octave, mid-infrared femtosecond source.* Science advances, 2018. **4**(4): p. eaaq1526.

21. Trebino, R., *Frequency-resolved optical gating: the measurement of ultrashort laser pulses*. 2012: Springer Science & Business Media.

22. Pasiskevicius, V., *Nonlinear crystals for solid-state lasers*, in *Handbook of Solid-State Lasers*. 2013, Elsevier. p. 139-167.

23. Butcher, P.N. and D. Cotter, *The elements of nonlinear optics*. Vol. 9. 1991: Cambridge university press.

24. Boyd, R.W., *Nonlinear optics*. 2003: Elsevier.

25. Armstrong, J., et al., *Interactions between light waves in a nonlinear dielectric.* Physical Review, 1962. **127**(6): p. 1918.

26. Yamada, M., et al., *First-order quasi-phase matched LiNbO3 waveguide periodically poled by applying an external field for efficient blue second-harmonic generation.* Applied Physics Letters, 1993. **62**(5): p. 435-436.

27. Gordon, L., et al., *Diffusion-bonded stacked GaAs for quasiphase-matched second-harmonic generation of a carbon dioxide laser.* Electronics Letters, 1993. **29**(22): p. 1942-1944.

28. Zheng, D., et al., *Diffusion bonding of GaAs wafers for nonlinear optics applications.* Journal of the Electrochemical Society, 1997. **144**(4): p. 1439-1441.

29. Myers, L.E., et al., *Quasi-phase-matched optical parametric oscillators in bulk periodically poled LiNbO 3.* JOSA B, 1995. **12**(11): p. 2102-2116.

30. Myers, L.E., et al., *Multigrating quasi-phase-matched optical parametric oscillator in periodically poled LiNbO 3.* Optics letters, 1996. **21**(8): p. 591-593.

31. Myers, L., et al., *Quasi-phase-matched 1.064-μm-pumped optical parametric oscillator in bulk periodically poled LiNbO 3.* Optics letters, 1995. **20**(1): p. 52-54.

32. Vodopyanov, K., et al., *Terahertz-wave generation in quasi-phase-matched GaAs.* Applied Physics Letters, 2006. **89**(14): p. 141119.

33. Vodopyanov, K.L., et al., *Optical parametric oscillation in quasi-phase-matched GaAs.* Optics letters, 2004. **29**(16): p. 1912-1914.

34. Schunemann, P.G., L.A. Pomeranz, and D.J. Magarrell. *Optical parametric oscillation in quasi-phase-matched GaP*. in *Nonlinear Frequency Generation and Conversion: Materials, Devices, and Applications XIV*. 2015. International Society for Optics and Photonics.

35. Tassev, V., et al. *Progress in orientation-patterned GaP for next-generation nonlinear optical devices*. in *Nonlinear Frequency Generation and Conversion: Materials, Devices, and Applications XII*. 2013. International Society for Optics and Photonics.

36. Tassev, V., et al., *Epitaxial growth of quasi-phase matched GaP for nonlinear applications: Systematic process improvements.* Journal of Crystal Growth, 2012. **352**(1): p. 72-77.

37. Zhang, C., et al., *Electric poling and relaxation of thermoset polyurethane second-order nonlinear optical materials: Role of cross-linking and monomer rigidity.* Macromolecules, 2001. **34**(2): p. 235-243.

38. Xu, J., et al., *Second harmonic generation investigation on electric poling effects in fused silica.* Optical Materials, 1997. **8**(4): p. 243-247.

39. Chang, L.L. and K. Ploog, *Molecular beam epitaxy and heterostructures*. Vol. 87. 2012: Springer Science & Business Media.

40. Morozov, E.Y., et al., *Second optical harmonic generation in nonlinear crystals with a disordered domain structure.* Journal of Experimental and Theoretical Physics Letters, 2001. **73**(12): p. 647-650.

41. Morozov, E.Y. and A.S. Chirkin, *Stochastic quasi-phase matching in nonlinear-optical crystals with an irregular domain structure.* Quantum Electronics, 2004. **34**(3): p. 227-232.

42. Baudrier-Raybaut, M., et al., *Random quasi-phase-matching in bulk polycrystalline isotropic nonlinear materials.* Nature, 2004. **432**(7015): p. 374-376.

43. Sorokin, E. and I.T. Sorokina. *Femtosecond operation and random quasi-phase-matched self-doubling of ceramic Cr: ZnSe laser*. in *Lasers and Electro-Optics (CLEO) and Quantum Electronics and Laser Science Conference (QELS), 2010 Conference on*. 2010. IEEE.

44. Ru, Q., et al., *Optical parametric oscillation in a random polycrystalline medium.* Optica, 2017. **4**(6): p. 617-618.

45. Ru, Q., et al. *Optical parametric oscillation in a random poly-crystalline medium: ZnSe ceramic*. in *Nonlinear Frequency Generation and Conversion: Materials and Devices XVII*. 2018. International Society for Optics and Photonics.

46. Mirov, S., et al., *Frontiers of mid-IR lasers based on transition metal doped chalcogenides.* IEEE Journal of Selected Topics in Quantum Electronics, 2018.

47. Vidal, X. and J. Martorell, *Generation of light in media with a random distribution of nonlinear domains.* Physical review letters, 2006. **97**(1): p. 013902.

48. Jankowski, M., et al., *Temporal simultons in optical parametric oscillators.* Physical Review Letters, 2018. **120**(5): p. 053904.

49. Jiang, H., et al. *Transparent electro-optic ceramics and devices*. in *Photonics Asia 2004*. 2005. International Society for Optics and Photonics.

50. Ye, Z.-G. and M. Dong, *Morphotropic domain structures and phase transitions in relaxor-based piezo-/ferroelectric (1− x) Pb (Mg 1/3 Nb 2/3) O 3− x PbTiO 3 single crystals.* Journal of Applied Physics, 2000. **87**(5): p. 2312-2319.

51. Choi, S., J. Jung, and A. Bhalla, *Morphotropic phase boundary in relaxor ferroelectric Pb (Mg1/3Nb2/3) O3 ceramics.* Ferroelectrics, 1996. **189**(1): p. 27-38.

52. Xu, G., et al., *Third ferroelectric phase in PMNT single crystals near the morphotropic phase boundary composition.* Physical Review B, 2001. **64**(2): p. 020102.

53. Park, S.-E. and T.R. Shrout, *Ultrahigh strain and piezoelectric behavior in relaxor based ferroelectric single crystals.* Journal of Applied Physics, 1997. **82**(4): p. 1804-1811.

54. Liu, W. and X. Ren, *Large piezoelectric effect in Pb-free ceramics.* Physical review letters, 2009. **103**(25): p. 257602.

55. Eitel, R.E., et al., *New high temperature morphotropic phase boundary piezoelectrics based on Bi (Me) O3–PbTiO3 ceramics.* Japanese Journal of Applied Physics, 2001. **40**(10R): p. 5999.

56. Noheda, B., et al., *Phase diagram of the ferroelectric relaxor (1− x) PbMg 1/3 Nb 2/3 O 3− x PbTiO 3.* Physical Review B, 2002. **66**(5): p. 054104.

57. Haertling, G.H., *PLZT electrooptic materials and applications—a review.* Ferroelectrics, 1987. **75**(1): p. 25-55.

58. Sun, E. and W. Cao, *Relaxor-based ferroelectric single crystals: Growth, domain engineering, characterization and applications.* Progress in materials science, 2014. **65**: p. 124-210.

59. Baek, J.G., T. Isobe, and M. Senna, *Synthesis of pyrochlore-free 0.9 Pb (Mg1/3Nb2/3) O3-0.1 PbTiO3 ceramics via a soft mechanochemical route.* Journal of the American Ceramic Society, 1997. **80**(4): p. 973-981.

60. Ravindranathan, P., et al., *Synthesis and Dielectric Properties of Solution Sol-Gel-Derived 0.9 Pb (Mg1/3Nb2/3) O3–0.1 PbTiO3 Ceramics.* Journal of the American Ceramic Society, 1991. **74**(12): p. 2996-2999.

61. Sheikh, A.D., H. Kumar, and V. Mathe, *Dielectric properties of chemically co-precipitated tetragonal Pb (Mg1/3Nb2/3) 0.65 Ti0. 35O3.* Solid State Sciences, 2010. **12**(9): p. 1534-1539.

62. Suh, D.-H., D.-H. Lee, and N.-K. Kim, *Phase developments and dielectric/ferroelectric responses in the PMN–PT system.* Journal of the European Ceramic Society, 2002. **22**(2): p. 219-223.

63. Gupta, S., P. Bedekar, and A. Kulkarni, *Synthesis, dielectric and microstructure studies of lead magnesium niobate stabilised using lead titanate.* Ferroelectrics, 1996. **189**(1): p. 17-25.

64. Guha, J.P., D.J. Hong, and H.U. Anderson, *Effect of Excess PbO on the Sintering Characteristics and Dielectric Properties of Pb (Mg1/3Nb2/3) O3–PbTiO3-Based Ceramics.* Journal of the American Ceramic Society, 1988. **71**(3): p. C-152-C-154.

65. Kelly, J., et al., *Effect of Composition on the Electromechanical Properties of (1-x) Pb (Mg1/3Nb2/3) O3− XPbTiO3 Ceramics.* Journal of the American Ceramic Society, 1997. **80**(4): p. 957-964.

66. Ghasemifard, M., S. Hosseini, and G.H. Khorrami, *Synthesis and structure of PMN–PT ceramic nanopowder free from pyrochlore phase.* Ceramics International, 2009. **35**(7): p. 2899-2905.

67. Cascales, C., et al., *The new pyrochlores Pb2 (M0· 5Sb1· 5) O6· 5 (M= Al, Sc, Cr, Fe, Ga, Rh).* Materials research bulletin, 1985. **20**(11): p. 1359-1365.

68. Wakiya, N., et al., *Crystal growth, crystal structure and chemical composition of a pyrochlore type compound in lead-magnesium-niobium-oxygen system.* Materials research bulletin, 1993. **28**(2): p. 137-143.

69. Lejeune, M. and J.P. Boilot, *Influence of ceramic processing on dielectric properties of perovskite type compound: Pb (Mg13, Nb23) O3.* Ceramics international, 1983. **9**(4): p. 119-122.

70. Wang, H.C. and W.A. Schulze, *The role of excess magnesium oxide or lead oxide in determining the microstructure and properties of lead magnesium niobate.* Journal of the American Ceramic Society, 1990. **73**(4): p. 825-832.

71. Kwon, S., E.M. Sabolsky, and G.L. Messing, *Low-Temperature Reactive Sintering of 0.65 PMN· 0.35 PT.* Journal of the American Ceramic Society, 2001. **84**(3): p. 648-650.

72. Gu, H., W.Y. Shih, and W.H. Shih, *Single-Calcination Synthesis of Pyrochlore-Free 0.9 Pb (Mg1/3Nb2/3) O3–0.1 PbTiO3 and Pb (Mg1/3Nb2/3) O3 Ceramics Using a Coating Method.* Journal of the American Ceramic Society, 2003. **86**(2): p. 217-221.

73. Sekar, M.M. and A. Halliyal, *Low-Temperature Synthesis, Characterization, and Properties of Lead-Based Ferroelectric Niobates.* Journal of the American Ceramic Society, 1998. **81**(2): p. 380-388.

74. Maness, P.-C., et al., *Bactericidal activity of photocatalytic TiO2 reaction: toward an understanding of its killing mechanism.* Applied and environmental microbiology, 1999. **65**(9): p. 4094-4098.

75. Alagar, M., T. Theivasanthi, and A.K. Raja, *Chemical synthesis of nano-sized particles of lead oxide and their characterization studies.* arXiv preprint arXiv:1204.0896, 2012.

76. Karami, H., et al., *Synthesis of lead oxide nanoparticles by sonochemical method and its application as cathode and anode of lead-acid batteries.* Materials Chemistry and Physics, 2008. **108**(2-3): p. 337-344.

77. Karami, H. and M. Ghamooshi-Ramandi, *Synthesis of sub-micro and nanometer sized lead oxide by sol-gel pyrrolysis method and its application as cathode and anode of lead-acid batteries.* Int. J. Electrochem. Sci, 2013. **8**: p. 7553-7564.

78. Sammes, N. and Z. Cai, *Ionic conductivity of ceria/yttria stabilized zirconia electrolyte materials.* Solid State Ionics, 1997. **100**(1-2): p. 39-44.

79. Huang, W., P. Shuk, and M. Greenblatt, *Properties of sol-gel prepared Ce1− xSmxO2− x2 solid electrolytes.* Solid State Ionics, 1997. **100**(1-2): p. 23-27.

80. Yoshimura, M. and W. Suchanek, *In situ fabrication of morphology-controlled advanced ceramic materials by Soft Solution Processing.* Solid State Ionics, 1997. **98**(3-4): p. 197-208.

81. Chavan, S. and A. Tyagi, *Combustion synthesis of nanocrystalline yttria-doped ceria.* Journal of materials research, 2004. **19**(2): p. 474-480.

82. Chavan, S. and A. Tyagi, *Preparation and characterization of Sr 0.09 Ce 0.91 O 1.91, SrCeO 3, and Sr 2 CeO 4 by glycine–nitrate combustion: Crucial role of oxidant-to-fuel ratio.* Journal of materials research, 2004. **19**(11): p. 3181-3188.

83. Bedekar, V., S. Chavan, and A. Tyagi, *Highly sinter-active nanocrystalline RE 2 O 3 (RE= Gd, Eu, Dy) by a combustion process, and role of oxidant-to-fuel ratio in preparing their different crystallographic modifications.* Journal of materials research, 2007. **22**(3): p. 587-594.

84. Singh, G., et al., *Effect of oxidant-to-fuel ratios on phase formation of PLZT powder; prepared by gel-combustion.* Journal of Alloys and Compounds, 2011. **509**(10): p. 4127-4131.

85. Ravindranathan, P. and K. Patil, *A one-step process for the preparation ofγ-Fe 2 O 3.* Journal of materials science letters, 1986. **5**(2): p. 221-222.

86. Yang, Y.-J., et al., *Characteristics of lanthanum strontium chromite prepared by glycine nitrate process.* Solid State Ionics, 2000. **135**(1-4): p. 475-479.

87. Alqat, A., et al., *Synthesis of hexagonal YMnO3 from precursor obtained by the glycine–nitrate process.* Ceramics International, 2013. **39**(3): p. 3183-3188.

88. Mohseni, H., et al., *Magnetic and structural studies of the Mn-doped Mg–Zn ferrite nanoparticles synthesized by the glycine nitrate process.* Journal of Magnetism and Magnetic Materials, 2012. **324**(22): p. 3741-3747.

89. Chick, L.A., et al., *Glycine-nitrate combustion synthesis of oxide ceramic powders.* Materials Letters, 1990. **10**(1-2): p. 6-12.

90. Chen, X., et al., *Combustion synthesis of lead oxide nanopowders for the preparation of PMN–PT transparent ceramics.* Ceramics International, 2015. **41**(1): p. 755-760.

91. Shen, M., et al., *Raman spectroscopy study of ferroelectric modes in [001]-oriented 0.67 Pb (Mg 1/ 3 Nb 2/ 3) O 3–0.33 PbTiO 3 single crystals.* Applied Physics Letters, 2005. **86**(25): p. 252903.

92. Chen, Y.-H., K. Uchino, and D. Viehland, *Substituent Effects in 0.65 Pb (Mg1/3Nb2/3O30. 35PbTiO3 Piezoelectric Ceramics.* Journal of electroceramics, 2001. **6**(1): p. 13-19.

93. Lee, S.H., et al., *Hot isostatic pressing of transparent Nd: YAG ceramics.* Journal of the American Ceramic Society, 2009. **92**(7): p. 1456-1463.

94. Zhilun, G., et al., *Low-Temperature Sintering of Lead-Based Piezoelectric Ceramics.* Journal of the American Ceramic Society, 1989. **72**(3): p. 486-491.

95. Frueh, T., et al., *The Effects of Na2O and SiO2 on Liquid Phase Sintering of Bayer Al2O3.* Journal of the American Ceramic Society, 2016. **99**(7): p. 2267-2272.

96. Ji, W., et al., *Effect of La content on dielectric, ferroelectric and electro-optic properties of Pb (Mg 1/3 Nb 2/3) O 3–PbTiO 3 transparent ceramics.* Ceramics International, 2015. **41**(2): p. 1950-1956.

97. Zhao, K., et al., *Domain dynamics of La-doped PMN-PT transparent ceramics studied by piezoresponse force microscope.* Applied Surface Science, 2014. **293**: p. 366-370.

98. Ruan, W., et al., *Large Electro-Optic Effect in La-Doped 0.75 Pb (Mg1/3Nb2/3) O3–0.25 PbTiO3 Transparent Ceramic by Two-Stage Sintering.* Journal of the American Ceramic Society, 2010. **93**(8): p. 2128-2131.

99. Chen, X., et al., *Effects of dopants on the microstructure and phase-purity control in PMN-PT ceramics.* Ceramics International, 2018. **44**(15): p. 17909-17913.

100. Pilgrim, S.M., et al., *Electromechanical Properties of Some Pb (Mg1/3Nb2/3–PbTiO3–(Ba, Sr) TiO3 Ceramics: I.* Journal of the American Ceramic Society, 1992. **75**(7): p. 1964-1969.

101. Wallace, J.S., et al., *Grain growth and twin formation in 0.74 PMN· 0.26 PT.* Journal of the American Ceramic Society, 2002. **85**(6): p. 1581-1584.

102. Kong, L., et al., *Translucent PMN and PMN-PT ceramics from high-energy ball milling derived powders.* Materials research bulletin, 2002. **37**(1): p. 23-32.

103. Fang, Z.Z., *Sintering of advanced materials*. 2010: Elsevier.

104. Guo, Y., et al., *The phase transition sequence and the location of the morphotropic phase boundary region in (1− x)[Pb (Mg1/3 Nb2/3) O3]–xPbTiO3 single crystal.* Journal of Physics: Condensed Matter, 2003. **15**(2): p. L77.

105. King, H., et al. *X-ray Diffraction Study of PMN-PT Ceramics in the Region of the Relaxor Transition*. in *Proc. 2nd. Canada-Us CanSmart Workshop on Smart Materials and Structures*. 2002. Citeseer.

106. Roth, R.S., *Classification of perovskite and other ABO3-type compounds.* J. Res. Nat. Bur. Stand, 1957. **58**(2): p. 75-88.

107. Zhang, S.-T., et al., *Lead-free piezoceramics with giant strain in the system Bi 0.5 Na 0.5 Ti O 3–Ba Ti O 3–K 0.5 Na 0.5 Nb O 3. I. Structure and room temperature properties.* Journal of Applied Physics, 2008. **103**(3): p. 034108.

108. Jaffe, B., *Piezoelectric ceramics*. Vol. 3. 2012: Elsevier.

109. Sun, J., G. Rao, and J. Liang, *Crystal structure and electronic transport property of perovskite manganese oxides with a fixed tolerance factor.* Applied physics letters, 1997. **70**(14): p. 1900-1902.

110. Zhang, J., et al., *Effect of La-doping content on the dielectric and ferroelectric properties of 0.88 Pb (Mg 1/3 Nb 2/3) O 3–0.12 PbTiO 3 ceramics.* Journal of Materials Science: Materials in Electronics, 2014. **25**(2): p. 653-658.

111. Orihara, H. and Y. Ishibashi, *A phenomenological theory of nonlinear dielectric response.* Journal of the Physical Society of Japan, 1995. **64**(1): p. 99-105.

112. Osman, J., et al., *Nonlinear optic coefficients in the ferroelectric phase.* JOURNAL-KOREAN PHYSICAL SOCIETY, 1998. **32**: p. S446-S449.

113. Murgan, R., et al., *Calculation of nonlinear-susceptibility tensor components in ferroelectrics: cubic, tetragonal, and rhombohedral symmetries.* JOSA B, 2002. **19**(9): p. 2007-2021.

114. Varon, I., G. Porat, and A. Arie, *Controlling the disorder properties of quadratic nonlinear photonic crystals.* Optics letters, 2011. **36**(20): p. 3978-3980.

115. Vodopyanov, K., *Terahertz-wave generation with periodically inverted gallium arsenide.* Laser physics, 2009. **19**(2): p. 305-321.

116. Stutius, W., *Growth and doping of ZnSe and ZnSxSe1-x by organometallic chemical vapor deposition.* Journal of Crystal Growth, 1982. **59**(1-2): p. 1-9.

117. Kamata, A., H. Mitsuhashi, and H. Fujita, *Origin of the low doping efficiency of nitrogen acceptors in ZnSe grown by metalorganic chemical vapor deposition.* Applied physics letters, 1993. **63**(24): p. 3353-3354.

118. Zhang, X., et al., *Growth and luminescence of zinc-blende-structured ZnSe nanowires by metal-organic chemical vapor deposition.* Applied physics letters, 2003. **83**(26): p. 5533-5535.

119. Dibenedetto, B. and J. Pappis, *Chemical Vapor deposition of multispectral domes*. 1975, RAYTHEON CO WALTHAM MA RESEARCH DIV.

120. Myhajlenko, S., et al., *Luminescence studies of individual dislocations in II-VI (ZnSe) and III-V (InP) semiconductors.* Journal of Physics C: Solid State Physics, 1984. **17**(35): p. 6477.

121. Terashima, K., M. Kawachi, and M. Takena, *Growth of ZnSe crystals by nonstoichiometric annealing.* Journal of crystal growth, 1990. **102**(3): p. 387-392.

122. Terashima, K., M. Kawachi, and M. Takena, *Characteristics of ZnSe crystals annealed under host atom atmospheres.* Journal of crystal growth, 1990. **104**(2): p. 467-474.

123. Terashima, K., et al., *Study of point defects in bulk ZnSe grown by nonstoichiometric annealing.* Japanese journal of applied physics, 1993. **32**(2R): p. 736.

124. Triboulet, R., et al., *Solid state recrystallization of II-VI semiconductors: application to cadmium telluride, cadmium selenide and zinc selenide.* Le Journal de Physique IV, 1995. **5**(C3): p. C3-141-C3-149.

125. Triboulet, R., et al., *Growth by solid phase recrystallization and assessment of large ZnSe crystals of high purity and structural perfection.* Journal of crystal growth, 1996. **159**(1-4): p. 156-160.

126. Fusil, S., et al. *Grain growth of ZnSe recrystallized in the solid phase*. in *Solid State Phenomena*. 1998. Trans Tech Publ.

127. Rzepka, E., et al., *Optical transmission of ZnSe crystals grown by solid phase recrystallization.* Journal of crystal growth, 1999. **197**(3): p. 480-484.

128. Triboulet, R., *Solid state recrystallization: a promising technique for the growth of semiconductor materials.* Crystal Research and Technology, 2003. **38**(3-5): p. 215-224.

129. Holman, R.L., *Novel uses of gravimetry in the processing of crystalline ceramics*, in *Processing of Crystalline Ceramics*. 1978, Springer. p. 343-358.

130. Lemasson, P., et al., *New results and trends in the solid phase recrystallization of ZnSe.* Materials Letters, 1998. **36**(1): p. 162-166.

131. Moriya, K. and T. Ogawa, *Growth history of a synthetic quartz crystal.* Journal of Crystal Growth, 1982. **58**(1): p. 115-121.

132. Gall-Borrut, P., et al. *Observation of defect structure in ceramic oxides by laser scattering tomography*. in *Window and Dome Technologies and Materials II*. 1990. International Society for Optics and Photonics.

133. Donecker, J. and M. Naumann, *Laser scattering tomography for crystal characterization: Quantitative approaches.* Crystal Research and Technology: Journal of Experimental and Industrial Crystallography, 2002. **37**(2-3): p. 147-157.

134. Burke, J. and D. Turnbull, *Recrystallization and grain growth.* Progress in metal physics, 1952. **3**: p. 220-292.

135. Avetissov, I., et al., *Nonstoichiometry and luminescent properties of ZnSe crystals grown from melt and vapor.* Journal of Crystal Growth, 2014. **401**: p. 686-690.

136. Rahaman, M.N., *Ceramic processing and sintering*. 2003: CRC press.

137. Press, W.H., *Numerical recipes 3rd edition: The art of scientific computing*. 2007: Cambridge university press.

138. Hellwarth, R. and P. Christensen, *Nonlinear optical microscopic examination of structure in polycrystalline ZnSe.* Optics Communications, 1974. **12**(3): p. 318-322.

139. Fischer, R., et al., *Broadband femtosecond frequency doubling in random media.* Applied physics letters, 2006. **89**(19): p. 191105.